Reviews of Geophysics

REVIEW ARTICLE
10.1029/2019RG000679

The Physics of Sediment Transport Initiation, Cessation, and Entrainment Across Aeolian and Fluvial Environments

Thomas Pähtz[1,2], Abram H. Clark[3], Manousos Valyrakis[4], and Orencio Durán[5]

[1]Institute of Port, Coastal and Offshore Engineering, Ocean College, Zhejiang University, Hangzhou, China, [2]State Key Laboratory of Satellite Ocean Environment Dynamics, Second Institute of Oceanography, Hangzhou, China, [3]Department of Physics, Naval Postgraduate School, Monterey, CA, USA, [4]Infrastructure and Environment Research Division, School of Engineering, University of Glasgow, Glasgow, UK, [5]Department of Ocean Engineering, Texas A&M University, TX College Station, USA

Key Points:
- The physics of sediment transport initiation, cessation, and entrainment across aeolian and fluvial environments is reviewed
- The focus lies on the simplest physical systems: mildly sloped, nearly monodisperse sediment beds without complexities such as vegetation
- A large part of the review concerns consensus-changing developments in the field within the last two decades

Correspondence to:
T. Pähtz,
0012136@zju.edu.cn

Citation:
Pähtz, T., Clark, A. H., Valyrakis, M., & Durán, O. (2020). The physics of sediment transport initiation, cessation, and entrainment across aeolian and fluvial environments. *Reviews of Geophysics*, *58*, e2019RG000679. https://doi.org/10.1029/2019RG000679

Received 4 SEP 2019
Accepted 29 DEC 2019
Accepted article online 5 JAN 2020

Abstract Predicting the morphodynamics of sedimentary landscapes due to fluvial and aeolian flows requires answering the following questions: Is the flow strong enough to initiate sediment transport, is the flow strong enough to sustain sediment transport once initiated, and how much sediment is transported by the flow in the saturated state (i.e., what is the transport capacity)? In the geomorphological and related literature, the widespread consensus has been that the initiation, cessation, and capacity of fluvial transport, and the initiation of aeolian transport, are controlled by fluid entrainment of bed sediment caused by flow forces overcoming local resisting forces, whereas aeolian transport cessation and capacity are controlled by impact entrainment caused by the impacts of transported particles with the bed. Here the physics of sediment transport initiation, cessation, and capacity is reviewed with emphasis on recent consensus-challenging developments in sediment transport experiments, two-phase flow modeling, and the incorporation of granular physics' concepts. Highlighted are the similarities between dense granular flows and sediment transport, such as a superslow granular motion known as creeping (which occurs for arbitrarily weak driving flows) and system-spanning force networks that resist bed sediment entrainment; the roles of the magnitude and duration of turbulent fluctuation events in fluid entrainment; the traditionally overlooked role of particle-bed impacts in triggering entrainment events in fluvial transport; and the common physical underpinning of transport thresholds across aeolian and fluvial environments. This sheds a new light on the well-known Shields diagram, where measurements of fluid entrainment thresholds could actually correspond to entrainment-independent cessation thresholds.

Plain Language Summary Loose sediment grains can be transported by blowing wind (aeolian) or water flowing in a riverbed (fluvial). These processes are responsible for shaping much of the natural world, but they involve the combination of several very complex physical systems, like turbulent fluid flow near a rough boundary and the mechanical behavior of granular materials. Thus, there is no consensus about the minimum wind or water speeds required to initiate and sustain sediment transport. Additionally, wind and water-driven sediment transport are obviously similar, suggesting that it should be possible to capture both under one description. Recent advances in experiments and computer simulations have helped scientists to answer some key questions about why sediment transport is initiated and sustained. This article reviews many of these recent discoveries, focusing on three key topics: (1) the mechanical behavior of granular materials; (2) how turbulence in the fluid helps to move grains; and (3) the role of inertia of mobile grains. We show that a deeper understanding of these topics helps to resolve some major inconsistencies in our understanding of why sediment transport is initiated and sustained and may help to unify sediment transport by wind and water under a single theoretical description.

1. Introduction

When an erodible sediment bed is subjected to a shearing flow of a Newtonian fluid, such as air or water, bed particles may be *entrained* (i.e., set into motion) by the action of flow forces and then transported by the flow, initiating a process known as *sediment transport*. The critical conditions that are required for the initiation of sediment transport have been studied for more than two centuries (e.g., Brahms, 1757). Dating

back to the pioneering studies for water-driven transport by Shields (1936) and for wind-driven transport by Bagnold (1936, 1937, 1938) (summarized in his book (Bagnold, 1941)), the initiation of sediment transport in both cases has been commonly described by threshold values of the time-averaged shear stress τ that the flow applies onto the bed (see reviews by Durán et al., 2011; Dey & Ali, 2018, 2019; Kok et al., 2012; Merrison, 2012; Yang et al., 2019; and references therein). The idea of a threshold value of τ is natural, since a necessary condition for flow-driven entrainment (or *fluid entrainment*) is that flow forces and/or flow-induced torques acting on bed surface particles must overcome resisting forces and/or torques. Consistently, for wall-bounded flows (to which sediment transport belongs) at a given shear Reynolds number $Re_* \equiv u_* d/\nu_f$, the shear velocity $u_* \equiv \sqrt{\tau/\rho_f}$ controls the near-surface profile of the streamwise flow velocity when averaged over the entire spectrum of turbulent fluctuations (see review by Smits et al., 2011, and references therein), where ρ_f is the fluid density, ν_f the kinematic fluid viscosity, and d a particle diameter characteristic for bed particles. As forces resisting entrainment of a bed particle scale with the submerged gravity force ($\propto (\rho_s - \rho_f) g d^3$), where ρ_s is the particle density and g the gravity constant, it has been common among geomorphologists to nondimenionalize τ via $\Theta \equiv \tau/[(\rho_p - \rho_f) g d]$ (Shields, 1936), which is known as the *Shields number* or *Shields parameter*. In the aeolian research community, the *threshold parameter* $\sqrt{\Theta}$ (Bagnold, 1941, p. 86) is also often used. Shields (1936) and numerous researchers after him have measured transport thresholds for water-driven transport (see reviews by Miller et al., 1977; Buffington & Montgomery, 1997; Dey & Ali, 2019; Dey & Papanicolaou, 2008; Paphitis, 2001; Yang et al., 2019; and references therein). These measurements are usually summarized in a diagram showing the threshold Shields number Θ_t as a function of Re_* (the *Shields curve* $\Theta_t(Re_*)$), which is known as the *Shields diagram*.

However, the concept of a threshold shear stress for *incipient motion* (i.e., for the initiation of sediment transport by fluid entrainment) has had several consistency problems. First, for wind-driven transport, the most widely used incipient motion models (Iversen & White, 1982; Shao & Lu, 2000), when applied to Martian atmospheric conditions, predict threshold shear stresses for fine sand particles that are so large that transport should occur only during rare strong Mars storms (Sullivan & Kok, 2017). However, this prediction is contradicted by modern observations indicating widespread and persistent sediment activity (Bridges, Ayoub, et al., 2012; Bridges, Bourke, et al., 2012; Chojnacki et al., 2015; Silvestro et al., 2013), even of very coarse sand (Baker et al., 2018).

A second inconsistency, which has long been known, concerns water-driven sediment transport and is tacitly acknowledged whenever the concept of an incipient motion shear stress is applied: the sediment transport rate Q (i.e., the average particle momentum per unit bed area) seems to never truly vanish for nearly any $\Theta > 0$ in water flume experiments because of occasional strong turbulent fluctuation events causing entrainment by bursts of much-larger-than-average flow forces. That is why measurements of Θ_t have relied either on indirect extrapolation methods or on vague criteria defining the value of Q (or a proxy of Q) at which transport is critical (Buffington & Montgomery, 1997). Such criteria had been introduced even before Shields (Gilbert, 1914; Kramer, 1935). In particular, the experiments by Paintal (1971) suggest a power law relationship between Q, appropriately nondimensionalized, and Θ for weak flows over gravel beds: $Q_* \equiv Q/[\rho_p d\sqrt{(\rho_p/\rho_f - 1) g d}] \propto \Theta^{16}$ (it was necessary to measure Q over tens of hours for the weakest flows), which describes a dramatic but not infinitely rapid decrease of Q_* with decreasing Θ. Qualitatively similar observations were reported by Helland-Hansen et al. (1974). Largely because of Paintal's experiments, Lavelle and Mofjeld (1987) strongly argued in favor of stochastic sediment transport models that do not contain a threshold shear stress (e.g., Einstein, 1950) in a highly cited paper with the title, "Do Critical Stresses for Incipient Motion and Erosion Really Exist?" Despite the fact that many researchers have been well aware of this inconsistency, the concept of a threshold shear stress has remained alive and never been truly questioned by the majority of scientists working on water-driven sediment transport (Dey & Ali, 2018, 2019; Yang et al., 2019). There are two main reasons for the trust in this concept. First, above a value of Q_* that roughly coincides with typical criteria defining critical transport ($Q_* \approx 0.007$), the relationship between Q_* and Θ turns into a much milder power law (Paintal, 1971): $Q_* \propto \Theta^{2.5}$, suggesting a clear physical meaning of the threshold Shields number associated with this transition ($\Theta_t \approx 0.05$). Second, descriptions of water-driven sediment transport that are based on a threshold shear stress (i.e., expressions $Q_*(\Theta)$ with $Q_*(\Theta \leq \Theta_t) = 0$) have been quite successful in reproducing transport rate measurements for well-controlled conditions when using very similar values of Θ_t. For example, the scaling $Q_* \propto (\Theta - \Theta_t)^{3/2}$ by Meyer-Peter and Müller (1948) with $\Theta_t \approx 0.05$ is one of the most widely used expressions in hydraulic engineering

for gravel transport driven by water (Wong & Parker, 2006). However, if this value of Θ_t has a real physical meaning, what is it? Does it truly describe incipient motion, which has always been the predominant interpretation (see reviews by Miller et al., 1977; Buffington & Montgomery, 1997; Dey & Ali, 2018, 2019; Dey & Papanicolaou, 2008; Paphitis, 2001; Yang et al., 2019; and references therein), despite the fact that $Q_*(\Theta \leq \Theta_t) > 0$ (in Paintal's experiments, $Q_* > 0$ even for $\Theta \approx 0.007 \ll \Theta_t$)?

A third inconsistency in the concept of an incipient motion shear stress, which also concerns water-driven sediment transport, is also old but much less well known, perhaps because one of the key papers (Graf & Pazis, 1977) is published in French language. Graf's and Pazis's measurements show that increasing the shear stress on the bed due to the water flow from zero up to a certain value τ (a transport initiation protocol) results in smaller transport rates Q than decreasing the shear stress from a larger value down to τ (a transport cessation protocol). This clearly indicates an important role of particle inertia in sustaining water-driven sediment transport. Hence, any measurement of Θ_t is affected by particle inertia because, regardless of whether an initiation or cessation protocol is used, particles are already transported when Θ approaches Θ_t (see the second inconsistency discussed above). Hence, Θ_t is not, or at least not only, associated with fluid entrainment and thus incipient motion. The importance of particle inertia was proposed and indirectly shown even earlier, in a largely ignored study (only eight citations indexed by Web of Science today, half a century after publication) by Ward (1969). In this study, Ward (1969) measured smaller values of Θ_t for a larger particle-fluid-density ratio $s \equiv \rho_p/\rho_f$ (which is a measure for particle inertia) at the same shear Reynolds number Re_*. A slight downward trend of Θ_t with s even existed in the pioneering experiments by Shields (1936). Interestingly, a particle inertia effect in water-driven sediment transport has actually been studied. It is well known, although often not considered to be crucial in the context of transport thresholds, that the flow strength at which a transported particle can come to rest at the bed surface is weaker than the one at which it can reenter transport (e.g., Ancey et al., 2002; Drake et al., 1988; Francis, 1973; Reid et al., 1985). In contrast, another potentially important effect of particle inertia in water-driven sediment transport has not received the same attention: the interaction between particles that are already in transport and particles of the bed surface (e.g., particle-bed impacts) may support bed particle entrainment or even be predominantly responsible for it (*impact entrainment*).

Particle inertia and particularly impact entrainment have been widely recognized as crucial for sustaining wind-driven sediment transport since the pioneering studies by Bagnold (1941). Yet, in contrast to water-driven transport, there seems to be a clear-cut shear stress threshold when applying an initiation protocol in wind tunnel experiments (e.g., Bagnold, 1941). This rather curious difference between wind-driven and water-driven transport is usually not discussed in the context of incipient motion. Why is it necessary to define critical transport rates for measuring an incipient motion shear stress threshold in water-driven transport but not in wind-driven transport? A complete description of incipient motion should be generally applicable and not limited to a subset of possible sediment transport conditions, since there is no reason to believe that the physical mechanisms involved in the entrainment of a bed particle by a turbulent flow depend much on the nature of the flow. In fact, frameworks unifying sediment transport across driving fluids (not only in regard to transport thresholds) are scarce in general (e.g., apart from modern studies, only Bagnold (1956, 1973) seems to have attempted unifying water-driven and wind-driven transport conditions).

One of the most desired aspects of a general framework of sediment transport would be its ability to reliably predict the general dependency of Q_* on Θ and other dimensionless environmental parameters, such as the density ratio s. However, there is an obvious problem: since measured transport rates may depend on the experimental protocol for a given condition, as was the case in the experiments by Graf and Pazis (1977) (see third inconsistency), does the concept of a general relationship even make sense? The consensus is, yes, it does make sense when referring to transport *capacity* (also known as transport *saturation* in aeolian geomorphology), which loosely defines the maximal amount of sediment a given flow can carry without causing net sediment deposition at the bed. However, a precise definition of transport capacity is very tricky and controversial (see review by Wainwright et al., 2015, and references therein). For example, the fact that equilibrium transport rates may depend on the experimental protocol for a given condition implies that not every equilibrium transport condition is equivalent to transport capacity and that transport capacity is in some way linked to particle inertia. In fact, that the latter may be the case was recognized by Nino and Garcia (1998), who numerically modeled water-driven sediment transport as a continuous motion of particles hopping along a flat wall. In particular, these authors mentioned that the capacity relation obtained from their numerical simulations contains a threshold Shields number that may not be associated with fluid

entrainment, demonstrating the necessity for a good understanding of transport capacity and its relationship to particle inertia in the context of sediment transport thresholds.

While this introduction has focused on introducing issues in our understanding of fluid entrainment, shear stress thresholds, particle inertia, transport capacity, and their mutual relationships from a historical perspective, there have been major developments in these topics in the last two decades, largely because of the emergence of novel experimental designs and modeling techniques. The purpose of this review is to draw the attention of the involved research communities to these developments that, if put together, resolve the above issues and provide a largely improved conceptual understanding of sediment entrainment and transport thresholds.

A large portion of recent developments in the field can be attributed to numerical studies modeling the particle phase using the discrete element method (DEM). In comparison to other methods modeling the particle phase (e.g., continuum models), this method has the big advantage that it approximates the laws of physics at a very basic level, namely, at the level of intergrain contacts. In fact, the force laws commonly used to model intergrain contacts are known to produce system results that match experiments extremely well (e.g., Clark et al., 2016; Lätzel et al., 2003; Stewart et al., 2001). Additionally, granular continuum models are formulated using DEM simulations (da Cruz et al., 2005) but reproduce complex experiments on granular flows often very accurately (Jop et al., 2006). In the context of sediment transport, the main uncertainty of DEM-based models lies therefore in the modeling of the coupling between the particle phase and the Newtonian fluid driving transport. However, many of the simulations that are described in this review show that the results are often insensitive to the details of how this coupling is treated. The authors of this review thus argue that new physics uncovered by DEM-based numerical simulations are on a relatively solid footing.

To limit the scope of this review, it focuses on studies of *mildly sloped* beds of *relatively uniform* sediments unless mentioned otherwise. Also, because of the focus on physical processes involving the bed surface, this review largely concerns *nonsuspended* sediment transport (i.e., the fluid turbulence is unable to support the submerged particle weight), in which transported particles remain in regular contact with the bed surface (typical for particles of sand size and larger) and which is the relevant transport mode for the morphodynamics of planetary landscapes, riverscapes, and seascapes. In contrast, in suspended transport (typical for particles of silt or dust size and smaller), transported particles can remain out of contact with the bed surface for very long times (e.g., as atmospheric dust aerosols). In typical nonsuspended wind-driven (*aeolian*) sediment transport, many particles move in large ballistic hops and the transport layer thickness h is therefore much larger than the particle diameter d. In the aeolian geomorphology community, such hopping particles are said to move in *saltation* and explicitly distinguished from particles rolling and sliding along the surface. However, this terminology is not used in this review. Instead, the term *saltation transport* is used for general transport regimes with $h \gg d$, that is, it refers to all rather than a subset of transported particles. In typical nonsuspended liquid-driven transport (henceforth referred to as *fluvial* transport for simplicity although this mode is not limited to fluvial environments), h is of the order of d because the largest particle hops are small. Following the fluvial geomorphology community, transport regimes with $h \sim d$ are termed *bedload transport*.

This manuscript is organized into sections that focus on specific topics (sections 2–4) followed by a summary and outlook section (section 5) and a Notation section describing the definitions of technical terms and mathematical symbols. It is noted that readers may find it useful to read section 5 first in order to organize the contents of the manuscript, and then consult sections 2–4 for more detailed information on a particular topic. Section 2 reviews recent insights into the mechanics of beginning sediment motion and fluid entrainment gained from studying sediment transport as a dense granular flow phenomenon. For example, it has become increasingly clear that granular material can flow even when a macroscopic motion does not occur, such as for a collapsed pile of sand, because of a process known as *creeping*, which describes an irreversible superslow granular motion associated with sporadic microscopic rearrangements. That is, it is crucial to clearly define what kind of motion one refers to when introducing sediment transport thresholds. Likewise, forces resisting the entrainment of a bed particle do not only depend on the local arrangement of bed particles but also on granular interactions with regions within the bed that are far away from the entrainment location (i.e., sediment entrainment is a nonlocal phenomenon). This is because of collective granular structures that particles can form. Section 3 reviews insights gained from recent experimental and theoretical studies showing that the fluid shear stress applied onto the bed surface alone only poorly characterizes the critical

conditions required for fluid entrainment by turbulent flows. These studies have provided more suitable criteria for sediment entrainment that take into account turbulent fluctuation events and, in particular, their durations. However, section 3 also explains that a critical fluid shear stress for incipient motion does make sense when referring to the shear stress at which the fluid entrainment probability exceeds zero (which, for turbulent fluvial bedload transport, occurs much below the Shields curve (Paintal, 1971)). For example, in wind tunnel studies (but not necessarily in the field), aeolian saltation transport is initiated at about this threshold. Finally, section 4 reviews studies on the role of particle inertia in sediment transport, a topic that has very recently undergone a dramatic change. In fact, while it is well established that impact entrainment is crucial for aeolian saltation transport (see reviews by Durán et al., 2011; Kok et al., 2012; Valance et al., 2015; and references therein), very recent experimental and theoretical studies revealed that it is also crucial for sustaining fluvial bedload transport. Likewise, a very old argument by Bagnold (1941), which was forgotten or deemed unimportant, has recently been revived. Bagnold (1941) pointed out that, for aeolian saltation transport, a predominant role of impact entrainment requires that the flow is able to sustain the motion of transported particles. This is only possible if the energy loss of transported particles rebounding with the bed is compensated by their energy gain during their trajectories via fluid drag acceleration. Models that explicitly incorporate this requirement have been able to partially unify aeolian saltation and viscous and turbulent fluvial bedload transport. When combined, the insights from the studies reviewed in sections 2–4 provide a conceptual picture free of inconsistencies, which is described in section 5. For example, the shear stress threshold compiled in the Shields diagram seems to characterize the cessation of sediment bulk motion and an appropriately defined transport capacity rather than incipient motion. Section 5 also summarizes important open problems and provides a brief outlook into related problems that have not been discussed in this review, such as the effects of particle size heterogeneity on transport thresholds and bed sediment entrainment.

2. Yield and Flow of Dense Granular Media in the Context of Sediment Transport

In theoretical considerations of a problem as complex as the mechanics of beginning sediment motion, simplifying assumptions must be made. This often means that the granular phase is treated extremely coarsely, as a continuum with a Coulomb-like friction coefficient (Drucker & Prager, 1952; Terzaghi, 1951), or very finely, where the pocket geometry of individual grains sets the bed strength (Wiberg & Smith, 1987). However, recent advances in granular mechanics have shown that Coulomb-like behavior of granular materials is inherently *nonlocal*, so it must be treated on intermediate length scales. This is due to the fact that the *yielding* condition, defined as the minimum shear stress required to achieve permanent granular flow, is set by emergent, collective networks of grains. These networks can couple different sections of the material together over large distances. The purpose of this section is to provide an overview of recent work on yield and flow of dense granular materials in the context of sediment transport, with a particular focus on the nonlocal nature of granular yielding. To simplify the discussion, it is assumed throughout this section that the granular bed is subjected to a constant bed shear stress (like for laminar flows), in which case the existence of a fluid entrainment threshold associated with bed failure does make sense. However, this is no longer true for turbulent flows, as reviewed in section 3. For more information on dense granular flow, readers might consult recent reviews (Forterre & Pouliquen, 2008; Jop, 2015; Kamrin, 2018) devoted exclusively to the topic of dense granular flow. For the connection between granular flow and sediment transport, the perspective and review by Frey and Church (2009) and Frey and Church (2011), respectively, are also recommended.

2.1. Yielding of Granular Media

Surface grains sit in *pockets* on top of the bed, and the geometry of the pocket determines the entrainment conditions for that particular grain via its protrusion (i.e., the grain height above surrounding grains) and friction angle. When the downstream drag force from the fluid overcomes resistive forces from gravity and from contact forces with the pocket, the grain will begin to move. This conceptually simple scenario appears in many theoretical studies (e.g., Ali & Dey, 2016; Dey, 1999; Dey & Papanicolaou, 2008; Ling, 1995; Wiberg & Smith, 1987). However, this picture has several conceptual problems. For example, there are many different pocket geometries (Buffington et al., 1992; Kirchner et al., 1990) implying a distribution of entrainment thresholds. Kirchner et al. (1990) made a similar argument, advocating for a statistical treatment of pocket geometries, where only the grains with the smallest entrainment thresholds would be relevant. Additionally, when transport thresholds are discussed, one typically does not include transient behavior, after the

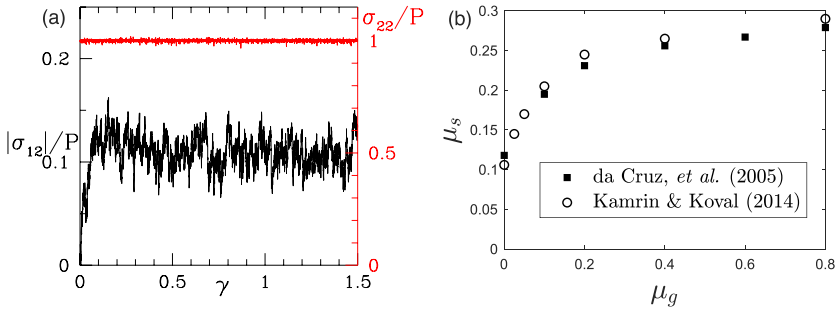

Figure 1. (a) From Peyneau and Roux (2008a), the normalized shear stress σ_{12}/P is plotted as a function of strain γ. The shear stress builds up from zero, reaching its maximum value at $\gamma \approx 0.1$. Copyright 2008 American Physical Society. (b) Data adapted from da Cruz et al. (2005) and Kamrin and Koval (2014) showing a measurement of the bulk static friction coefficient μ_s as a function of μ_g, which is the static friction coefficient between the surfaces of two grains (simulated as two-dimensional disks).

flow has pushed grains from less stable to more stable pockets. For example, an entrained grain that then restabilizes in a nearby pocket would not constitute sediment transport. After such a rearrangement, the resulting bed would have a different intergrain force and contact structure, which would be more suited to resisting the applied flow forces (Masteller & Finnegan, 2017). Thus, determining the fluid entrainment threshold amounts to determining the strongest bed that can be formed by the grains, subject to the flow forces and dynamics. This process necessarily involves transient behavior, as grains search for stable configurations, and spatial correlations, since information about each grain's movement is transmitted through the intergrain force network.

While this represents a very challenging problem, it is exactly the picture that has emerged in recent years regarding the physical origin of frictional behavior in noncohesive soils or sediments. The yield criterion of granular materials is defined by the maximum internal shear stress that a granular material can achieve, but grains must rearrange to find this maximum stress, sometimes for a long time (Clark et al., 2018; Srivastava et al., 2019). The yield criterion has the form of a friction coefficient, where flow occurs only when $\mu \equiv \tau_p/P > \mu_s$, where τ_p and P are the granular shear stress and pressure P, respectively, that arise from intergrain contacts, and μ_s is the static friction coefficient of the material. At first glance, this is not surprising, since the grains themselves have a surface friction coefficient μ_g. However, μ_s is only weakly dependent on μ_g (da Cruz et al., 2005), as shown in Figure 1.

Even *frictionless* spheres have $\mu_s \approx 0.1$ (Peyneau & Roux, 2008a, 2008b), which arises from a preferred orientation for intergrain contacts that aligns with the compressive direction of the applied shear deformation. This effect is independent of whether the grains interact via linear spring forces (Thompson & Clark, 2019) or more realistic Hertzian interactions (Peyneau & Roux, 2008a). Similar behavior is observed for grains with surface friction and irregular shape (Azéma & Radjaï, 2010 , 2014; Radjaï et al., 1998; Trulsson, 2018), but the maximum stress anisotropy is enhanced by these effects, since grain-grain contacts can have both normal and tangential components. This raises the yield stress slightly: frictional disks have $\mu_s \approx 0.2 - 0.3$ (da Cruz et al., 2005) and frictional spheres have $\mu_s \approx 0.3 - 0.4$ (Jop et al., 2006), with only a weak dependence on μ_g for $\mu_g > 0.1$. Additionally, μ_s is nearly independent of polydispersity (Voivret et al., 2009). This picture assumes grains are slowly moving with persistent intergrain contacts, but μ_s can be lowered significantly for more energetic kinds of driving, like vibration (Gaudel and De Richter, 2019) or in aeolian saltation transport (Pähtz, Durán, et al., 2019), probably because the tendency of the contact orientation to align with the compressive direction is somewhat suppressed (Pähtz, Dúran, et al., 2019). Thus, frictional behavior in granular media arises primarily from the anisotropic structure of force and contact networks, and grain-grain friction, shape, and polydispersity play secondary roles.

Here, μ is used to denote the local nondimensional shear stress in the granular material itself, while the Shields number Θ is the dimensionless shear stress applied to the granular bed surface, so the two quantities are not equivalent but are closely related. At the surface of the bed, $\mu \approx \Theta$ if lift forces are neglected. The existence of a maximum shear stress that can be supported by a granular material (which is independent of grain size) suggests that, for noncohesive sediments, there should be a theoretical upper limit to the

threshold Shields number Θ_t, $\Theta_t^{max} \approx \mu_s$. This implies that the Shields curve must plateau at low values of the shear Reynolds number Re_* for laminar flows. This fact has been a subject of debate for many years, with some authors (Buffington & Montgomery, 1997; Dey, 1999; Govers, 1987; Hong et al., 2015: Mantz, 1977; Miller et al., 1977; Shields, 1936; Yalin & Karahan, 1979) showing a trend where Θ_t continues to grow as Re_* gets smaller, while other studies (Paphitis, 2001; Pilotti & Menduni, 2001; Ouriemi et al., 2007; Wiberg & Smith, 1987) show a plateau at low Re_*. Recent work by the present authors (Clark, Shattuck, et al., 2015; Clark et al., 2017; Pähtz & Durán, 2018a) has investigated sediment transport thresholds over a wide range of Re_* and density ratio s using simulations based on the DEM to model noncohesive grains that are coupled to fluid-driven shear forces. These studies all suggest that Θ_t is a constant at low Re_* and s, corresponding to the strongest possible state of the bed. It is noted that cohesive effects become important for very small grains, which can cause Θ_t to continue to grow for smaller Re_*.

2.1.1. Open Problem: Value of Viscous Yield Stress Θ_t^{max}

Measured values of the viscous yield stress Θ_t^{max} vary substantially. For nearly monodisperse beds of spherical particles, most studies reported $\Theta_t^{max} \approx 0.12$ (Charru et al., 2004; Houssais et al., 2015; Loiseleux et al., 2005; Ouriemi et al., 2007; Seizilles et al., 2014), but larger values of up to about 0.37 have also been reported (Hong et al., 2015; Lobkovsky et al., 2008). Also, some measurements suggest that Θ_t^{max} depends on the median grain size (Hong et al., 2015), in contradiction to the grain size independence of μ_s, while other studies find no such dependence (Ouriemi et al., 2007). To the authors' knowledge, there is currently no convincing explanation for these contradicting observations. However, the scatter in the reported values for Θ_t^{max} (between 0.12 and 0.37) is within the range reported for the yield stress of granular materials, ranging from low-friction spheres to rougher, more frictional particles. Thus, the yield stress of the bulk granular material may at least play some role in setting the scatter in Θ_t^{max}. In this context, it is worth noting that, for the entrainment of particles resting on an idealized substrate by a laminar flow, threshold Shields numbers range from zero to very large values depending on the packing arrangement (Agudo et al., 2017; Deskos & Diplas, 2018; Shih & Diplas, 2019; Topic et al., 2019).

2.2. Rheological Descriptions

The existence of a yield stress is one piece of a rheological description, which is a constitutive law that mathematically connects the strain rate to the local stress at each point in a material. For granular materials, dissipation implies that more force is required for faster strain rates, so μ will increase with strain rate $\dot{\gamma}$. For the case of sediment transport, formulation of a constitutive law has obvious practical benefits, namely that it would allow an analytical prediction of transport rates Q at varying Shields number Θ for transport conditions dominated by granular interactions. However, note that a bulk constitutive law may not be able to capture certain cases, particularly very near to the onset or cessation of fluvial bedload or aeolian saltation transport, where the transport layer is dominated by the isolated motion of a single grain along the bed (which is the typical situation in gravel-bed rivers (Parker, 1978; Phillips and Jerolmack, 2016)). Despite the fact that the force and contact networks discussed above are spatially extended, some progress has been made by considering so-called *local rheologies*. Based on dimensional analysis, da Cruz et al. (2005) showed that μ for dry, uniform granular flows must depend on $\dot{\gamma}$ via a single dimensionless number, $I \equiv \dot{\gamma} d/\sqrt{P/\rho_p}$, where I is called the inertial number, similar to the Savage (Savage, 1984) or Coulomb (Ancey et al., 1999) numbers. A functional form for $\mu(I)$ can then be measured from experiments or DEM simulations (a crude approximation is given by $\mu = \mu_s + c_I I$, where c_I is a constant parameter). If one then assumes that a three-dimensional, tensorial generalization of this law is *locally* satisfied at each point in space in arbitrary geometries, then the equations of motion are closed and one can predict (at least numerically) flow in any arbitrary geometry where the forces and boundary conditions are known. Experimental measurements of rapid, dense flow in several geometries show good agreement with the local rheology (Jop et al., 2005, 2006; MiDi, 2004).

2.2.1. Open Problem: Rheology of Nonsuspended Sediment Transport

There are many physical mechanisms that are relevant to nonsuspended sediment transport that are not included in the inertial number description, but recent work has suggested that appropriate dimensional analysis can be used to find a general rheological description that is relevant in all contexts. For example, viscous effects from the fluid can be included (Amarsid et al., 2017; Boyer et al., 2011; Guazzelli & Pouliquen, 2018; Houssais & Jerolmack, 2017; Houssais et al., 2016; Ness & Sun, 2015, 2016; Trulsson et al., 2012) by replacing the inertial number I with the viscous number $J \equiv \rho_f \nu_f \dot{\gamma}/P$. This description is valid when the Stokes-like number I^2/J is small, and the standard $\mu(I)$ rheology again takes over for large I^2/J.

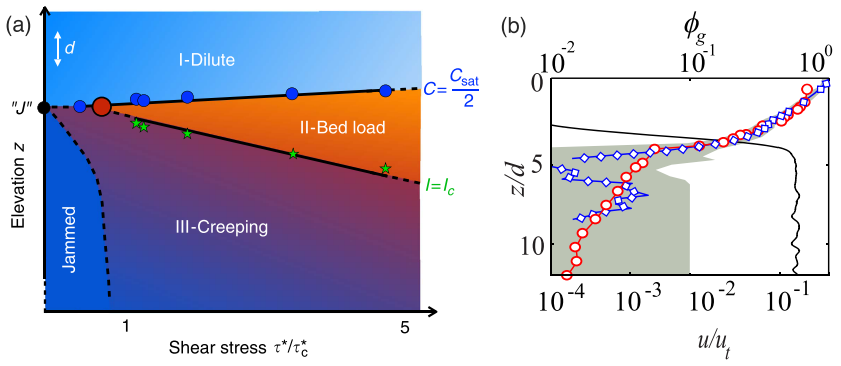

Figure 2. (a) From Houssais et al. (2015) (Creative Commons Attribution 4.0 International License), a proposed phase diagram for granular flow behavior as a function of elevation z in the bed (vertical axis) and applied shear stress $\tau^\star$ from the overlying fluid flow (horizontal axis). Bedload transport triggers slow creeping flow below it, consistent with nonlocal rheological models that have recently been formulated for dry granular media, as described in the text. (b) From Allen and Kudrolli (2017), normalized velocity profiles u/u_t for the fluid (blue squares) and grains (red circles) are plotted as a function of height z/d. Also plotted is the packing fraction of the grains ϕ_g as a function of height. The top of the bed corresponds to the drop in ϕ_g. Above the bed, grains move with the fluid. Below the bed, the grain velocity profile decays exponentially (a straight line on the semilogarithmic plot), which is a prediction of the nonlocal granular flow rheologies discussed in the text. Copyright 2017 American Physical Society.

This crossover can be heuristically written in terms of a viscoinertial number $K \equiv J + c_K I^2$, where c_K is an order-unity fit parameter (Trulsson et al., 2012; Ness & Sun, 2015, 2016; Amarsid et al., 2017), and the rheology takes the form $\mu(K)$.

The previous paragraph describes a unification of dry and wet, *viscous* granular flows, but some situations, like turbulent bedload or aeolian saltation transport, do not fit neatly into this description. Maurin et al. (2016) showed that, for intense turbulent bedload transport, the inertial number I (used for dry flows) collapses the data best, but with a different $\mu(I)$ relation compared to dry flows. Additionally, the presence of more severe velocity fluctuations and grain-grain collisions can weaken the material, giving a μ that is smaller than would be predicted by a $\mu(I)$ or $\mu(K)$ rheology at a given shear rate (Pähtz & Durán, 2018b). Another option is to build a rheological description that explicitly accounts for these fluctuations and collisions via the Péclet number $\mathrm{Pe} \equiv \dot{\gamma} d/\sqrt{T}$ (Pähtz, Durán, et al., 2019), where the granular temperature T equals the mean square of kinetic particle velocity fluctuations. The advantage of Pe is that it is applicable to a wide range of different granular flows (e.g., it unifies intense fluvial bedload and aeolian saltation transport), whereas K is limited to relatively homogeneous flows. The disadvantage is that Pe involves another granular property (T) that requires modeling.

2.3. Creep and Nonlocal Rheologies

As discussed in section 1, some water flume experiments suggest that fluvial bedload transport never truly ceases for nearly any $\Theta > 0$, which is usually attributed to turbulent fluctuations. However, as discussed in this section, the granular material itself may be partially responsible. In fact, it is well known that granular creep can be observed in a variety of observational geophysical contexts (Boulton & Hindmarsh, 1987; Ferdowsi et al., 2018; Pierson et al., 1987) as well as more idealized granular flows in a laboratory setting (Amon et al., 2013; Komatsu et al., 2001; Moosavi et al., 2013; Nichol et al., 2010; Roering et al., 2001), including sediment transport explicitly (Allen & Kudrolli, 2018; Houssais et al., 2015), as depicted in Figure 2. Generally, creeping refers to slow, typically intermittent flow (not limited to the bed surface) that occurs below a macroscopic yield criterion.

One class of creeping flow involves systems where regions with $\mu > \mu_s$ and $\mu < \mu_s$ exist nearby each other, which often occurs in systems with stress gradients (e.g., due to gravity or curvature). In this case, creeping flow is observed in regions with $\mu < \mu_s$ (Crassous et al., 2008; Fenistein & van Hecke, 2003; Koval et al., 2009; MiDi, 2004). This creeping flow is not steady or continuous, but occurs in a series of intermittent, avalanche-like slips, which are triggered by the nearby steadily flowing region with $\mu > \mu_s$. The time-averaged shear rate profiles decay quasi-exponentially with spatial distance to the steadily flowing region. Various nonlocal theories have been proposed (Baran et al., 2006; Pouliquen & Forterre, 2009) that include a spatial length scale ξ over which flow can be triggered in this way. The most successful theories

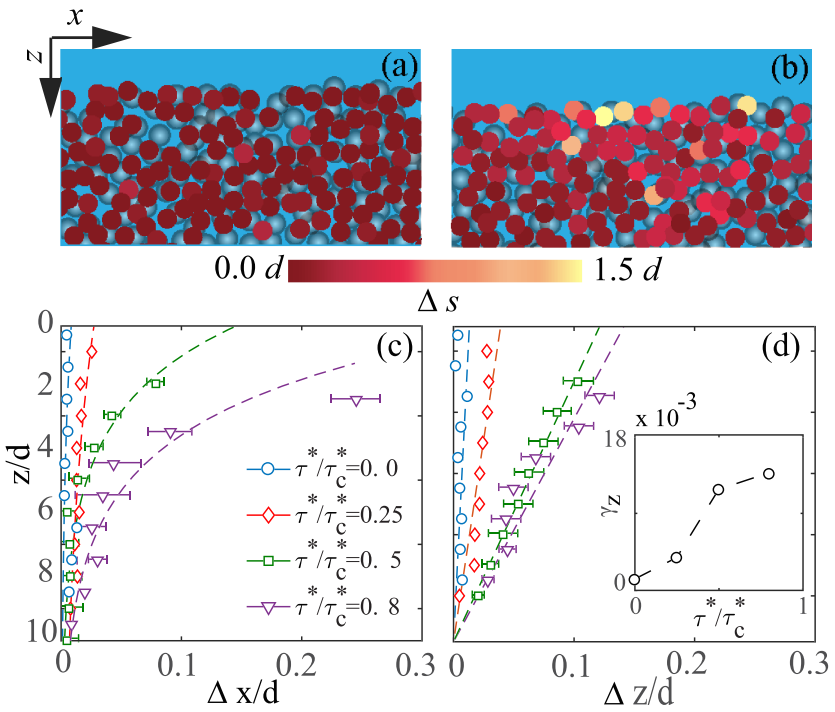

Figure 3. From Allen and Kudrolli (2018), particle movement during 90 min with (a) no fluid flow and (b) fluid flow at 80% of the critical flow rate (i.e., $\tau^*/\tau_c^* = 0.8$) to initiate particle transport (brighter colors indicate more particle movement). Movement is also plotted during times t = 30–90 s in the (c) flow (x) direction and (d) gravity (z) direction. There is exponential behavior in the x direction and a linear shift in the z direction. The strain γ_z is shown in the inset to (d), by fitting the slopes of the data in (d). Copyright 2018 American Physical Society.

(Bouzid et al., 2013, 2015 ; Henann & Kamrin, 2013; Kamrin & Henann, 2015; Kamrin & Koval, 2012) suggest that the cooperative length scale ξ *diverges at the yield stress* (i.e., $\xi \propto |\mu - \mu_s|^{-\nu}$, where $\nu \approx 0.5$). This means that, near the yield stress, flow events can be triggered over arbitrarily large distances; this point is revisited below. The grain-scale physical origin of the nonlocal models and associated spatial correlations (Zhang & Kamrin, 2017) as well as how exactly to best mathematically formulate a nonlocal rheology (Bouzid et al., 2017; Li & Henann, 2019) is still a subject of debate in the literature.

The creeping flow captured by these nonlocal models is also apparent in laboratory flumes used to model fluvial sediment transport. Houssais et al. (2015, 2016) showed that sediment transport involves the coexistence of three regimes: a dilute suspension above the bed surface, the bedload layer at the bed surface, and creeping behavior below the surface. These regions are depicted in Figure 2a. The shear rate profile in the creeping regime follows an exponential decay, which is consistent with the predictions of nonlocal models. Similar behavior was also observed by Allen and Kudrolli (2017), shown in Figure 2b, who also stressed that the apparent agreement with nonlocal models formulated for dry granular materials implies that the fluid stress is not playing a major role in the observed creeping behavior. In the creeping regime, $\mu < \mu_s$, but flow events are triggered via the bedload transport regime at the top of the bed via spatial correlations in the force network. These creeping events, although slow and intermittent, can lead to segregation effects over long times (~10–100 hr), where large particles are sorted to the top (Ferdowsi et al., 2017). Thus, creep and nonlocal rheology may play a crucial role in armoring of gravel-bedded rivers, as opposed to size sorting in the transported layer. Additionally, recent computational work (Pähtz & Durán, 2018b) has shown that sediment transport rheology is nonlocal even relatively far from the sediment transport threshold.

There is a second class of creeping flow, which is currently not explained by any rheological model. In the above discussion, creeping granular flow at $\mu < \mu_s$ was always induced by nearby regions with $\mu > \mu_s$. In some cases, creeping flow can be observed at $\mu < \mu_s$ without any apparent granular flow nearby at $\mu > \mu_s$ (Amon et al., 2013). This class of creep is often accompanied by compaction of the bed. Slow shear and compaction interact in a complex way that is not fully understood but can be crucial in regulating slow (e.g., millimeters to meters per day) geophysical flows (Moore & Iverson, 2002). Similar behavior was also

observed in laboratory sediment transport experiments by Houssais et al. (2015) and further studied by Allen and Kudrolli (2018), as shown in Figure 3.

The latter authors observed a granular bed with an overlying laminar shear flow and showed that slow (less than 0.1 grain diameters in 90 min) creeping flow persisted even for $\Theta \ll \Theta_t$ (meaning that $\mu < \mu_s$ everywhere in the granular bed). The grain motion in the direction of fluid flow followed an exponential decay with depth, similar to the creep described by nonlocal models. However, it was not induced by granular flow but somehow by the laminar fluid flow. Streamwise creep was also accompanied by compaction of the bed, which can strengthen the material and thus reduce creep. This second class of creep is therefore similar to compaction (Knight et al., 1995; Ribière et al., 2005) and creep (Candelier & Dauchot, 2009; Divoux et al., 2008) that is induced by tapping or vibrations, despite the fact that no explicit vibrations were applied. The existence of this class of creep implies that sediment is likely *always* transported (albeit slowly) for arbitrarily small values of Θ, even in the absence of turbulence. Another recent experimental flume study (Masteller & Finnegan, 2017) showed a similar result, where conditioning a bed by applying weak fluid flow led to zero net transport but a smoother bed profile with fewer protruding grains. Then, when the fluid flow rate was increased to a value associated with significant transport for a conditioned bed, sediment transport rates were smaller when compared with an unconditioned bed.

2.3.1. Open Problem: Physical Origin of Creeping Below Macroscopic Yield

The physical mechanisms that lead to the second class of creep, where $\mu < \mu_s$ everywhere in the system, are not known. One possible mechanism is contact aging (Jia et al., 2011), where the microscopic contact structure between two solid objects (i.e., grains) can evolve and weaken with time for reasons that are not fully understood (Liu & Szlufarska, 2012). Additionally, Pons et al. (2016) showed that this second class of creep could be induced in dry granular flow by applying small pressure fluctuations to the interstitial air, with resulting shear rates of the order of 10^{-7}. Similar fluctuations likely always exist in natural systems. These two hypotheses are supported by the fact that, to the authors' knowledge, this class of creep does not occur in DEM simulations, which use a Cundall-Strack model (Cundall & Strack, 1979) or similar Coulomb-like yield criterion for the frictional forces between grains, and fluctuating forces or slow variations in grain-grain friction are not included. Some DEM studies have observed creeping below a macroscopic yield criterion like the angle of response (Ferdowsi et al., 2018), but the results from these studies seem to always include some region of $\mu > \mu_s$.

2.4. Critical Behavior and Weak Links

Many experimental and computational studies (Carneiro et al., 2011; Heyman et al., 2013; Houssais et al., 2015) have observed that, near sediment transport thresholds (including the impact entrainment threshold, reviewed in section 4.1.3), the time t_{conv} required for some system measurement (e.g., the sediment transport rate Q) to converge to its steady state value appears to grow very large. A common form (Clark, Shattuck, et al., 2015) to capture these long time scales is $t_{\text{conv}} \propto |\Theta - \Theta_t|^{-\beta}$, where β is some positive exponent. A diverging time scale can arise in many ways, but one possibility is a *critical phase transition*. The study of phase transitions, where a material abruptly changes as a control parameter is smoothly varied, originated in thermal physics (e.g., liquid-gas or ferromagnetic transition), but it has also been successful in describing many other kinds of systems where thermal physics is not applicable. The key feature of a *critical* phase transition is a diverging correlation length, such that small changes near the critical point can have system-spanning effects that last for arbitrarily long times. The system is thus said to be *scale-free* at the critical point, since there is no largest length or time scale that is affected by a perturbation.

2.4.1. Open Question: Is Flow-Induced Bed Failure a Critical Phenomenon?

Bed failure at the yield stress describes by definition a phase transition, but whether this transition is critical and how it arises from grain-grain and grain-fluid interactions remain open questions. However, there is a growing body of work (Clark et al., 2018; Srivastava et al., 2019; Thompson & Clark, 2019) suggesting that the yielding transition for granular media is a critical transition. This is also suggested by the diverging correlation length $\xi \propto |\mu - \mu_s|^{-\nu}$ that is present in the nonlocal models discussed above (Kamrin & Koval, 2012; Bouzid et al., 2013). In addition to describing creeping flow for $\mu < \mu_s$, nonlocal theories are also able to correctly predict other size-dependent effects, like strengthening of thin layers (MiDi, 2004; Kamrin & Henann, 2015). The idea that yielding of granular media is a critical transition helps to explain certain experimentally observed behaviors in laboratory and computational models of sediment transport. For example, using a laboratory flume near the viscous limit, Houssais et al. (2015, 2016) found a diverging time scale near the critical Shields number that is "associated with the slowing down, and increasing variability, of the particle

dynamics; it is unrelated to hydrodynamics." Evidence of scale-free channeling patterns (Aussillous et al., 2016) was also observed during erosion of granular beds, which was attributed to the fact that the onset of erosion was behaving like a critical phase transition.

When the physics controlling the onset of grain motion is no longer just the yield strength of the granular material itself, then the picture changes somewhat. For example, once particle inertia becomes important in sustaining nonsuspended sediment transport (see section 4), the granular phase may not have a frictional state μ that is close to μ_s, and thus it may be far from the critical point. For viscous bedload transport (small Re_*), when particle inertia is not important, computational studies typically show that t_{conv} obeys system size dependence that is consistent with a critical phase transition (Clark et al., 2018; Yan et al., 2016). However, under steady driving conditions, when grain inertia starts to play a role (e.g., for larger Re_*), then t_{conv} still diverges, $t_{\mathrm{conv}} \propto |\Theta - \Theta_t|^{-\beta}$, but systems of different sizes will have the same t_{conv} (Clark, Shattuck, et al., 2015; Clark et al., 2017). Thus, Θ_t for inertial particles appears to be more similar to a dynamical instability rather than a true critical point.

However, nonlocal effects still likely play a role in the initiation of permanent bed failure. For example, if particle inertia plays a crucial role in sustaining sediment transport, as argued below in section 4, then a bed could be above the threshold needed to sustain motion but not have any way to get started. Returning to the argument from Kirchner et al. (1990) discussed above, if only the grains with the lowest entrainment thresholds are susceptible to being moved by the fluid, then these grains might be thought of as *weak links* in the bed. Motion that is initiated by these weak links could trigger flow elsewhere in the system, via the redistribution of forces or by collision. Clark, Shattuck, et al. (2015) and Clark et al. (2017) showed that the initiation of motion did indeed obey statistics consistent with a Weibullian weakest link scenario.

2.5. Summary

This section has described recent advances in the physics of sheared granular flows, with a focus on application to sediment transport. The main ideas are as follows. First, the yield condition for granular materials (e.g., a sediment bed) has the form of a static friction coefficient μ_s, but it is not set directly by grain-grain friction. Instead, μ_s is an emergent property that arises from the maximum structural anisotropy that the grain-grain contact network can support. Friction plays a minor role in determining this maximum anisotropy, and grain shape and polydispersity also play minor roles. Second, although these contact networks are extended in space (and thus inherently nonlocal), local rheological descriptions (i.e., constitutive laws) can be very successful in many contexts. Recent advances suggest that a unified, local rheological description might be within reach. This rule could be used to model any context of wet or dry granular flow with appropriate boundary conditions. Such a description could be used to predict sediment transport rates and thresholds if the grain properties (i.e., size distribution, friction coefficient, grain shape, etc.) were known, even approximately. Third, the inherently nonlocal nature of yielding is dominant when the material is near its yield condition. This causes creeping behavior in regions where a local rheology would predict no flow, which complicates the search for a unified rheological description. However, the results described in Figures 2 and 3 showed that creeping is similar in wet and dry flows, since it very slow and thus dominated by grain rearrangements (not fluid). This suggests that the nonlocal descriptions for wet and dry flows might also be unified in a relatively simple way. The underlying physics behind this nonlocal behavior is not fully understood, but there is mounting evidence that yielding of granular materials represents a kind of critical transition, where different parts of the system can be correlated over arbitrary distances. Remarkably, for sediment transport, creep seems to occur even much below the yield transition, that is, for seemingly arbitrarily small Shields numbers Θ.

This section has considered only sediment beds sheared by nonfluctuating flows and usually neglected the effects of particle inertia in sustaining sediment transport. That is, except for the occurrence of creep, many of the results of this section do not apply to turbulent flows nor flows with significant particle inertia effects that are near the threshold for grain motion (occurring for sufficiently large Re_* and/or s, see section 4). In particular, the average fluid shear stress at which turbulent flows are able to entrain bed particles is usually much below the yield stress of the granular phase. Nonetheless, both creep and the viscous yields stress $\Theta_t^{\max}$ will play crucial roles in the new conceptual picture of sediment transport thresholds and sediment entrainment that is presented in section 5.

3. Fluid Entrainment by Turbulent Flows

This section reviews the state of the art on the entrainment of bed particles by a turbulent flow of Newtonian fluid. This process is not equivalent to the initiation of overall sediment motion, which occurs even in the absence of bed sediment entrainment because of creeping (see section 2.3). It is also not equivalent to the comparably simple physics of fluid entrainment by a nonfluctuating flow. For example, when a laminar flow of a Newtonian fluid shears a target particle resting on the sediment bed, there are critical values of the fluid shear stress τ, which depend on the local bed arrangement, above which this particle begins to roll and slide, respectively (Agudo et al., 2017; Deskos & Diplas, 2018). Once motion begins, resisting forces weaken and, since the flow does not fluctuate, the particle will inevitably leave its bed pocket (i.e., become entrained). The entrained particle will travel along the bed until it comes to rest in another pocket in which it can resist the flow, provided such a pocket exists and is accessible (when the sediment bed has yielded, particles can no longer find stable resting place, see section 2.1). In contrast, in turbulent flows, even though resisting forces weaken when a bed particle becomes mobilized, such a mobilized particle may not find its way out of its initial bed pocket (i.e., incomplete entrainment). The prototype for this situation is a turbulent fluctuation of the flow that exerts a large force on the particle, but the fluctuation is too short-lived for it to become entrained. Hence, there are two important ingredients that need to be considered to accurately describe sediment entrainment by turbulent flows for a given pocket geometry: the magnitude and duration of turbulent fluctuations (evidence for this statement is briefly reviewed in section 3.1). Only entrainment criteria that account for both aspects are able to accurately describe fluid entrainment experiments (section 3.2). Shear stress-based criteria, in general, do not belong to this category. Yet one can still define the critical shear stress τ_t^{In} above which the probability of fluid entrainment exceeds zero. This and related thresholds have received a lot of attention in studies on aeolian and planetary transport (section 3.3).

3.1. The Role of Turbulent Fluctuations in Fluid Entrainment

Turbulent fluctuations have been known to play a crucial role in fluid entrainment for a long time. For example, Einstein and El-Samni (1949), and later Mollinger and Nieuwstadt (1996), measured large fluctuating lift forces on a fixed rough surface induced by pressure gradient fluctuations of the order of the mean pressure gradient. These authors concluded that such pressure gradient fluctuations must be important also for the mobilization of bed sediment. In fact, numerous laboratory, field, and theoretical studies have advocated the viewpoint that the magnitude of peaks of the instantaneous flow force acting on a bed particle, consisting of both lift and drag forces, is a key aspect of fluid entrainment (e.g., Apperley & Raudkivi, 1989; Cameron et al., 2019, 2020; Dwivedi et al., 2010a, 2010b; Giménez-Curto & Corniero, 2009; Heathershaw & Thorne, 1985; Hofland et al., 2005; Kalinske, 1947, 1967; Kirchner et al., 1990; Nelson et al., 1995; Paintal, 1971; Papanicolaou et al., 2001; Schmeeckle et al., 2007; Sumer et al., 2003; Vollmer & Kleinhans, 2007; Zanke, 2003). However, while such force peaks explain certain observations, such as the episodic character of very weak turbulent bedload transport (Helland-Hansen et al., 1974; Hofland, 2005; Paintal, 1971) or the strong increase of weak turbulent bedload transport in the presence of vegetation (Yang & Nepf, 2018, 2019; Yager & Schmeeckle, 2013), they do not explain all observations. In fact, experiments in which a target particle was placed on an idealized rough substrate and exposed to an electrodynamic force revealed that very high force pulses do not lead to entrainment if their duration is too short (Diplas et al., 2008). Likewise, moderate force pulses that only barely exceed resisting forces lead to entrainment if their duration is sufficiently long. That the duration of force peaks is as important as their magnitude has also been experimentally confirmed both for particles resting on idealized, fixed beds (Celik et al., 2010, 2013, 2014; Diplas et al., 2008; Valyrakis, 2013; Valyrakis et al., 2010, 2011, 2013) and natural erodible sediment beds (Salim et al., 2017, 2018). However, note that, for sediment transport along erodible beds (with the exception of viscous bedload transport), the vast majority of entrainment events are triggered by particle-bed impacts, except for very weak transport conditions (see sections 4.1.2 and 4.1.3). In the following, criteria are reviewed that account for both the magnitude and duration of turbulent fluctuation events.

3.2. Entrainment Criteria That Account for the Magnitude and Duration of Turbulent Fluctuation Events

3.2.1. Impulse Criterion

The initiation of movement of a target particle resting in a pocket of the bed surface necessarily requires that the instantaneous flow forces (or torques) $F(t_0)$ acting on it at the instant t_0 of initial motion overcome

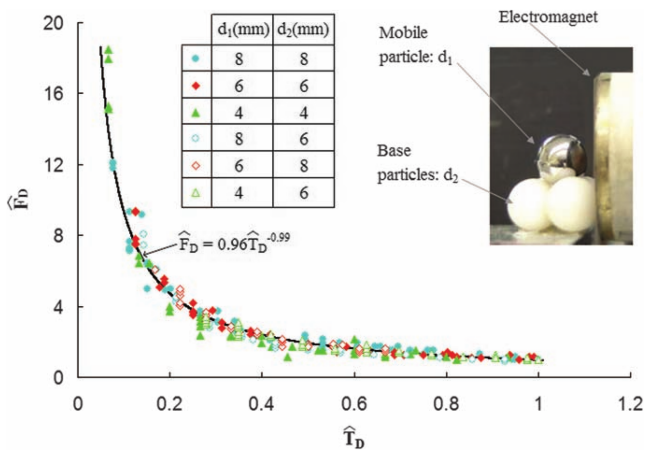

Figure 4. From Diplas et al. (2008) (M.V. is copyright holder), normalized magnitude $\hat{F}_D$ of the electrodynamic force pulse that is required for entrainment versus normalized duration $\hat{T}_D$ of the force pulse. Data correspond to the entrainment experiments that were carried out for various particle arrangements and varying sizes of the target (d_1) and base particles (d_2). The line corresponds to the prediction $\hat{F}_D = \hat{T}_D^{-1}$ associated with a constant impulse threshold.

resisting forces (or torques) F_c:

$$F(t_0) \geq F_c, \tag{1}$$

However, this criterion is not sufficient for entrainment to occur as the target particle may merely move back to its initial resting place if $F(t)$ becomes subcritical for times t too soon after t_o so that its gained kinetic energy is insufficient to overcome the potential barrier of its bed pocket. For this reason, Diplas et al. (2008) proposed that the fluid impulse I_f associated with larger-than-critical flow forces must exceed a critical value:

$$I_f \equiv \int_{t_0}^{t_0+T} F(t)\mathrm{d}t \geq I_{fc} \quad \text{with} \quad F(t) \geq F_c \quad \text{for} \quad t \in (t_0, t_0+T), \tag{2}$$

where T is the duration of the impulse event (i.e., the duration of the particle acceleration phase of a turbulent fluctuation event). Note that T can be much smaller than the time needed to leave the bed pocket as the latter also includes the particle deceleration phase. Diplas et al. (2008) confirmed their hypothesis with idealized experiments in which they subjected an isolated target particle with a constant electrodynamic, horizontal force F_D for a given time T_D, for which $I_f = F_D T_D$. In fact, their measured data of the force that is required for entrainment roughly obey the relation $\hat{F}_D \equiv F_D/F_D^{\min} = T_D^{\max}/T_D \equiv \hat{T}_D^{-1}$, where $F_D^{\min}$ is the minimal force required for measurable particle motion (but not necessarily entrainment) and $T_D^{\max}$ the associated time that is needed for $F_D^{\min}$ to cause entrainment (Figure 4).

In order to use equation (2) for predicting particle entrainment, one needs to know the impulse threshold I_{fc}. For entrainment into a rolling motion, Valyrakis et al. (2010) derived an expression for the critical impulse $I_{fc} = F_t T_t$ (F_t is defined below) assuming a constant pulse of a hydrodynamic force, separated into a horizontal drag and vertical lift component ($\mathbf{F} = (F_D, F_L)$), of short duration T_t (so that the angular displacement $\Delta\psi$ of the particle remains small for $t \in (t_0, t_0 + T_t)$):

$$I_{fc} = \frac{F_t}{g}\sqrt{2f(\psi,\alpha,s)L_{\mathrm{arm}}g\left(\frac{7}{5}+\frac{C_m}{s}\right)}\sqrt{\frac{-m_p g}{2\rho_\psi(F_n - F_{nc})}}\,\mathrm{arsinh}\left[\frac{\sqrt{-2\rho_\psi(F_n-F_{nc})(m_p g)}}{(F_t - F_{tc})}\right], \tag{3}$$

where $F_t = F_D\sin\psi + F_L\cos\psi$ and $F_n = -F_D\cos\psi + F_L\sin\psi$ are the tangential and normal components, respectively, of the driving flow force at the rest position, $m_p = \frac{1}{6}\rho_p\pi d^3$ is the particle mass, $F_{tc} = m_p g\cos(\psi+\alpha)/\sin\psi - (m_p g/s)\cot\psi$ the resisting force, L_{arm} the lever arm length, $C_m = 1/2$ the added mass coefficient, and $f(\psi,\alpha,s) = \cos(\psi+\alpha)\sin\alpha + [1-\sin(\psi+\alpha)](\cos\alpha - 1/s)$, with α the bed slope angle and ψ the pivoting angle (Figure 5). For many conditions, this expression can be well approximated by (Valyrakis et al., 2010)

$$I_{fc} \approx m_p\left(\frac{F_t}{F_t - F_{tc}}\right)\sqrt{2f(\psi,\alpha,s)L_{\mathrm{arm}}g\left(\frac{7}{5}+\frac{C_m}{s}\right)}. \tag{4}$$

Lee et al. (2012) derived an alternate expression for short turbulent fluctuation events. Instead of a pure rolling motion, they considered entrainment into a combined rolling and sliding motion (however, note that rolling is usually the preferred mode of entrainment) without bed slope ($\alpha = 0$), assuming that the associated tangential motion is described by a Coulomb friction law with friction coefficient μ_C. Furthermore, instead of the pivoting angle, they described the pocket geometry by the horizontal (ΔX) and vertical (ΔZ) particle displacement (in units of d) that is needed for the particle to escape (equivalent to $\psi + \alpha = \pi/2$ in Figure 5). The expression by Lee et al. (2012) reads

$$I_{fc} \equiv (F_e T_e)_c = (\Delta Z + \mu_C \Delta X)m_p\sqrt{\frac{F_e}{F_e - F_{ec}}}\sqrt{2gd\left(1+\frac{C_m}{s}\right)\left(1+\frac{1}{s}\right)}, \tag{5}$$

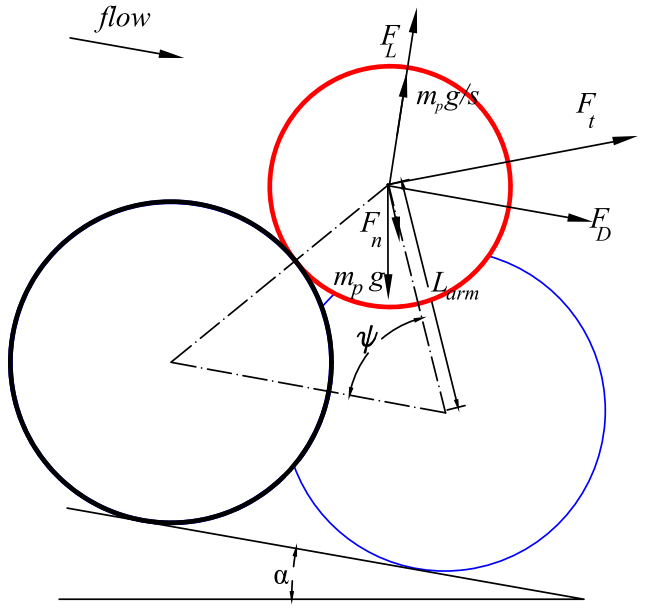

Figure 5. Sketch of pocket geometry.

where $F_e = F_D(\sin\psi - \mu\cos\psi) + F_L(\cos\psi + \mu_C \sin\psi)$ is an effective hydrodynamic force and $F_{ec} = m_p g(1 - 1/s)(\sin\psi + \mu_C \cos\psi)$ its critical value. For entrainment into a hopping motion, defined as a lift force-induced particle uplift by a vertical distance $\geq 1d$, Valyrakis et al. (2010) derived

$$I_{fc} \equiv (F_L T_L)_c = m_p \sqrt{\frac{F_L}{F_L - F_{Lc}}} \sqrt{2gd\cos\alpha \left(1 + \frac{C_m}{s}\right)\left(1 + \frac{1}{s}\right)}, \quad (6)$$

where the resistance force is given by $F_{Lc} = m_p g(1 - 1/s)\cos\alpha$. Note that equation (6) with $\alpha = 0$ is equivalent to equation (5) if the critical dimensionless displacement $\Delta Z + \mu_C \Delta X = 1$ and $F_{L(c)}$ replaced by $F_{e(c)}$.

Equations (3)–(6) reveal that the impulse threshold I_{fc} is constant only if the driving flow force is very strong ($F(t) \gg F_c$). However, for near-critical fluctuation events ($F(t) \to F_c$), I_{fc} diverges. This motivates the introduction of an energy-based entrainment criterion.

3.2.2. Energy Criterion

The impulse criterion (equation (2)) accounts for the available momentum of the turbulent fluctuation event in comparison to the momentum required for entrainment. However, close observation of near-bed turbulence reveals that fluctuation events are scarcely ever square pulses or even single-peaked (Valyrakis, 2013). Instead, turbulent flows in nature exhibit a wide range of flow patterns and structures, some of which may be more efficient for particle entrainment than others. For example, the transfer of energy from flow to particles in turbulent fluctuation events with large driving flow forces ($F(t) \gg F_c$) is expected to be much more efficient than in fluctuation events with near-critical flow forces ($F(t) \sim F_c$, see section 3.2.1). This motivates the characterization of entrainment using the energy of the fluctuation event that is effectively transferred to the particle (Valyrakis et al., 2013):

$$C_{\text{eff}} E_f = C_{\text{eff}} \int_{t_0}^{t_0+T} P_f(t)\mathrm{d}t \geq W_c, \quad (7)$$

where W_c is the minimal amount of work required for complete particle entrainment and $P_f(t) = f[u(t)^3]$ the instantaneous flow power, parameterized by the cube of the local flow velocity, and C_{eff} is the coefficient of energy transfer efficiency of the turbulent fluctuation event. The energy transfer coefficient C_{eff} is expected to increase with $\langle F\rangle/F_c$ (see section 3.2.1), where $\langle\cdot\rangle$ denotes the time average over the event. Water flume experiments on the entrainment of a particle resting on an idealized substrate have confirmed that C_{eff} tends to increase with $\langle F\rangle/F_c$ (Figure 6). However, one has to keep in mind that C_{eff} incorporates also other effects such as grain orientation and shape.

In order to use equation (7) for predicting particle entrainment, one needs to know the energy threshold W_c. Valyrakis et al. (2013) derived

$$Rolling: W_c = m_p \cos\alpha[1 - \sin(\psi + \alpha)](1 - 1/s)gL_{\text{arm}}, \quad (8)$$

$$Hopping: W_c = m_p \cos\alpha(1 - 1/s)gd. \quad (9)$$

For typical sediment beds, the ratio between both energy thresholds ($[1 - \sin(\psi + \alpha)]L_{\text{arm}}/d$) is of the order of 0.1, demonstrating that a rolling motion is much more easily initiated upon entrainment than a hopping motion. Note that, in contrast to the expressions for the critical impulse for rolling (equations (3) and (4)), equation (8) does neither require the assumption of a small angular particle displacement $\Delta\psi$ during the acceleration phase of a turbulent fluctuation event nor the assumption of a short duration of this phase.

3.3. Shear Stress Threshold of Incipient Motion and Initiation of Aeolian Saltation Transport

The entrainment criteria reviewed in section 3.2 are able to predict whether a certain turbulent fluctuation event is capable of entraining a target particle, whereas a criterion based on a critical shear stress would not

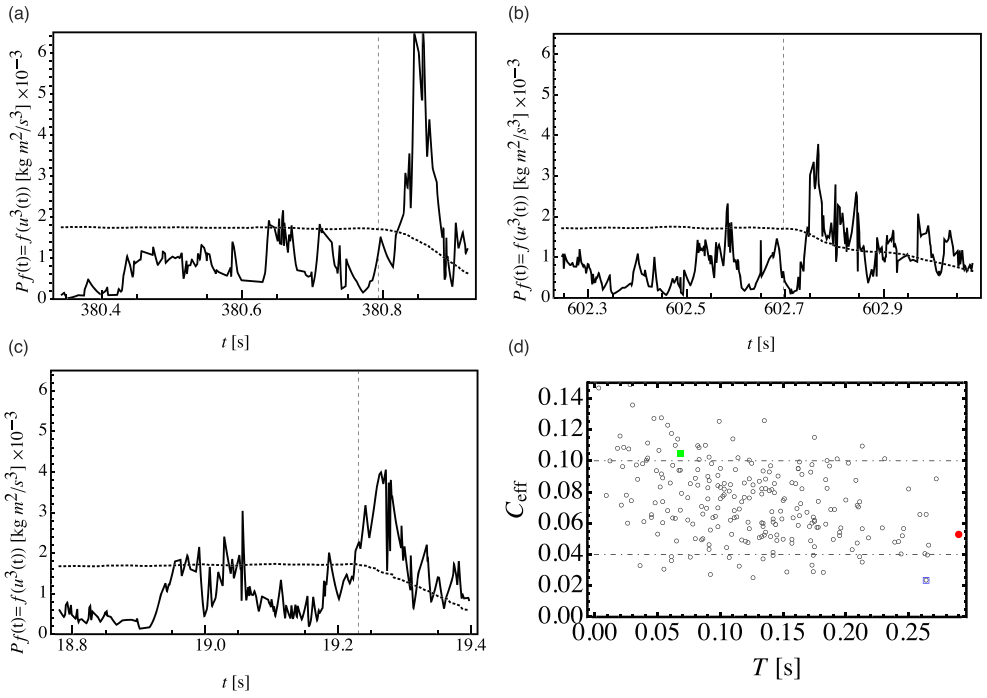

Figure 6. (a–c) Flow power $P_f(t)$ versus time t for three different turbulent fluctuation events that lead to entrainment of a target particle resting on a prearranged substrate. The solid lines correspond to experimental data (Valyrakis et al., 2013). The dashed lines indicate the start of the respective fluctuation event. The dotted lines indicate the critical flow power that must be exceeded in order to overcome the resisting forces (i.e., $u > u_c(t)$), which depend on time because resisting forces weaken once the target particle starts to move. (d) Coefficient of energy transfer C_{eff} versus duration of turbulent fluctuation event (T) for various recorded entrainment events (symbols). The green closed square corresponds to the event shown in (a), the blue open square to the event shown in (b), and the red closed circle to the event shown in (c).

suffice for this purpose. However, one can still define a shear stress threshold τ_t^{In} (the *initiation threshold*) at which the fluid entrainment probability exceeds zero (i.e., below which entrainment never occurs). Such a threshold must exist because the size of turbulent flow eddies is limited by the system dimensions, such as the boundary layer thickness δ. In fact, a limited size of turbulent flow eddies implies that also the magnitude of peaks of the flow force is limited. That is, one can always find a nonzero shear stress below which even the largest fluctuation peaks do not exceed the resisting forces acting on bed particles (however, note that the existence of sufficiently large flow force peaks does not guarantee a nonzero entrainment probability because their durations may always be too short). Like for $\Theta_t^{\max}$, transient behavior associated with the flow temporarily pushing particles from less stable to more stable pockets is excluded in the definition of τ_t^{In}, which implies $\Theta_t^{\text{In}} \simeq \Theta_t^{\max}$ for laminar flows at sufficiently low shear Reynolds number Re_*. Furthermore, surface inhomogeneities that can generate a lot of turbulence, such as vegetation (Yang & Nepf, 2018, 2019; Yager & Schmeeckle, 2013), are also not considered in the definition of τ_t^{In}. While τ_t^{In} is usually not measured for turbulent fluvial bedload transport (it is much below the Shields curve (Paintal, 1971)), it has often been measured in wind tunnel experiments (briefly reviewed in section 3.3.1), including those that sought to determine the initiation threshold of aeolian saltation transport. The reason is that, as soon as the first particles of the initially quiescent bed surface are entrained (i.e., begin to roll as rolling requires the smallest flow forces), the flow is usually nearly sufficient to net accelerate them during their downstream motion, resulting in larger and larger particle hops (i.e., the initiation threshold of aeolian saltation transport is only slightly larger than τ_t^{In}) (Bagnold, 1941; Burr et al., 2015; Iversen et al., 1987). This occurs because, for typical wind tunnels, τ_t^{In} is significantly above the cessation threshold of saltation transport (see section 4.3). However, it will become clear that this statement may not apply to aeolian field conditions. Section 3.3.2 briefly reviews models of τ_t^{In} derived from wind tunnel experiments, while section 3.3.3 reviews recent evidence that indicates that such models, in general, are unreliable, particularly when applied to field conditions.

3.3.1. Wind Tunnel Experiments of the Initiation of Aeolian Rolling and Saltation Transport

Two distinct experimental setups have been used to measure τ_t^{In}. In the first setup, small isolated patches of particles are placed at the bottom of a wind tunnel and then the fluid shear stress τ is increased until particles in such patches start to roll or detach (de Vet et al., 2014; Merrison et al., 2007; Williams et al., 1994). In the second setup, a complete bed of particles is prepared at the tunnel bottom and then the fluid shear stress τ is increased until saltation transport begins (e.g., Bagnold, 1937; Burr et al., 2015; Carneiro et al., 2015; Chepil, 1945; Cornelis & Gabriels, 2004; Dong et al., 2003; Greeley et al., 1976, 1980, 1984; Greeley & Marshall, 1985; Gillette et al., 1980; Iversen et al., 1976; Iversen and Rasmussen, 1994; Lyles and Krauss, 1971; Nickling, 1988; Swann et al., 2020) (see also Raffaele et al., 2016, and references therein). It is worth noting that, according to the definition of τ_t^{In}, beginning saltation transport refers to the mere occurrence of saltation transport, even if very sporadic, which is also the definition used by Bagnold (1937). However, many experimental studies defined beginning saltation transport through a critical loosely defined saltation transport activity (similar to the definition of the fluvial transport thresholds compiled in the Shields diagram), which yields slightly larger threshold values (Nickling, 1988).

3.3.1.1. Open Problem: Qualitative Discrepancy Between Threshold Measurements

For cohesionless particles ($d \gtrsim 100\mu$m), existing threshold measurements based on the second setup show that τ_t^{In} increases relatively strongly with the particle diameter d (Raffaele et al., 2016). In contrast, for the first setup, measurements indicate that τ_t^{In} remains constant with d for $d \gtrsim 100\mu$m (Merrison et al., 2007; de Vet et al., 2014). The reason for this qualitative inconsistency is not understood. Merrison et al. (2007) suggested that the initiation of rolling (measured in their experiments) may be different to that of saltation transport. However, this suggestion is inconsistent with the observation that saltation transport in wind tunnels is preceded by rolling further upwind (Bagnold, 1941; Burr et al., 2015; Iversen et al., 1987). Furthermore, in contrast to standard wind tunnel experiments, for experiments in pressurized wind tunnels with Venusian air pressure, both an equilibrium rolling (lower initiation threshold) and an equilibrium saltation transport regime (higher initiation threshold) exist, and both initiation thresholds strongly increase with d (Greeley & Marshall, 1985).

3.3.2. Models of the Initiation of Aeolian Rolling and Saltation Transport

Nearly all existing models of the initiation of aeolian rolling and saltation transport (including sand transport (Bagnold, 1941; Burr et al., 2015; Claudin & Andreotti, 2006; Cornelis & Gabriels, 2004; de Vet et al., 2014; Durán et al., 2011; Duan, Cheng, & Xie, 2013; Edwards & Namikas, 2015; Iversen et al., 1976, 1987; Iversen & White, 1982; Kok & Renno, 2006; Lu et al., 2005; Merrison et al., 2007; Shao & Lu, 2000), drifting snow (He & Ohara, 2017; Lehning et al., 2000; Schmidt, 1980), and the transport of regolith dust by outgassed ice on the comet 67P/Churyumov-Gerasimenko (Jia et al., 2017)) predict τ_t^{In} from the balance between aerodynamic forces and/or torques and resisting forces and/or torques acting on a bed particle. Even though many of these models do not consider peaks of the aerodynamic force, and some of them do not treat τ_t^{In} as what it is (i.e., the threshold at which the fluid entrainment probability exceeds zero, see above), they are conceptually very similar and mainly differ in the empirical equations that they use for the aerodynamic and cohesive interparticle forces. For this reason, only one of the most popular and simple models, the model by Shao and Lu (2000), is discussed here. It reads

$$\Theta_t^{\mathrm{In}} = A_N \left(1 + \frac{\gamma_C}{\rho_p g d^2}\right), \tag{10}$$

where $A_N = 0.0123$ is an empirical scaling factor and $\gamma_C = 3 \times 10^{-4}$ kg/s^2 an empirical constant that accounts for cohesive interparticle forces. More complex models (e.g., Claudin & Andreotti, 2006; Durán et al., 2011; Iversen & White, 1982) involve additional dependencies of Θ_t^{In} on the shear Reynolds number Re_* or, equivalently, on the *Galileo number* $Ga \equiv \sqrt{(s-1)gd^3}/\nu_f \equiv Re_*/\sqrt{\Theta}$ (also called *Yalin parameter* (Yalin, 1977)).

3.3.3. Effects of the Boundary Layer Thickness on the Initiation of Aeolian Rolling and Saltation Transport

The size of turbulent flow eddies, and thus the duration of turbulent fluctuation events, is limited by the system dimensions, more specifically, the boundary layer thickness δ (see review by Smits et al., 2011, and references therein). However, in most wind tunnel experiments and the field, the produced turbulent boundary layer should be so thick that any turbulent fluctuation has a nonzero probability to last sufficiently long for entrainment to occur (Pähtz et al., 2018). That is, the mere existence of aerodynamic force peaks that exceed resisting forces is sufficient for τ_t^{In} to be exceeded. However, this is no longer true when δ becomes

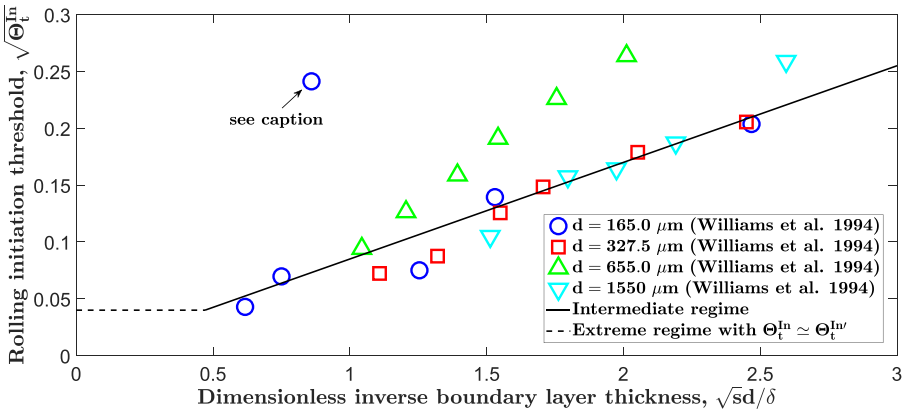

Figure 7. From Pähtz et al. (2018) (Creative Commons Attribution 4.0 International License), threshold parameter $\sqrt{\Theta_t^{In}}$ versus dimensionless inverse boundary layer thickness $\sqrt{s}d/\delta$. Symbols correspond to the measurements of incipient rolling by Williams et al. (1994), who set up their wind tunnel in a manner that produces a developing turbulent boundary layer, for four different sediments consisting of nearly uniform, cohesionless particles. The solid line corresponds to equation (11) for the intermediate regime using $\sqrt{\Theta_t^{In'}} \simeq$ const (neglecting the weak logarithmic dependency of $\sqrt{\Theta_t^{In'}}$ on δ/d). This regime turns into the extreme regime in which $\sqrt{\Theta_t^{In}} \simeq \sqrt{\Theta_t^{In'}}$. This transition is shown by the dashed line assuming $\sqrt{\Theta_t^{In'}} = 0.04$ (only for illustration purposes as the actual values of $\sqrt{\Theta_t^{In'}}$ in the experiments by Williams et al. (1994) are unknown). It is suspected that the one extreme outlier for $d = 165\mu$m may either have been a faulty measurement or be associated with the observation that the boundary layer for this particular sand sample was not always fully turbulent (Williams et al., 1994).

too small, at which point turbulent fluctuation events may cause particles to rock (i.e., vibrate or wobble or oscillate) within their bed pockets but no fluctuation lasts long enough for the particles to completely leave them. Pähtz et al. (2018) physically modeled such situations and derived an expression for the ratio between τ_t^{In} and the shear stress threshold $\tau_t^{In'}$ of incipient rocking (equivalent to the Shields number ratio $\Theta_t^{In}/\Theta_t^{In'}$). These authors' derivation uses the impulse criterion of section 3.2.1 (even though Pähtz et al. (2018) start with the energy criterion, their analysis is effectively equivalent to assuming a constant impulse threshold) and the fact that the maximal duration T_{max} of turbulent fluctuation events is controlled by δ and the local mean flow velocity $\overline{u}$ via $T_{max} \propto \delta/\overline{u}$ (Alhamdi & Bailey, 2017). The derived expression reads

$$\sqrt{\frac{\Theta_t^{In}}{\Theta_t^{In'}}} \simeq \begin{cases} 1 & \text{if} \quad C < 1 \\ C & \text{if} \quad 1 \leq C \leq \alpha_f \\ \alpha_f & \text{if} \quad C > \alpha_f \end{cases} \tag{11}$$

$$C \equiv \alpha_f^{-1} f(G) \frac{\sqrt{s}d}{\delta}.$$

where $\alpha_f \equiv u_m/\overline{u} \geq 1$ is the ratio between the characteristic flow velocity u_m associated with the largest positive fluctuations and $\overline{u}$, and $f(G)$ is a factor that encodes information about particle shape, orientation, and the pocket geometry. Equation (11) encompasses three different regimes. In one extreme, if there is a nonzero probability that turbulent fluctuation events associated with the largest positive fluctuations last sufficiently long for particle entrainment, then there will be a nonzero probability that incipient rocking evolves into incipient rolling (i.e., $\Theta_t^{In}/\Theta_t^{In'} \simeq 1$). In the other extreme, if all positive fluctuation events always last too short, the mean flow must exceed the torque balance for entrainment to occur (i.e., $\Theta_t^{In}/\Theta_t^{In'} \simeq \alpha_f^2$). In the intermediate regime between these two extremes, $\Theta_t^{In}/\Theta_t^{In'}$ is proportional to the square of the inverse dimensionless boundary layer thickness $(d/\delta)^2$. Although weak logarithmic dependencies on δ/d are also incorporated in α_f and $\Theta_t^{In'}$ (Lu et al., 2005), they are dominated by this proportionality. In fact, Figure 7 shows that the prediction for the intermediate regime is roughly consistent with the experimental data by Williams et al. (1994) if one uses that the Shields number for incipient rocking ($\Theta_t^{In'}$) is approximately constant, neglecting the logarithmic dependency of $\Theta_t^{In'}$ on δ (and further minor dependencies on Ga). Williams et al. (1994) set up their wind tunnel in a manner that produces a relatively thin developing turbulent boundary layer (i.e., δ increases with downstream distance). However, once the intermediate regime is exceeded (i.e., $\Theta_t^{In} \simeq \Theta_t^{In'}$) because δ becomes too large, as for most wind tunnel experiments with fully developed

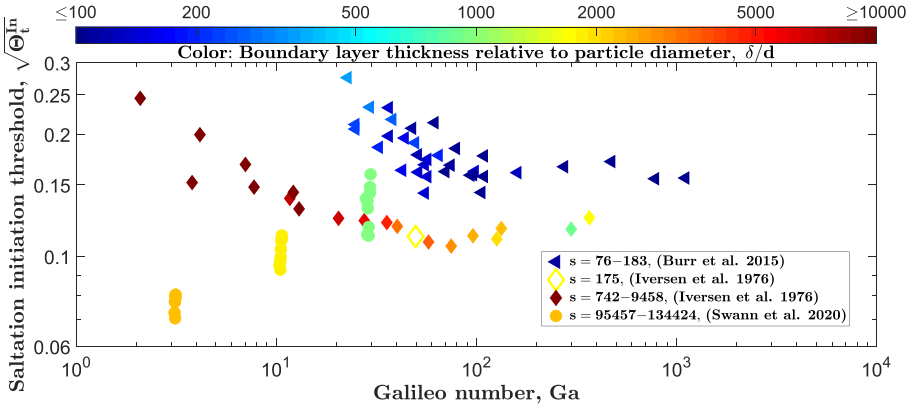

Figure 8. Modified from Pähtz et al. (2018) (Creative Commons Attribution 4.0 International License), compilation of measurements in wind tunnels with fully developed boundary layer of the initiation threshold parameter of saltation transport ($\approx \sqrt{\Theta_t^{In}}$) (Burr et al., 2015; Iversen et al., 1976; Swann et al., 2020) versus the Galileo number Ga. The color indicates the thickness of the boundary layer δ relative to the particle diameter d, which controls the relative amplitude of turbulent fluid velocity fluctuations for a constant Ga. Circles correspond to threshold values obtained from the raw data by Swann et al. (2020). The threshold values for the experiments by Iversen et al. (1976) are found in Iversen and White (1982).

boundary layers, the logarithmic dependency of Θ_t^{In} on δ/d via $\Theta_t^{In\prime}$ may become significant (Figure 8). For example, for the same Galileo number Ga, the threshold values measured by Burr et al. (2015) in Figure 8, which were carried out in a pressurized wind tunnel with $\delta \approx 1.9$ cm, are significantly larger than those measured by Iversen et al. (1976), which were carried out in a wind tunnel with $\delta \approx 1.2$ m.

3.3.3.1. Open Problem: Unexpected Behavior of Saltation Transport Initiation Threshold for Large Density Ratio

The very recent measurements by Swann et al. (2020), who used a very- low pressure wind tunnel and three different beds of cohesionless particles ($d = [310, 730, 1310]$ μm) to mimic Martian conditions, indicate that $\sqrt{\Theta_t^{In}}$ unexpectedly increases substantially with Ga and thus d (Figure 8). A possible explanation could be that, because of the very large density ratio s, some of the experimental conditions may have been in the intermediate regime (i.e., $1 \leq C \leq \alpha_f$ in equation (11)), in which $\sqrt{\Theta_t^{In}}$ scales with d (Figure 7). In fact, $1/C \propto \delta/(\sqrt{s}d) \simeq [3.1, 4.9, 12.4]$ for the three conditions, where only the largest value (corresponding to $d = 310$μm) is larger than the critical value $\delta/(\sqrt{s}d) \approx 6.6$ that Pähtz et al. (2018) associated with the end of the intermediate regime. In other words, the measurements for $d = 730$μm and $d = 1310$μm may both have been in the intermediate regime, in which $\sqrt{\Theta_t^{In}}$ roughly scales with d (cf. Figure 7).

3.3.3.2. Controversy: Dependency of Saltation Transport Initiation Threshold on Density Ratio

Based on comparisons between experiments in pressurized wind tunnels with comparably very thin boundary layers but larger-than-normal air density (Burr et al., 2015; Greeley et al., 1984) and nonpressurized wind tunnels with comparably very large boundary layers (Iversen et al., 1976) (and normal air density), Iversen et al. (1987) and Burr et al. (2015) argued that there is an underlying decrease of the saltation transport initiation threshold (which is slightly larger than Θ_t^{In} for aeolian transport in typical wind tunnels, see above) with the density ratio s for a constant shear Reynolds number Re_* (equivalent to a constant Ga). However, this dependency on s may be an artifact of huge differences in the dimensionless boundary layer thickness δ/d (Pähtz et al., 2018). In fact, even though the dependency of Θ_t^{In} on δ/d is logarithmic once the intermediate regime is exceeded (like for the measurements in question), such weak dependencies can still have significant effects once differences in δ/d become very large. This point of view is supported by Figure 8, in which δ/d is color coded. It can be seen that the yellow, open diamond (a measurement from a nonpressurized wind tunnel) exhibits a similar value of s as the blue symbols (measurements from a pressurized wind tunnels), which was achieved by using a very light particle material ($\rho_p = 210$ kg/m^3). Nonetheless, the threshold $\sqrt{\Theta_t^{In}}$ of the former is significantly smaller than those of the latter. Also, the former measurement relatively smoothly connects to the other measurements carried out in the same nonpressurized wind tunnel, which exhibit much larger values of s. On the other hand, the measurements by Swann et al. (2020), for which s is comparably very large and δ/d of a similar size as for the measurements by Iversen et al.

(1976), support the density ratio hypothesis because of comparably small values of $\sqrt{\Theta_t^{\mathrm{In}}}$. Note that, for the discussion of threshold values, one has to keep in mind that threshold measurements are highly prone to measurement errors of various sources (Raffaele et al., 2016). Such errors are likely much larger than often reported because measurements of $\sqrt{\Theta_t^{\mathrm{In}}}$ can vary by more than a factor of 2 for a given condition, even for cohesionless particles (Raffaele et al., 2016).

3.3.3.3. Open Problem: Aeolian Bedload Transport in the Field

In wind tunnel experiments, rolling is being initiated at threshold values that are significantly above the cessation threshold of saltation transport (see section 4.3). This is why rolling seems to always evolve into saltation transport (i.e., equilibrium rolling and thus aeolian bedload transport does not seem to exist) (Bagnold, 1941; Burr et al., 2015; Iversen et al., 1987). However, atmospheric boundary layers are several orders of magnitude thicker than those of wind tunnels (Kok et al., 2012; Lebonnois et al., 2018; Lorenz et al., 2010; Petrosyan et al., 2011) and may therefore exhibit a significantly smaller rolling threshold. In contrast, the cessation threshold of saltation transport is predominantly a property of the mean turbulent flow (see section 4.3) and therefore rather insensitive to the boundary layer thickness δ. Hence, for atmospheric boundary layers, it is possible that equilibrium rolling transport exists. Note that equilibrium rolling transport has been observed in pressurized wind tunnels with Venusian air pressure for a narrow range of Shields numbers Θ (e.g., Greeley & Marshall, 1985).

3.3.3.4. Open Problem: Reliable Models of the Initiation Threshold of Planetary Saltation Transport

The most widely used models for the initiation of aeolian saltation transport (see section 3.3.2), which have been adjusted to wind tunnel measurements, do not take into account the dependency of the relative magnitude of turbulent fluctuations on the dimensionless boundary layer thickness δ/d. This may be the reason why these models, when applied to Martian atmospheric conditions, predict threshold shear stresses for fine sand particles that are so large that transport should occur only during rare strong Mars storms (Sullivan & Kok, 2017), in contradiction to modern observations indicating widespread and persistent sediment activity (Bridges, Ayoub, et al., 2012; Bridges, Bourke, et al., 2012; Chojnacki et al., 2015; Silvestro et al., 2013), even of very coarse sand (Baker et al., 2018). For example, for the Martian conditions reported by Baker et al. (2018) ($\rho_p = 2{,}900\ \mathrm{kg/m^3}$, $\rho_f = 0.02\ \mathrm{kg/m^3}$, $g = 3.71\ \mathrm{m/s^2}$, $d = 1.5\ \mathrm{mm}$), equation (10) predicts for the threshold shear velocity: $u_{*t}^{\mathrm{In}} \equiv \sqrt{\Theta_t^{\mathrm{In}}(\rho_p/\rho_f - 1)gd} \simeq 3.7\ \mathrm{m/s}$, which corresponds to winds that are more than twice as fast as the strongest Mars storms. Note that Lu et al. (2005) proposed a model for the initiation of rolling that includes the effect of δ/d. The authors of this review therefore recommend to use the model by Lu et al. (2005) in combination with models of the cessation threshold of saltation transport (see section 4.3) for the estimation of the occurrence of saltation transport in real atmospheric boundary layers. However, it remains to be demonstrated that this approach yields reliable predictions. In fact, in the field, atmospheric instability, topography gradients, and surface inhomogeneities, such as obstacles and vegetation, can dramatically enhance local turbulence and thus fluid entrainment. Likewise, sublimation of subsurface ice in cold environments (the so-called *solid-state greenhouse effect* Kaufmann et al., 2006) can generate airborne particles of carbon dioxide, methane, and nitrogen ice (Hansen et al., 1990; Jia et al., 2017; Telfer et al., 2018; Thomas et al., 2015). Given that even a few entrained particle can result in fully developed saltation transport provided that the fetch is sufficiently long (Sullivan & Kok, 2017), it may well be that saltation transport in the field can almost always be initiated close to the cessation threshold (Pähtz et al., 2018; Sullivan & Kok, 2017; Telfer et al., 2018). Evidence for this hypothesis is seen on Pluto, where aeolian dunes and wind streaks have been observed even though saltation transport initiation had been thought to be virtually impossible because of Pluto's very thin atmosphere (pressure $P = 1\ \mathrm{Pa}$) and relatively weak 10 m winds ($u_{10\mathrm{m}}^{\max} \approx 10\ \mathrm{m/s}$) (Telfer et al., 2018).

3.3.3.5. Open Problem: Lack of Direct Aeolian Sediment Transport Initiation Measurements in the Field

The overarching problem associated with the rather poor current knowledge of aeolian sediment transport initiation in the field (see open problems above) is that, to the authors' knowledge, there are no *direct* field measurements of the transport initiation threshold Θ_t^{In}. In fact, existing field experiments have focused on detecting aeolian saltation transport (Barchyn & Hugenholtz, 2011, and references therein) rather than on

how the fluid entrainment of individual bed particles, which usually starts out as a rolling motion, leads to saltation transport. Hence, we currently do neither know the wind speeds that are required in the field to initiate rolling transport of individual bed particles nor whether such rolling transport, like in wind tunnels, always evolves into saltation transport (see open problems above). What adds to the problem is that existing field studies either obtain saltation transport threshold estimates using methods that do not seek to distinguish saltation transport initiation and cessation (Barchyn & Hugenholtz, 2011, and references therein) or assume that Θ_t^{In} coincides with the continuous saltation transport threshold (Martin & Kok, 2018) (which is a controversial assumption, see section 4.1.3.3).

4. The Role of Particle Inertia in Nonsuspended Sediment Transport

As discussed in section 1, old experimental studies (e.g., Graf & Pazis, 1977; Ward, 1969) strongly indicated that the fluvial transport threshold measurements that are compiled in the Shields diagram are to a nonnegligible degree affected by particle inertia. As the Shields diagram shows a rough data collapse of the threshold Shields number Θ_t as a function of the shear Reynolds number Re_*, this raises the question of whether Re_* is in some way associated with particle inertia. Indeed, while Re_* has usually been interpreted as the ratio between the particle size and the size of the viscous sublayer of the turbulent boundary layer, Clark et al. (2017) showed that it can also be interpreted as a number that compares the viscous damping time scale to the ballistic time scale between bed collisions. Importantly, these authors showed that the shape of the Shields curve can be partly explained by the fact that inertial particles at high Re_* are harder to stop.

In general, the role of particle inertia in nonsuspended sediment transport can be twofold. On the one hand, entrainment by or supported by particle-bed impacts may be able to supply the transport layer with bed particles and thus compensate captures of transported particles by the bed (section 4.1). This mechanism gives rise to a shear stress threshold associated with impact entrainment. On the other hand, although the mean turbulent flow is usually too weak to initiate transport (which instead usually requires turbulent fluctuation events, see section 3), it may be able to sustain the motion of particles that are already in transport. This mechanism gives rise to a physical process-based definition of transport capacity and a shear stress threshold, which has often been misidentified as an entrainment threshold by Shields (1936) and others (section 4.2). Various models for both shear stress thresholds that have been proposed in the literature are compared with one another in section 4.3.

4.1. Impact and Impact-Supported Entrainment

Bagnold (1941) was the first to recognize that impact entrainment is crucial for sustaining aeolian saltation transport. Based on his wind tunnel and field observations, he explained (Bagnold, 1941, p. 102), "In air, the grains, when once set in motion along the surface, strike other stationary grains, and either themselves bounce high (a distance measured in hundreds if not thousands of grain diameters) into the relatively tenuous fluid, or eject other grains upwards to a similar height." Largely because of Bagnold's observations, the statistics of particle impacts onto a static granular packing have been subject of many experimental and theoretical investigations (section 4.1.1). Bagnold (1941, p. 102) also believed that impact entrainment is negligible for fluvial bedload transport: "If the physics of this impact-ejection mechanism is applied to sand in water, it is found that the impact momentum of the descending grains is insufficient to raise surface grains to a height greater than a small fraction of one grain diameter." However, Bagnold, and numerous researchers after him, did not consider that even a marginal uplift of a bed particle can make it much easier for a turbulent fluctuation event to entrain it (section 4.1.2) and that once bedload transport becomes sufficiently strong, multiple particle-bed impacts occur in so short sequence that the bed can no longer be considered as static. In fact, for continuous transport, recent studies revealed that impact entrainment alone can sustain bedload transport (section 4.1.3).

4.1.1. Impact of an Incident Particle Onto a Static Granular Packing

The collision process between an incident particle and a static granular packing has been investigated in many experimental (Ammi et al., 2009; Bachelet et al., 2018; Beladjine et al., 2007; Chen et al., 2019; Clark et al., 2012, 2016; Clark, Petersen, et al., 2015; Mitha et al., 1986; Nishida et al., 2004; Oger et al., 2008; Rioual et al., 2000, 2003; Tanaka et al., 2002; Werner, 1990) and theoretical (Anderson & Haff, 1988, 1991; Bourrier et al., 2008; Crassous et al., 2007; Comola & Lehning, 2017; Duan, Zhu, & Zheng, 2013; Haff & Anderson, 1993; Ho et al., 2012; Huang et al., 2017; Kok & Renno, 2009; Lämmel et al., 2017; McElwaine et al., 2004; Namikas, 2006; Oger et al., 2005, 2008; Tanabe et al., 2017; Valance & Crassous, 2009; Werner

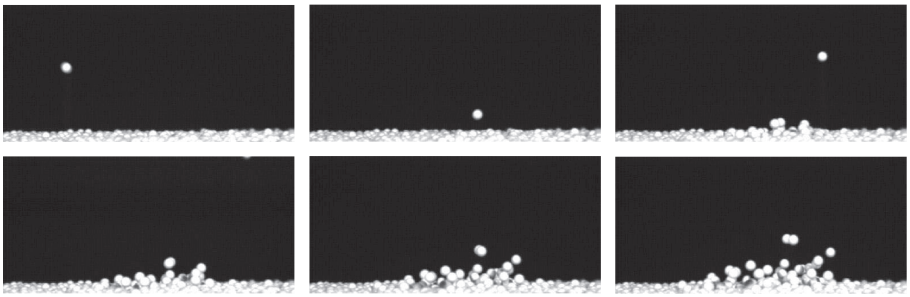

Figure 9. From Beladjine et al. (2007), high-speed images of the impact of an incident particle on a static granular packing. The time step between two successive images is 4 ms. Copyright 2007 American Physical Society.

& Haff, 1988; Xing & He, 2013; Zheng et al., 2005, 2008) studies in order to better understand aeolian saltation transport and other geophysical phenomena (e.g., rockfall (Bachelet et al., 2018; Bourrier et al., 2008)); see also (Dong et al., 2002; Gordon & McKenna Neuman, 2009, 2011; McEwan et al., 1992, 2004; Nalpanis et al., 1993; Rice et al., 1995, 1996; White & Schulz, 1977; Willetts & Rice, 1986, 1989) for collision statistics during ongoing aeolian saltation transport. In typical experiments, a spherical incident particle of diameter d and mass m is shot (e.g., by an airgun) at a given speed $\mathbf{v_i}$ and angle θ_i onto a static packing of spheres of the same size. As shown in Figure 9 and sketched in Figure 10, as a result of its impact on the packing, the incident particle may rebound (velocity $\mathbf{v_r}$, angles θ_r, ϕ_r) and/or eject bed particles into motion (number N_e, velocity $\mathbf{v_e}$, angles θ_e, ϕ_e), where a particle is typically counted as ejected if its center is lifted by more than d above the top of the bed surface. The statistics of this process has been the subject of several recent experimental and numerical studies (e.g., Ammi et al., 2009; Beladjine et al., 2007; Tanabe et al., 2017) (note that experimental studies that used only one camera measured quantities projected into the incident plane: $v^{2D}_{r(e)} \equiv \sqrt{v^2_{r(e)x} + v^2_{r(e)z}}$ and $\tan\theta^{2D}_{r(e)} \equiv \tan\theta_{r(e)}/\cos\phi_{r(e)}$). These studies have yielded the following insights:

(i) The incident particle loses much more energy in head-on than in grazing collisions. In fact, the average restitution coefficient and its two-dimensional projection obey the following empirical relationships for $10° \leq \theta_i \leq 90°$:

$$\bar{e} \equiv \overline{|\mathbf{v_r}|}/|\mathbf{v_i}| = A - B\sin\theta_i, \tag{12a}$$

$$\overline{e^{2D}} \equiv \overline{v_r^{2D}}/|\mathbf{v_i}| = A^{2D} - B^{2D}\sin\theta_i, \tag{12b}$$

where the overbar denotes an ensemble average over collision experiments, and the A and B coefficients are empirical constants that vary slightly between the studies (e.g., $A \approx A^{2D} \approx 0.87$, $B \approx 0.62$ Ammi et al., 2009, and $B^{2D} \approx 0.72$ Beladjine et al., 2007).

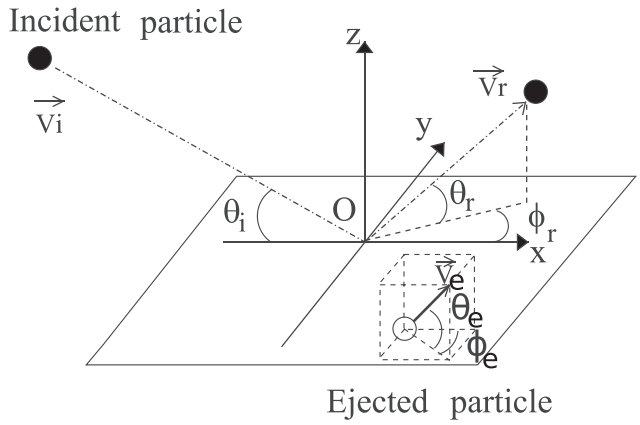

Figure 10. Sketch of collision process.

(ii) The average vertical restitution coefficient exceeds unity at small impact angles and obeys the following empirical relationship for $10° \leq \theta_i \leq 90°$:

$$\overline{e_z} \equiv \overline{v_{rz}}/v_{iz} = A_z/\sin\theta_i - B_z, \tag{13}$$

where $A_z \approx 0.3$ and $B_z \approx 0.15$ for the experiments by Beladjine et al. (2007). Pähtz, Liu, et al. (2020) suggested the following modification of equation (13):

$$\overline{e_z} = A^{2D}/\sqrt{\sin\theta_i} - B^{2D}. \tag{14}$$

This modification, which is also consistent with the experimental data, ensures the correct asymptotic behavior of the average rebound angle, $\overline{\theta_r} \sim \sqrt{\theta_i}$ (Lämmel et al., 2017), in the limit $\theta_i \to 0$.

(iii) The average rebound angle and its two-dimensional projection are independent of the incident speed, increase with the impact angle, and obey the following empirical relationships for $10° \leq \theta_i \leq 90°$:

$$\overline{\theta_r} = \theta_0 + \chi\theta_i, \tag{15a}$$

$$\sin\overline{\theta_r^{2D}} = \overline{e_z}\sin\theta_i/\overline{e^{2D}} \tag{15b}$$

where $\theta_0 \approx 20°$ and $\chi \approx 0.19$ for the experiments by Ammi et al. (2009).

(iv) The average energy that the incident particle transfers to the bed is spent for the ejection of bed particles. That is, it is proportional to the average of the sum of the kinetic energy of ejected particles ($E_e = \frac{1}{2}m\mathbf{v_e}^2$ and $E_e^{2D} = \frac{1}{2}mv_e^{2D2}$). In fact, the following empirical relationships are obeyed for $10° \leq \theta_i \leq 90°$:

$$\overline{N_e}\,\overline{E_e} = r(1-\overline{e}^2)E_i, \tag{16a}$$

$$\overline{N_e}\overline{E_e^{2D}} = r^{2D}(1-\overline{e^{2D}}^2)E_i, \tag{16b}$$

where $r \approx 0.04$ and $r^{2D} \approx 0.038$ for the experiments by Ammi et al. (2009). Note that r and r^{2D} decrease with the coordination number of the particle packing (Rioual et al., 2003).

(v) The average number of ejected particles is a linear function of the incident speed for $10° \leq \theta_i \leq 90°$:

$$\overline{N_e} = n_0(1-\overline{e}^2)[|\mathbf{v_i}|/(\zeta\sqrt{gd}) - 1] \simeq n_0(1-\overline{e^{2D}}^2)[|\mathbf{v_i}|/(\zeta\sqrt{gd}) - 1], \tag{17}$$

where $n_0 \approx 13$ and $\zeta \approx 40$ for the experiments by Ammi et al. (2009). Note that n_0 decreases with the coordination number of the particle packing (Rioual et al., 2003).

(vi) The average horizontal and lateral velocities of ejected particles are nearly independent of the incident velocity, but the average vertical velocity increases slightly with the incident velocity and is independent of the impact angle for $10° \leq \theta_i \leq 90°$ (Ammi et al., 2009):

$$\overline{v_{rx}^2} \approx \overline{v_{ry}^2} \approx 4gd, \tag{18a}$$

$$\overline{v_{rz}}/\sqrt{gd} \approx 1.06(|\mathbf{v_i}|/\sqrt{gd})^{1/4}, \tag{18b}$$

$$\overline{v_{rz}^2}/gd \approx 1.46(|\mathbf{v_i}|/\sqrt{gd})^{1/2} \tag{18c}$$

(vii) The average ejection angle $\overline{\theta_e}$ is constant for $10° \leq \theta_i \leq 90°$ (Ammi et al., 2009). However, its projection into the incident plane increases with the impact angle (Beladjine et al., 2007):

$$\overline{\theta_e^{2D}} \approx \frac{\pi}{2} + 0.1\left(\theta_i - \frac{\pi}{2}\right). \tag{19}$$

4.1.1.1. Open Problem: Behavior of the Rebound Probability

Mitha et al. (1986) measured that about 94% of all impacting particles are not captured by the bed (i.e., they successfully rebound). However, the range of impact velocities in their experiments was very narrow ($|\mathbf{v_i}| \in (106, 125)\sqrt{gd}$). More systematic measurements of the rebound probability P_r are needed.

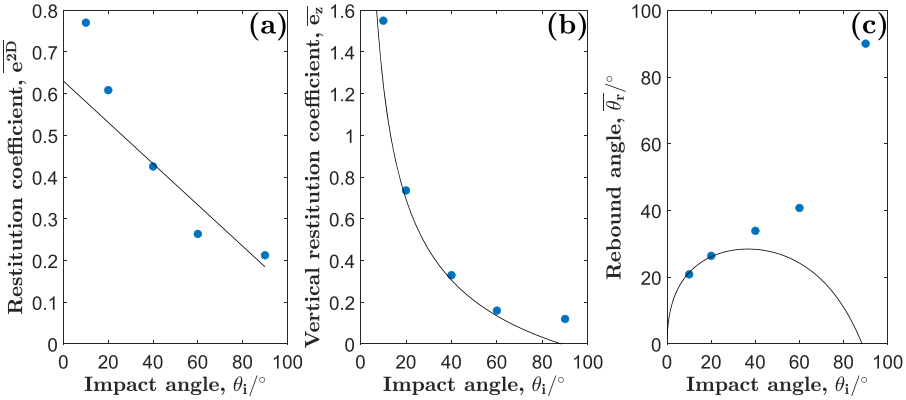

Figure 11. Test of the analytical expressions by Lämmel et al. (2017) that describe the particle rebound of an impacting particle in the limit of shallow impact angles ($\theta_i \lesssim 20°$). (a) Average rebound restitution coefficient $\overline{e^{2D}}$, (b) average vertical rebound restitution coefficient $\overline{e_z}$, and (c) average rebound angle $\overline{\theta_r}$ versus impact angle θ_i. Symbols correspond to experimental data by Beladjine et al. (2007). Solid lines correspond to equations (20)–(22).

Studies have attempted to physically describe both the rebound (Lämmel et al., 2017; Namikas, 2006; Zheng et al., 2005, 2008) and ejection dynamics (Comola & Lehning, 2017; Crassous et al., 2007; Ho et al., 2012; Kok & Renno, 2009; Lämmel et al., 2017; McElwaine et al., 2004; Valance & Crassous, 2009). For example, the rebound dynamics can be analytically calculated for an idealized packing geometry and a given rebound location assuming a binary collision between the incident particle and hit bed particle. From averaging over all possible rebound locations, one can then determine the rebound angle and restitution coefficient distributions. Using this procedure, Lämmel et al. (2017) derived the following expressions for $\overline{e^{2D}}$, $\overline{e_z}$, $\overline{\theta_r^{2D}}$, and P_r in the limit of shallow impact angles ($\theta_i \lesssim 20°$):

$$\overline{e^{2D}} = \beta_r - (\beta_r^2 - \alpha_r^2)\theta_i/(2\beta_r), \tag{20}$$

$$\overline{e_z} = -\beta_r + (2/3)(\alpha_r + \beta_r)\sqrt{2/\theta_i}, \tag{21}$$

$$\overline{\theta_r^{2D}} = \overline{e_z}\theta_i/\overline{e^{2D}} \approx (2/3)(1 + \alpha_r/\beta_r)\sqrt{2\theta_i} - \theta_i, \tag{22}$$

$$P_r = 1 - \frac{1 + \ln \xi}{\xi}, \quad \text{with} \quad \xi \equiv \max\left[1, \frac{9\sqrt{2}(1 + \alpha_r/\beta_r)^2\theta_i \mathbf{v_i}^2}{4\sqrt{3}gd}\right], \tag{23}$$

where α_r and β_r are the normal and tangential rebound restitution coefficients, respectively, in the impact plane, which depend on the binary normal and tangential restitution coefficient (i.e., the ratio between the postcollisional and precollisional relative particle velocity component normal and tangential, respectively, to the contact plane). Figure 11 compares equations (20)–(22) with the experimental data by Beladjine et al. (2007) using the values $\alpha_r = 0.2$ and $\beta_r = 0.63$, which Lämmel et al. (2017) obtained from fitting the numerical solution of the full problem (i.e., not limited to $\theta_i \lesssim 20°$) to the experimental data. The agreement with the data with $\theta_i \lesssim 20°$ is acceptable considering that the theory has been derived mostly from first physical principles. Equation (23), which is the modified version of equations (41) and (42) of Lämmel et al. (2017) that these authors describe in their text, cannot be tested because of the lack of systematic measurements of the rebound probability P_r. A widely used alternative expression for P_r was given by Anderson and Haff (1991): $P_r \approx 0.95[1 - \exp(-\gamma_r|\mathbf{v_i}|)]$. However, this expression is empirical and contains the dimensional parameter γ_r (note that Andreotti (2004) assumed $\gamma_r \propto 1/\sqrt{gd}$). Because $\overline{e_z} \gtrsim 1$, which is a precondition for sustained aeolian saltation transport (from energy conservation), requires shallow impact angles, equations (20)–(23) can be used for the theoretical modeling of aeolian saltation transport.

For the description of the ejection dynamics, there have been two distinct approaches: solving an underdetermined momentum and/or energy balance of the particles involved in the collision process

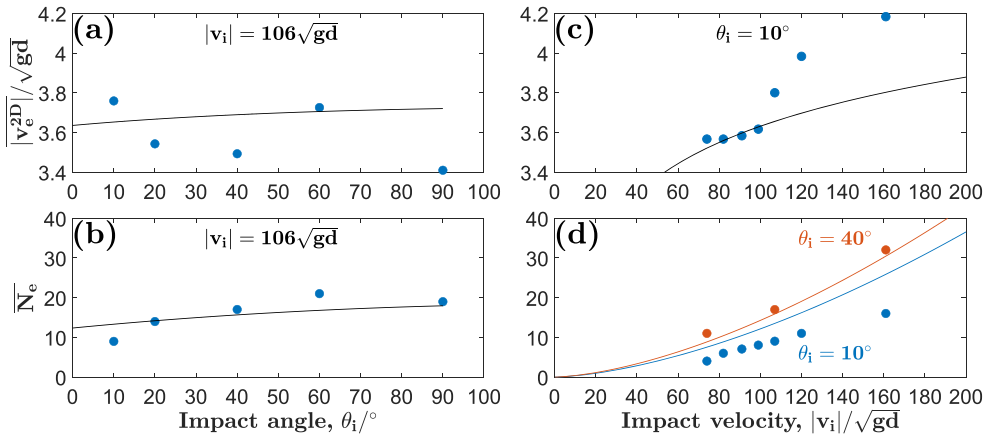

Figure 12. Test of the analytical expressions by Lämmel et al. (2017) that describe the ejection of bed surface particles caused by the splash of an impacting particle. (a, c) Nondimensionalized average ejection velocity $\overline{|\mathbf{v}_e^{2D}|}$ and (b, d) average number of ejected particles $\overline{N_e}$ versus (a, b) impact angle θ_i and (c, d) nondimensionalized impact velocity $|v_i|/\sqrt{gd}$. Symbols correspond to experimental data by Beladjine et al. (2007). Solid lines correspond to equations (25) and (27) combined with the approximation $\overline{|\mathbf{v}_e|} \simeq \overline{|\mathbf{v}_e^{2D}|}$.

(Kok & Renno, 2009; Comola & Lehning, 2017) and treating the collision process as a sequence of binary collisions, in which the energy is split between the collisional partners (i.e., incident and bed particle or two bed particles) (Crassous et al., 2007; Ho et al., 2012; Lämmel et al., 2017; McElwaine et al., 2004; Valance & Crassous, 2009). A minimal numerical model that is based on the latter approach has been able to reproduce experimental data of both the rebound and ejection dynamics, including the measured log-normal distribution of the vertical ejection velocity (Crassous et al., 2007). Furthermore, based on this approach and the derivation by Ho et al. (2012), Lämmel et al. (2017) derived the following analytical expression for the distribution of the ejection energy E_e:

$$\begin{aligned} P(E_e) &= \frac{1}{\sqrt{2\pi}\sigma E_e}\exp\left[-\frac{(\ln E_e - \mu)^2}{2\sigma^2}\right], \quad \text{with} \\ \sigma &= \sqrt{\lambda}\ln 2, \\ \mu &= \ln[(1-\bar{e}^2)E_i] - \lambda\ln 2, \\ \lambda &= 2\ln[(1-\bar{e}^2)E_i/(mgd)], \end{aligned} \tag{24}$$

from which they further obtained expressions for $\overline{N_e}$, $\overline{E_e}$, and $\overline{|\mathbf{v}_e|}$:

$$\overline{N_e} = r\frac{(1-\bar{e}^2)E_i}{2\overline{E_e}}\operatorname{erfc}\left[\frac{\ln(mgd)-\mu}{\sqrt{2}\sigma}\right], \tag{25}$$

$$\overline{E_e} = mgd[(1-\bar{e}^2)E_i/(mgd)]^{1-(2-\ln 2)\ln 2}, \tag{26}$$

$$\overline{|\mathbf{v}_e|} = \frac{\operatorname{erfc}\{[\ln(mgd)-\mu-\sigma^2/2]/(\sqrt{2}\sigma)\}}{\operatorname{erfc}\{[\ln(mgd)-\mu]/(\sqrt{2}\sigma)\}}\sqrt{2}\exp(\mu/2+\sigma^2/8), \tag{27}$$

where $r = 0.06$. Figure 12 shows that these expressions are roughly consistent with experimental data considering that they have been derived mostly from first physical principles. Note that equations (20)–(27), after some minor modifications, can also be applied to situations in which the size of the impacting particle differs from the size of the particles of the granular packing (Lämmel et al., 2017). Further note that equation (38) of Lämmel et al. (2017), which is the equivalent of equation (27), contains a typo (a σ is missing in the denominator).

4.1.1.2. Open Problem: Impacts Onto Mobile Beds

The findings from collision experiments with static beds are often applied to model fluvial bedload (Berzi et al., 2016; Pähtz, Liu, et al., 2020) and aeolian saltation transport (Andreotti, 2004; Berzi et al., 2016, 2017; Bo et al., 2017; Claudin & Andreotti, 2006; Creyssels et al., 2009; Huang et al., 2014; Jenkins et al., 2010; Jenkins & Valance, 2014, 2018; Kok, 2010a; Kok & Renno, 2009; Lämmel et al., 2012; Lämmel & Kroy, 2017; Pähtz et al., 2012; Pähtz, Liu, et al., 2020; Wang & Zheng, 2014, 2015). However, if the time between successive particle-bed impacts is too short for a bed particle to fully recover from each impact, it can accumulate more and more kinetic energy with each impact. Hence, for a sufficiently large impact frequency and impact energy (both increase with the sediment transport rate Q), the bed can no longer be treated as static and the findings from such collision experiments may no longer apply. For example, the simultaneous impact of two particles onto the bed leads to a significantly different outcome compared with the situation in which each particle impacts separately (Duan, Zhu, & Zheng, 2013). For these reasons, future studies should try to systematically investigate the effects of disturbances from the static bed on the outcome of a particle-bed impact.

4.1.1.3. Open Problem: Effects of Particle Shape and Size Distribution

Chen et al. (2019) investigated the particle-bed collision process for natural sand particles, which exhibit nonspherical shapes and nonuniform particle size distributions. They found significant quantitative and qualitative deviations from the laws describing spherical, uniform particles. More systematic experimental studies are needed to pinpoint the exact manner in which particle shape and size distribution affect the collision process.

4.1.1.4. Controversy: Effects of Viscous Damping

Binary collisions that occur within an ambient fluid can be significantly damped depending on the Stokes number $St \equiv s|\mathbf{v_r}|d/(9\nu_f)$ (Gondret et al., 2002; Maurin et al., 2015; Schmeeckle, 2014; Yang and Hunt, 2006), where $\mathbf{v_r}$ is the relative particle velocity just before a collision. For example, experiments suggest that the effective normal restitution coefficient ϵ of a damped binary collision vanishes for $St \lesssim 10$ (Gondret et al., 2002). The question that then arises is how does viscous damping affect the rebound and ejection dynamics of a particle-bed impact. Berzi et al. (2016, 2017) assumed that the rebound restitution coefficients $\overline{e^{2D}}$ and $\overline{e_z}$, like ϵ, also vanish when St falls below a critical value. In contrast, DEM-based simulations indicate that the dynamics of saltation (Pähtz & Durán, 2018a) and particularly bedload transport (Drake & Calantoni, 2001; Elghannay & Tafti, 2017; Maurin et al., 2015; Pähtz & Durán, 2017, 2018a, 2018b) are not much affected by the value of ϵ, which suggests that the rebound and ejection dynamics of a particle-bed impact may not be much affected by viscous damping. A possible explanation for this unexpected behavior could be that a nearly elastic particle-bed impact may be roughly equivalent to a sequence of binary collisions between particles in contact at the instant of impact. In fact, a theoretical model based on this hypothesis reproduced experiments of the collision process (Crassous et al., 2007; Valance & Crassous, 2009). For the perfectly elastic case ($\epsilon = 1$), the impactor would then transfer all of its momentum in the direction normal to the contact plane to the particle it hit (which is the expected result of an elastic binary collision between a mobile and a resting particle) and, therefore, rebound with zero normal momentum. A complete loss of normal momentum is also expected for the completely inelastic case ($\epsilon = 0$). This suggests that the rebound process is not much affected by ϵ, which would imply that the momentum in the direction tangential to the contact plane is what mainly matters. Collision experiments in an ambient viscous liquid could resolve this controversy.

4.1.1.5. Open Problem: Effects of Cohesion

Cohesive interparticle forces, including van der Waals (Castellanos, 2005), water adsorption (Herminghaus, 2005), and electrostatic forces (Lacks and Sankaran, 2011), become significant in the collision process for sufficiently small particles (on Earth, for $d \lesssim 100\mu$m) because they scale with a lower power p in the particle diameter ($F_{\text{coh}} \sim d^p$) than the gravity force ($F_g \sim d^3$). However, collision experiments with so small particles have not been carried out because it is very difficult to detected their dynamics with cameras. Numerical studies are also very scarce. To the authors' knowledge, only the very recent study by Comola, Gaume, et al. (2019) studied cohesive forces, by implementing them in a numerical DEM-based model of aeolian saltation transport. These authors investigated the impact of a particle onto the bed for a large range of the strength of cohesive forces and found that cohesion decreases $\overline{N_e}$ via solidifying the bed, while $\bar{e}$ slightly and $|\mathbf{v_e}|/|\mathbf{v_i}|$ considerably increase. However, more systematic studies are needed to confirm these results and determine scaling laws describing the effects of cohesion on the outcome of a particle-bed impact.

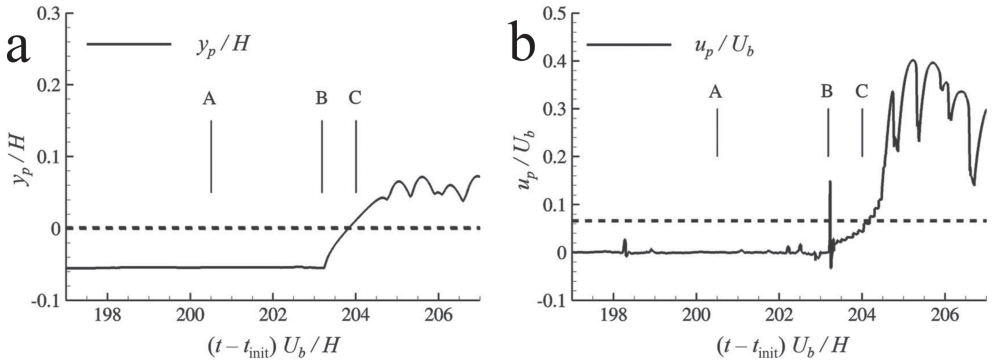

Figure 13. From Vowinckel et al. (2016), time evolution of a typical erosion event. At time instant *A*, a bed surface particle is at rest. At time instant *B*, it is hit by an impacting transported particle. The impact causes a slight dislocation off its initial position. Once slightly lifted, the particle protrudes into the flow, enhancing the flow forces acting on it. This enhancement in combination with much-larger-than-average flow velocities during a turbulent fluctuation event (Figure 14) leads to entrainment (time instant *C*), as indicated by the nondimensionalized (a) vertical displacement (y_p/H) and (b) particle velocity (u_p/U_b) exceeding critical values (dashed lines). Copyright 2016 Taylor & Francis Group.

4.1.2. Collision-Enhanced Turbulent Entrainment in Fluvial Bedload Transport

To the authors' knowledge, only a single study has resolved the effects of particle-bed impacts on entrainment by turbulent fluctuation events in bedload transport (Vowinckel et al., 2016). However, this study provided one of the largest, if not the largest, data sets of entrainment events associated with fluvial bedload transport with a very high resolution in space and time. Vowinckel et al. (2016) coupled direct numerical simulations (DNS) for the fluid phase (i.e., the Navier-Stokes equations are directly solved without using turbulent closure assumptions) with DEM simulations for the particle phase (i.e., particles interact with each other according to a contact model) using the immersed boundary method, which fully resolves the geometry of particles (and thus the hydrodynamic forces acting on them) without remeshing the grid during their motion (Vowinckel et al., 2014). Because of the sophistication of this numerical method (i.e., resolving all relevant physical processes at very small scale), the produced data can be considered to be very reliable. The simulated setup consisted of two layers of grains resting on the simulation bottom wall, the lower of which was fixed, arranged in a hexagonal packing, and exposed to a unidirectional open channel flow of thickness $H = 9d$ (Reynolds number $Re \equiv U_b H/\nu_f = 2941$, where U_b is the bulk flow velocity). The Shields number was at $\Theta = 0.0255$, which is about 25% below the Shields curve for the simulated condition. That is, the nondimensionalized transport rate Q_* was likely below the value associated with critical transport conditions (see section 1), which is consistent with Vowinckel et al. (2016) reporting that only 3% of all particles were in motion on average. For these conditions, it was found that, in the vast majority of cases (overall

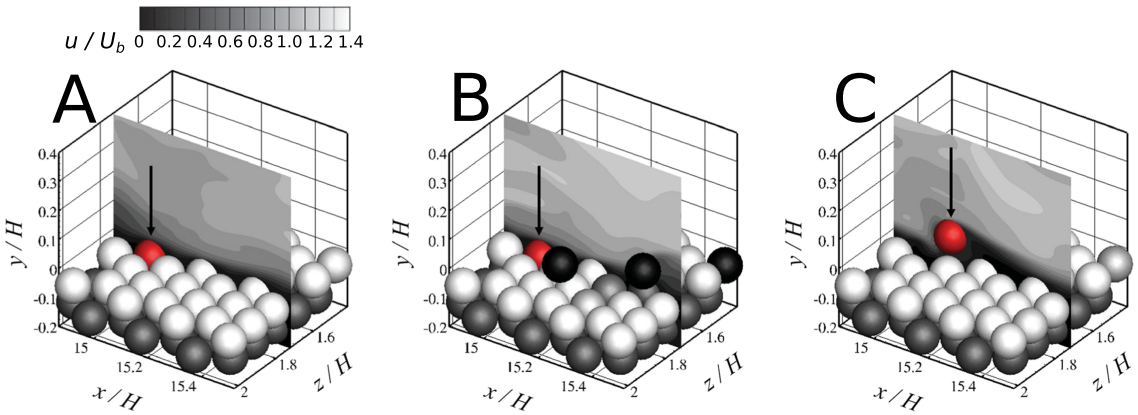

Figure 14. From Vowinckel et al. (2016), zoom into the simulation domain and contour plots of the instantaneous streamwise flow field (u/U_b) during a typical erosion event of a target particle (red). The color (gray, white, and black) corresponds to (nonerodible, resting, and transported) particles. Time instants *A*, *B*, and *C* are as in Figure 13. Copyright 2016 Taylor & Francis Group.

96.5%), a particle-bed impact and a subsequent turbulent fluctuation event are responsible for entrainment, even when one or more of the six pockets surrounding the target particle were not occupied by other particles (in which case the target particle experiences a larger exposure to the flow). For an entrainment event following this pattern, Figure 13 shows the time evolution of (a) the vertical displacement (y_p) and (b) velocity of a bed surface particle (u_p), while Figure 14 shows the simulation domain and contour plots of the instantaneous flow field. It can be seen that, at the instant of entrainment, the instantaneous streamwise flow velocity (u) exhibits larger-than-average values (Figure 14c). In fact, Vowinckel et al. (2016) reported that 82% of the entrainment events were caused by *sweep*, characterized by positive fluctuations of u and negative fluctuations of the flow velocity component in the direction normal to the bed.

The results by Vowinckel et al. (2016) were obtained for an idealized hexagonal packing and may not necessarily apply in their full extent to realistic sediment beds found in nature. While for a hexagonal packing, the vast majority of entrainment events are initiated by particle-bed impacts, it remains unclear whether this holds true also for natural sediment beds, in which bed surface particles tend to protrude much more strongly into the flow. On the one hand, a larger protrusion makes it easier for a turbulent fluctuation event to entrain a bed surface particle without a preceding particle-bed impact. On the other hand, particle-bed impacts can result in entrainment without the need of a turbulent fluctuation event (see section 4.1.3).

4.1.3. The Role of Particle-Bed Impacts in Sustaining Continuous Sediment Transport

Pähtz and Durán (2017) numerically studied the role of particle-bed impacts in sustaining continuous nonsuspended sediment transport for transport conditions characterized by a large range of the Shields number Θ, density ratio s, and Galileo number Ga. These authors coupled quasi-two-dimensional DEM simulations for the particle phase with a Reynolds-averaged description of the fluid hydrodynamics that neglects turbulent fluctuations around the mean turbulent flow. While such simulations cannot resolve entrainment by turbulent fluctuation events, they are able to elucidate the importance of entrainment by particle-bed impacts relative to entrainment by the mean turbulent flow. Also, the absence of turbulent fluctuations eliminates transport intermittency in the sense that transport in the simulation domain is either continuous (i.e., periods of rest are absent) or it completely stops after a finite time (except for potential creeping, see section 2.3). From their simulations, Pähtz and Durán (2017) determined an effective value of the local particle velocity averaged over elevations near the bed surface (V_b) relative to the critical velocity that is needed to escape the potential wells set by the pockets of the bed surface ($\propto \sqrt{\hat{g}d}$, where $\hat{g} = [1 + 1/(s + C_m)]$ is the value of the gravity constant reduced by the buoyancy and added mass force, with $C_m = 1/2$ the added mass coefficient). They found that $V_b/\sqrt{\hat{g}d}$ exhibits a universal approximately constant value of order unity for continuous nonsuspended sediment transport if the following constraint is obeyed:

$$Im \equiv Ga\sqrt{s + C_m} \gtrsim 20 \quad \text{or} \quad \Theta \gtrsim 5/Im. \tag{28}$$

The interpretation of $V_b/\sqrt{\hat{g}d} \approx$ const is that particles located near the bed surface (which includes both particles of the bed and transported particles) are on average at the verge of leaving it or being captured by its potential wells, consistent with a dynamic equilibrium that is solely controlled by particle inertia. This implies that entrainment occurs solely due to the action of particle-bed impacts. Consistently, Pähtz and Durán (2017) observed from visually inspecting simulations that obey equation (28) that every entrainment event is initiated by a particle-bed impact, usually with a small time delay between the instant of impact and beginning visible motion. In contrast, for transport conditions that do not obey equation (28), $V_b/\sqrt{\hat{g}d}$ exhibits a smaller value, which means that the mean turbulent flow must assist particles located near the bed surface in escaping the potential wells. For bedload transport, the findings by Pähtz and Durán (2017) were independent of the effective normal restitution coefficient ϵ for a damped binary collision, which indicates that viscous damping does not suppress impact entrainment (see also the discussion of viscous damping in section 4.1.1.4).

The constraint set by equation (28) is obeyed by the vast majority of sediment transport regimes, including turbulent fluvial bedload transport. That is, in the absence of turbulent fluctuation events, only viscous fluvial bedload transport is significantly affected by the entrainment of bed sediment by the mean turbulent flow. The numerical prediction that impact entrainment dominates entrainment by the mean turbulent flow in turbulent fluvial bedload transport is supported by experiments (Heyman et al., 2016; Lee & Jerolmack, 2018). Lee and Jerolmack (2018) studied bedload transport driven by a water flow in a quasi-two-dimensional flume (i.e., its lateral dimension was only slightly larger than the particle

diameter d). Because the size of turbulent structures, and thus turbulent fluctuation events, is strongly suppressed when the system dimensions are so strongly narrowed down, their experiments are somewhat comparable to the numerical simulations by Pähtz and Durán (2017) described above. Lee and Jerolmack (2018) fixed the water discharge and fed particles at the flume entrance with varying frequency f_{in} (the tested range of f_{in} was likely associated with a transport rate below capacity). In contrast to similar older experiments (Ancey et al., 2008; Böhm et al., 2004; Heyman et al., 2013), the bed was relatively deep, which ensured the complete dissipation of shock waves associated with particle-bed impacts (Rioual et al., 2003). Lee and Jerolmack (2018) reported that, for all tested conditions, every entrainment event is initiated by a particle-bed impact, exactly as numerically predicted, and that the number of transported particles roughly scales with the energy transferred to the bed by rebounding particles. The latter finding is remarkably similar to the scaling of the average ejected particle number $\overline{N_e}$ in static bed experiments (e.g., see equation (25)). Lee and Jerolmack (2018) also measured the frequency of particles passing an illuminated window near the flume exit (f_{out}). They found that $f_{\mathrm{out}} < f_{\mathrm{in}}$ for sufficiently small f_{in} and that $f_{\mathrm{out}} \approx f_{\mathrm{in}}$ once f_{in} exceeds a critical value.

Similar observations were made by Heyman et al. (2016), who used a water flume with a narrow but larger width ($W = 5d$) than Lee and Jerolmack (2018) and who also used a relatively deep bed. Heyman et al. (2016) measured that the entrainment rate was proportional to the number of transported particles per unit bed area, which is indirect evidence supporting that the majority of entrainment events is caused by particle-bed impacts. These authors also reported for all their tested feeding frequencies f_{in} that the entrainment and deposition rate are equal to one another, in resemblance of the measurement $f_{\mathrm{out}} \approx f_{\mathrm{in}}$ for sufficiently large f_{in} by Lee and Jerolmack (2018). Note that one expects the approximate equality $f_{\mathrm{out}} \approx f_{\mathrm{in}}$ to break down for large f_{in} (when the influx exceeds transport capacity) because increasing momentum transfer from fluid to particles slows down the flow, which at some point can no longer sustain the particle motion.

The results by Heyman et al. (2016) and Lee and Jerolmack (2018) suggest that mainly (but not solely) particles that were previously in motion are being entrained by particle-bed impacts. Otherwise, there would be no reason to expect that the entrainment and deposition rate are relatively equal to one another for a large range of f_{in} (instead, one would expect that only for transport capacity). This can be explained when assuming that particle-bed impacts are effective in mobilizing a bed particle almost only when the bed particle exceeds a critical energy level just before the impact. On the one hand, this assumption would explain why bed particles that have never been transported only rarely become mobilized by particle-bed impacts. On the other hand, this assumption is consistent with the fact that a transported particle that has just been captured by a bed pocket exhibits a residual kinetic energy that takes some time to be completely dissipated, during which it can be remobilized by an impact from a particle coming from behind. It seems that, once f_{in} exceeds a critical value, there is usually a particle coming from behind in time and transported particles can only rarely settle completely even though they may temporarily stop. Temporary particle stops and reentrainment make transported particles tend to move in clusters near the flume exit even though they are apart from one another at the flume entrance, which is exactly what Lee and Jerolmack (2018) reported and what can be observed in the numerical simulations by Pähtz and Durán (2018a, Movie S2).

There is evidence that the presumed impact entrainment mechanism described above may play an important role in nonsuspended sediment transport in general. In fact, in simulations of steady, homogenous sediment transport using DEM-based numerical models that *neglect turbulent fluctuations around the mean turbulent flow*, the steady state transport rate Q exhibits a discontinuous jump at a fluid shear stress τ_t^{ImE} (Carneiro et al., 2011, 2013; Clark, Shattuck, et al., 2015; Clark et al., 2017; Pähtz & Durán, 2018a). That is, for $\tau \geq \tau_t^{\mathrm{ImE}}$, transport is significantly larger than zero ($Q > 0$) and continuous, whereas $Q \simeq 0$ when $\tau < \tau_t^{\mathrm{ImE}}$. Assuming that only impact entrainment took place in all these simulations (as the mean turbulent flow is too weak for entrainment, see above), τ_t^{ImE} can be identified as the impact entrainment threshold. The discontinuous jump of Q thus means that, in order for impact entrainment to sustain transport, a critical transport rate must be exceeded. Like the critical feeding frequency in the experiments by Lee and Jerolmack (2018), this critical transport rate may be interpreted as the value above which most transported particles can be captured only temporarily by bed pockets as they are usually hit in time and thus reentrained by an impact from a particle coming from behind before dissipating too much of their kinetic energy. However, it is crucial to point out that impact entrainment of bed particles that have never been transported occasionally occurs in DEM-based sediment transport simulations as well, which is why a further interpretation of the physical

origin of the discontinuous jump of Q has been proposed (Pähtz and Durán, 2018a). It states that, at a critical transport rate, bed surface particles do no longer sufficiently recover between successive particle-bed impacts. They thus accumulate energy between successive impacts until they are eventually entrained. In contrast, for subcritical transport rates, particles sufficiently recover between impacts so that impact entrainment is inefficient, causing transport to eventually stop. The two interpretations above are based only on the energy of bed particles or temporarily captured transported particles. In contrast, in the context of an idealized continuous rebound modeling framework (see section 4.2), an alternative mechanism based on the critical amount of energy E_c that bed particles need to acquire for entrainment (more precisely, for entering a quasi-continuous motion) can explain the discontinuous jump of Q without further assumptions (see section 4.2.1).

4.1.3.1. Open Problem: Precise Mechanism of Impact Entrainment in Continuous Transport

The proposed impact entrainment mechanisms described above and in section 4.2.1 are mostly speculative and based on indirect experimental or theoretical evidence, or idealized models. More direct investigations are therefore needed to uncover the precise nature of impact entrainment and the degree to which each of these mechanisms contributes. Such investigations may also help to better understand fluctuations of nonsuspended sediment transport. For example, the longer the average time t_{conv} it takes for transport to stop (in the absence of turbulent fluctuations around the mean turbulent flow) when $\tau < \tau_t^{\text{ImE}}$ (t_{conv} obeys a critical scaling behavior at τ_t^{ImE}, see section 2.4), the larger are the transport autocorrelations, which can be quite substantial in fluvial bedload transport (Ancey et al., 2006, 2008, 2015; Dinehart, 1999; Drake et al., 1988; Heathershaw & Thorne, 1985; Martin et al., 2012).

4.1.3.2. Open Problem: Precise Definitions of Intermittent and Continuous Transport

As explained above, in simulations of steady, homogenous sediment transport using DEM-based numerical models that neglect turbulent fluctuations, the steady transport rate Q (in a time-averaged sense) exhibits a discontinuous jump at the impact entrainment threshold τ_t^{ImE}. In contrast, for most natural conditions, fluid entrainment by turbulent events can reinitiate transport whenever it temporarily stops, meaning that Q remains significant below τ_t^{ImE} (Carneiro et al., 2011). Hence, since turbulent events capable of fluid entrainment occur only at an intermittent basis (see section 3), Pähtz and Durán (2018a) suggested that τ_t^{ImE} is equivalent to the continuous transport threshold for most natural conditions and that transport becomes intermittent below τ_t^{ImE}. However, provided that fluid entrainment does occur, it is certain to find particles being in transport below τ_t^{ImE} at any given instant in time in the large-system limit, which renders the distinction between intermittent and continuous transport somewhat ambiguous. For this reason, Pähtz and Durán (2018a) referred to intermittent conditions as those that deviate significantly from transport capacity (defined as in section 4.2.2). Consistently, Martin and Kok (2018) and Comola, Kok, et al. (2019) found from aeolian field experiments that the long-term-averaged transport remains at capacity when the fraction f_Q of active saltation transport is close to unity, that is, when transport quantified over a short but somewhat arbitrary time interval (2 s (Martin & Kok, 2018) or 0.04 s (Comola, Kok, et al., 2019)) almost never stops. Interestingly, Comola, Kok, et al. (2019) showed that the value of f_Q can be indirectly estimated from the lowpass-filtered wind speed associated with large and very large scale turbulent structures (cutoff frequency $\Omega \approx 0.04$ Hz). Alternatively, for their coupled DNS/DEM simulations of fluvial bedload transport, González et al. (2017) fitted continuous functions to the distributions of the discrete transported particle number (defined as the number of particles faster than a somewhat arbitrary velocity threshold) at different τ and identified the onset of continuous transport as the value of τ at which these fitting functions predict a zero probability for a vanishing particle number. Future studies should investigate the compatibility of these and other definitions of continuous transport.

4.1.3.3. Controversy: Threshold of Continuous Aeolian Saltation Transport

In the opinion of the authors, the evidence reviewed above for the hypothesis that continuous transport occurs once impact entrainment alone is sufficient in compensating random captures of transported particles is quite strong. (In other words, significant fluid entrainment may occur in continuous transport—and does so quite likely in aeolian saltation transport given that the turbulent intensity within the saltation transport layer increases with the sediment transport rate (Li & McKenna Neuman, 2012)—but it is not needed to sustain continuous transport.) However, it is worth pointing out that most aeolian researchers prefer a different narrative for aeolian saltation transport. For example, Martin and Kok (2018) assumed that continuous aeolian saltation transport in the field occurs once the saltation transport initiation threshold ($\approx \tau_t^{\text{In}}$) is exceeded, whereas the impact entrainment threshold describes the cessation of intermittent saltation transport. This assumption is based on the idea that fluid entrainment continuously provides the transport layer

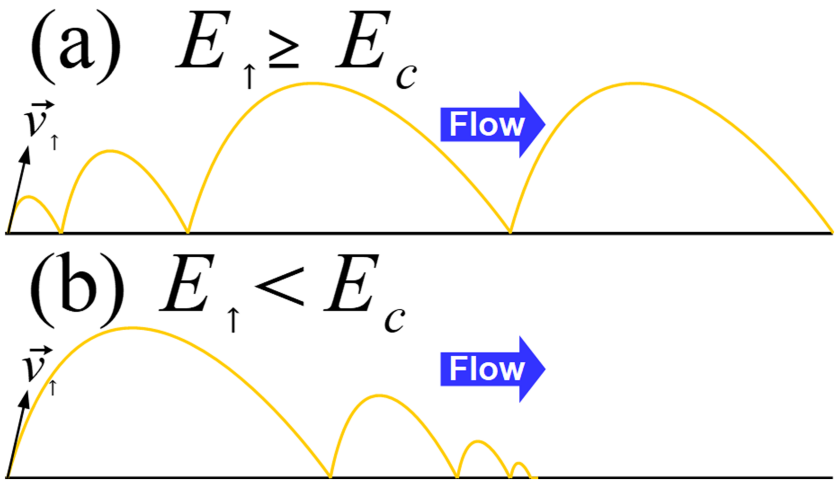

Figure 15. Sketch of continuous rebound mechanism. Depending on its initial kinetic energy $E_\uparrow$ relative to a critical energy level E_c that depends on the properties of the flow, a particle (yellow lines) either (a) gains sufficient energy in its hops along a flat wall (black lines) to approach a steady, periodic hopping motion or (b) net loses energy until it stops.

with bed particles. However, this idea is problematic because turbulent events capable of fluid entrainment occur only at an intermittent basis (see section 3). The interested reader is also referred to the commentary by Pähtz (2018), in which this controversy is extensively discussed.

4.2. Continuous Particle Rebounds and Transport Capacity

In order for the mean turbulent flow to sustain the motion of particles that are already in transport, it needs to compensate, on average, the energy dissipated in particle-bed rebounds via drag acceleration during the particle trajectories. This mechanism, which is illustrated in detail by means of a thought experiment in section 4.2.1, gives rise to a shear stress threshold of sediment transport (henceforth termed *rebound threshold*), as was already noted by Bagnold (1941, p. 94) for aeolian saltation transport: "Physically [the rebound threshold] marks the critical stage at which the energy supplied to the saltating grains by the wind begins to balance the energy losses due to friction when the grains strike the ground [and rebound]." It also suggests a clear-cut definition of transport capacity, which is otherwise difficult to define (see review by Wainwright et al., 2015, and references therein), that leads to an experimentally and numerically validated universal scaling of the transport load M (i.e., the mass of transported sediment per unit bed area) with the fluid shear stress τ (section 4.2.2). From the appearance of the rebound threshold in this scaling of M, one can conclude that at a significant if not predominant portion of the threshold measurements by Shields (1936) and others have been misidentified as measurements of the entrainment threshold (section 4.2.3).

4.2.1. Particle Rebounds Along a Flat Wall

To illustrate the concept of continuous particle rebounds, the motion of a particle along a flat wall driven by a constant flow (e.g., the mean turbulent flow) is considered. This particle shall never be captured and instead, for illustration purposes, always rebound with a constant angle and lose a constant fraction of its impact energy (the core of the argument will not significantly change if more sophisticated rebound laws, such as equations (20)–(22), are considered). For this idealized scenario, there are two possible particle trajectories depending on the initial particle velocity $\mathbf{v}_\uparrow$, which are sketched in Figure 15. First, if the corresponding initial kinetic energy $E_\uparrow$ exceeds a critical value E_c, the particle will spend sufficiently long within the flow so that it gains sufficient energy via fluid drag during its hops to approach a steady, periodic hopping motion, in which its energy gain via fluid drag is exactly balanced by its energy loss during its rebounds (Figure 15a). Henceforth, such particles are termed *continuous rebounders*. Second, if $E_\uparrow < E_c$, the particle loses net energy in its initial and all subsequent hops until it stops (Figure 15b). The critical energy E_c depends on properties of the flow. Crucially, if the flow is too weak, all possible trajectories fall into the second category (i.e., $E_c = \infty$).

There are a few takeaways from the this simple thought experiment for realistic systems. First, as the mean turbulent flow is controlled by the fluid shear stress τ, it suggests the existence of a rebound threshold τ_t^{Rb} below which the energy losses in particle-bed rebounds cannot be compensated by the flow on average

(Berzi et al., 2016, 2017; Jenkins & Valance, 2014; Pähtz & Durán, 2018a; Pähtz, Liu, et al., 2020). Second, the randomness introduced by inhomogeneities of the bed and turbulent fluctuations of the flow introduce trajectory fluctuations that can lead to random losses of continuous rebounders, particularly when the lift-off energy accidentally falls below E_c (Pähtz and Durán, 2018a). Such losses must be compensated by the entrainment of bed particles into the continuous rebound layer. Hence, the mere mobilization of bed particles is not sufficient because the lift-off energy of mobilized particles must also exceed E_c. In particular, for rebound threshold models (see section 4.3), it has been shown that E_c becomes equal to the average rebound energy of continuous rebounders in the limit $\tau \to \tau_t^{\mathrm{Rb}}$ (Pähtz, Liu, et al., 2020). This implies that the impact entrainment threshold τ_t^{ImE} must be strictly larger than τ_t^{Rb}, since the energy of an entrained particle is much smaller than the energy of the particle that caused its entrainment (i.e., a continuous rebounder) because of energy conservation. In particular, $\tau_t^{\mathrm{ImE}} > \tau_t^{\mathrm{Rb}}$ automatically explains the discontinuous jump of the sediment transport rate Q at τ_t^{ImE} that has been observed in the absence of fluid entrainment by turbulent fluctuation events (see section 4.1.3) because $Q(\tau_t^{\mathrm{ImE}})$ is controlled by the excess shear stress $\tau_t^{\mathrm{ImE}} - \tau_t^{\mathrm{Rb}} > 0$ in the absence of such events (see section 4.2.2).

4.2.2. Transport Capacity Interpretation Based on Continuous Rebounds

A third takeaway for realistic systems of the thought experiment described in section 4.2.1 involves the fact that, because of momentum transfer from flow to particles, the flow slows down with increasing transport load M. Hence, for a given $\tau > \tau_t^{\mathrm{Rb}}$, provided that there is an abundance of impact and/or fluid entrainment, the system tends to entrain bed material until the mean turbulent flow becomes so weak that it can barely sustain the average motion of continuous rebounders (Pähtz & Durán, 2018b). Any further slowdown of the flow would then spike the deposition rate, leading to a decrease of M and subsequent increase of the flow speed. That is, the system is at a dynamic equilibrium that may be interpreted as transport capacity.

Pähtz and Durán (2018b) analytically showed that this interpretation of transport capacity leads to the capacity scaling

$$M \simeq \mu_b^{-1}\tilde{g}^{-1}(\tau - \tau_t^{\mathrm{Rb}}), \tag{29}$$

where $\tilde{g} = (1 - 1/s)g$ is the buoyancy-reduced value of the gravitational constant g and $\mu_b = \tau_{pb}/P_b$ an approximately constant bed friction coefficient (i.e., the ratio between the particle shear stress τ_{pb} and normal-bed particle pressure $P_b \simeq M\tilde{g}$ evaluated at the bed surface). Note that the definitions of τ_{pb} and P_b (and thus μ_b), in contrast to the definitions of τ_p and P (and thus the yield stress ratio μ_s, see section 2.1), include contributions from stresses associated with the particle fluctuation motion in addition to contributions from intergranular contacts. The derivation of equation (29) by Pähtz and Durán (2018b) is based on two main steps: showing the approximate constancy of μ_b starting from a geometric constraint on particle-bed rebounds in the steady state and assuming $\tau_{gb} \simeq \tau - \tau_t^{\mathrm{Rb}}$, which expresses the aforementioned dynamic equilibrium condition associated with the continuous rebound motion. Interestingly, τ_{gb} describes the momentum that is transferred from flow to transported particles per unit bed area per unit time, which implies that high-buoyant fluids (small $\tilde{g}$), such as water, require a larger transport load M for a given rate of momentum transfer (i.e., for a given $M\tilde{g} \propto \tau_{gb}$) than low-buoyant fluids (large $\tilde{g}$), such as air. Pähtz and Durán (2018b) tested these derivation steps with numerical data from DEM-based simulations of nonsuspended sediment transport (the same as those by Pähtz and Durán, 2017, see section 4.1.3). It turned out that these steps, and thus equation (29), are obeyed across nonsuspended sediment transport conditions with $Ga\sqrt{s} \gtrsim 10$ (all but relatively viscous bedload transport) provided that the bed surface is defined as the effective elevation of energetic particle-bed rebounds.

The functional form of equation (29) is the foundation of the majority of theoretical and experimental shear stress threshold-based expressions for the capacity transport rate, $Q \simeq M\overline{v_x}$ (where $\overline{v_x}$ is the average streamwise velocity of particles moving above the bed surface), and goes back to the pioneering theoretical descriptions of nonsuspended sediment transport by Bagnold (1956, 1966, 1973). However, Bagnold's physical interpretation of the assumptions leading to this scaling was inaccurate: μ_b is not equal to μ_s and τ_t^{Rb} is not an entrainment threshold, as Bagnold assumed (Pähtz & Durán, 2018b). In fact, equation (29) has no association with sediment entrainment whatsoever, except for the fact that sediment entrainment is a necessary requirement to keep transport at capacity (Pähtz & Durán, 2018b).

As explained in section 4.1.3, Q, and thus M, is significantly larger than zero at the impact entrainment threshold τ_t^{ImE}. In particular, transport becomes intermittent for $\tau < \tau_t^{\mathrm{ImE}}$ or even stops in the absence of entrainment by turbulent fluctuation events (i.e., transport capacity cannot be sustained). Hence,

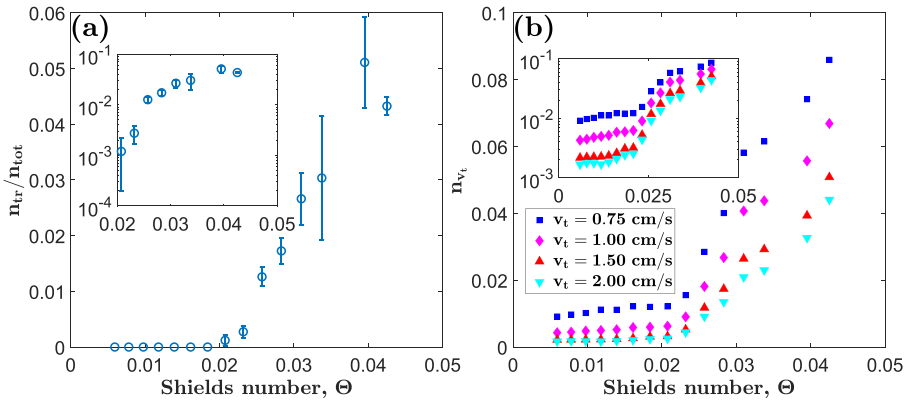

Figure 16. Measurements of particle activity by Salevan et al. (2017). (a) Number of transported particles relative to the total number of bed surface particles (n_{tr}/n_{tot}) and (b) number of particles n_{v_t} that are faster than a certain velocity threshold v_t versus Shields number Θ. Error bars in (a) correspond to the standard error computed from six experimental runs.

equation (29) is, in general, valid only for $\tau \geq \tau_t^{ImE}$ and also consistent with the rebound threshold model prediction $\tau_t^{ImE} > \tau_t^{Rb}$ (see section 4.2.1). Note that aeolian saltation transport experiments (Carneiro et al., 2015; Martin & Kok, 2018) and coupled DNS/DEM fluvial bedload transport simulation (González et al., 2017), indeed, very roughly suggest $\tau_t^{ImE} \approx 1.5\tau_t^{Rb}$ and $\tau_t^{ImE} \approx 2\tau_t^{Rb}$, respectively. In order to extend the validity of equation (29), and thus of standard sediment transport rate relationships, to shear stresses τ with $\tau_t^{Rb} < \tau < \tau_t^{ImE}$, one must abandon long-term averaging sediment transport data. Instead, it is necessary to conditionally average M (or Q) only over periods of near-capacity transport (on short-term average), but ignore periods with transport significantly below capacity or even at rest (Bunte & Abt, 2005; Comola, Kok, et al., 2019; Singh et al., 2009; Shih & Diplas, 2018). Likewise, for realistic fluvial bedload transport, it is necessary to exclude the turbulence-driven fluctuation motion (including turbulent entrainment events) when measuring M for equation (29) to remain valid; otherwise, transport does not vanish for $\tau \to \tau_t^{Rb}$. Salevan et al. (2017) demonstrated that implementing such constraints in the analysis of experimental data is, in principle, possible. By separating the velocity distribution of all measurable particles (including those that are visually perceived as resting) into a Student's t-distribution associated with the turbulence-driven fluctuation motion and an exponential distribution associated with the bulk transport of particles (which automatically implies conditional averaging as periods of rest do not affect this distribution), they obtained a measure for the number of transported particles relative to the total number of bed surface particles (n_{tr}/n_{tot}). This measure, indeed, vanishes within experimental precision below a Shields number threshold (Figure 16a), which can be interpreted as Θ_t^{Rb}, whereas the number of particles n_{v_t} that are faster than a certain velocity threshold v_t remains nonzero for the entire range of Θ because of the turbulence-driven fluctuation motion (Figure 16b).

4.2.3. Does the Shields Diagram Truly Show Incipient Motion Thresholds?

The Shields diagram is a compilation of measurements of the threshold Shields number Θ_t as a function of the shear Reynolds number Re_*, which have been labeled as measurements of incipient sediment motion by numerous studies and reviews (e.g., Shields, 1936, Ali & Dey, 2016; Buffington & Montgomery, 1997; Cao et al., 2006; Dey, 1999; Dey & Ali, 2019, 2018; Dey & Papanicolaou, 2008; Ling, 1995; Miller et al., 1977; Paphitis, 2001; Parker & Klingeman, 1982; van Rijn, 1984; Wiberg & Smith, 1987; Yalin & Karahan, 1979; Yang et al., 2019; and references therein). However, incipient motion of turbulent fluvial bedload transport is much better characterized by impulse and energy-based criteria (section 3.2), unless one refers to the Shields number Θ_t^{In} at which the fluid entrainment probability exceeds zero (section 3.3), which is much below the Shields curve (Paintal, 1971). Furthermore, in steady, homogenous turbulent fluvial bedload transport in which turbulence is suppressed (e.g., in narrow water flumes), the vast majority of entrainment events is caused by particle-bed impacts (see section 4.1.3). It is therefore here argued, based on the results reviewed in section 4.2.2, that many of the threshold data compiled in the Shields diagram are actually measurements of the rebound threshold Θ_t^{Rb}.

The Shields diagram shows two kinds of threshold measurements obtained using two different methods. The first method is the *reference method*, where one takes paired measurements of Θ and the nondimensionalized

transport rate Q_* (or transport load $M_* \equiv M/(\rho_p d)$) and extrapolates them to the Shields number at which Q_* (or M_*) either vanishes (e.g., Shields, 1936) (it is slightly controversial whether Shields really used this method (Buffington, 1999)) or equals a small reference value (e.g., Parker & Klingeman, 1982). This method yields approximately the rebound threshold Θ_t^{Rb} if an expression for Q_* (or M_*) based on equation (29) is used for the extrapolation and provided that the data used for the extrapolation are at capacity (i.e., $\Theta \geq \Theta_t^{\mathrm{ImE}}$). For example, Lajeunesse et al. (2010) extrapolated their measurements (many data points obeyed $\Theta \geq 2\Theta_t^{\mathrm{Rb}} \approx \Theta_t^{\mathrm{ImE}}$) to $M_* = 0$ using exactly equation (29), yielding exactly Θ_t^{Rb}. That the reference method yields the rebound threshold Θ_t^{Rb} is further supported by the fact that the values of Θ_t^{Rb} obtained from the DEM-based fluvial bedload transport simulations by Pähtz and Durán (2018a) are consistent with the compilation of reference method-based threshold measurements by Buffington and Montgomery (1997).

The second method is the *visual method*, where one increases Θ until criteria defining what is considered critical transport are obeyed (e.g., Kramer, 1935) (see section 1). The threshold values obtained from this method depend significantly on the chosen criterion and are, on average, close to those obtained from the reference method (Buffington and Montgomery, 1997). For example, the transition point $(\Theta, Q_*) \approx (0.05, 0.007)$ at which the function $Q_*(\Theta)$ measured in the gravel-bed experiments by Paintal (1971) changed from $Q_* \propto \Theta^{16}$ to $Q_* \propto \Theta^{2.5}$ (see section 1) is indistinguishable from the reference threshold for the same conditions within measurement uncertainty. In particular, a close examination of Paintal's and other gravel bed data has revealed that Paintal's power-16 region can actually be subdivided into two regions (Dey & Ali, 2019, Figure 5) (see also Shih and Diplas, 2019, Figure 8b): one region ($\Theta \lesssim 0.04$) with a milder power law and one with a stronger power law ($0.04 \lesssim \Theta \lesssim 0.05$), which includes a jump of Q_* by an order of magnitude at $\Theta \simeq 0.04$. Such a jump is consistent with exceeding the rebound threshold Θ_t^{Rb} because transported particles suddenly become able to move along the surface for comparably long times before being captured by the bed. Hence, it seems that also the visual method, at least for typical critical transport criteria, approximately yields the rebound threshold Θ_t^{Rb} rather than an entrainment threshold.

The hypothesis that the Shields diagram shows measurements of the rebound threshold is further supported by the fact that certain rebound threshold models (Pähtz & Durán, 2018a; Pähtz, Liu, et al., 2020) reproduce the Shields curve without fitting to the experimental data compiled in the Shields diagram (see section 4.3), even when limited to only visually measured data (Pähtz, Liu, et al., 2020).

4.3. Sediment Transport Cessation Models

This section reviews theoretical models for both the rebound threshold Θ_t^{Rb} and impact entrainment threshold Θ_t^{ImE}. One of the early motivations for developing such models was to better understand the hysteresis between the initiation and cessation of aeolian saltation transport observed in wind tunnel experiments (e.g., Bagnold, 1941; Carneiro et al., 2015; Chepil, 1945; Iversen & Rasmussen, 1994). While the difference between transport initiation and cessation is relatively small on Earth, wind tunnel experiments and observations suggested a substantial difference on Mars, which needed to be explained (Almeida et al., 2008; Kok, 2010b). (However, note that extrapolating wind tunnel measurements of the initiation threshold Θ_t^{In} to field conditions using standard initiation threshold models is actually inappropriate because Θ_t^{In} depends on the boundary layer thickness δ, as discussed in section 3.3.) Later on, cessation threshold models were developed with the purpose to unify fluvial bedload and aeolian saltation transport in a single theoretical framework (Berzi et al., 2016; Pähtz & Durán, 2018a; Pähtz, Liu, et al., 2020).

As cessation threshold models are associated with a sustained motion of transported particles, they require a physical description of the particle motion within the transport layer that is coupled with boundary conditions that describe the interaction between transported particles and the bed surface. In general, there have been two approaches to describe the transport layer and bed interactions. The first approach consists of representing the entire particle motion by particles moving in identical periodic trajectories along a flat wall that mimics the bed surface (section 4.3.1). The second approach consists of deriving general correlations between transport layer-averaged physical quantities and obtain the correlation coefficients from numerical simulations (section 4.3.2). It will be shown that the latter approach is probably a rough approximation of a variant of the former. Correlation-based model equations elucidate the role that the density ratio s plays for the rebound threshold Θ_t^{Rb} in a simple manner and therefore provide a simple conceptual explanation for why Θ_t^{Rb} is smaller in aeolian saltation than in fluvial bedload transport (section 4.3.3).

Most of the sediment transport cessation threshold models reviewed here account for cohesive interparticle forces and do so in a similar manner as transport initiation threshold models. However, Comola,

Gaume, et al. (2019) recently revealed that the effects of cohesion on transport cessation and initiation thresholds are actually fundamentally different from one another, which is why this section only considers versions of existing cessation threshold models for cohesionless particles. The effect of cohesion on the particle-bed collision process, and thus on transport cessation thresholds, remains a major open problem (see section 4.1.1.5).

4.3.1. Identical Periodic Trajectory Models (IPTMs)

Most studies proposing cessation threshold models start with the assumption that the motion of transported particles can be represented by a system in which all particles hop in the same periodic trajectory, referred to as the average trajectory, driven by the mean turbulent flow along a flat wall, with which they interact according to certain boundary conditions (Berzi et al., 2016, 2017; Claudin & Andreotti, 2006; Kok, 2010a; Pähtz, Liu, et al., 2020). (Note that, although Kok (2010a) does not explicitly refer to identical periodic trajectories, his mathematical treatment of the problem is equivalent to IPTMs.) However, the assumption of identical periodic particle trajectories introduces a variety of potentially major weaknesses, which has cast doubt on the reliability of IPTMs (Andreotti, 2004; Lämmel & Kroy, 2017; Pähtz & Durán, 2017, 2018a):

1. In IPTMs, the particle concentration increases with elevation z and jumps to zero when z exceeds the hop height (Anderson & Hallet, 1986). In contrast, in real nonsuspended sediment transport, it monotonously decreases with z, often exponentially (e.g., Durán et al., 2012). IPTMs that refer only to the motion of a well-defined species of particles (e.g., continuous rebounders) do not necessarily suffer from this weakness because the concentration profile associated with this species may behave differently from that of transported particles.
2. In IPTMs, the mean square of the vertical particle velocity ($\langle v_z^2 \rangle$) decreases with z. In contrast, in real nonsuspended sediment transport, it increases with z, except far from the bed surface (Pähtz & Durán, 2017). This behavior is a signature of the fact that the transport layer, in general, consists of different species of particles with different characteristic velocities (e.g., Durán et al., 2011, Figure 21). That is, IPTMs that refer only to the motion of a well-defined species of particles (e.g., continuous rebounders) do not necessarily suffer from this weakness.
3. Only particles that take off from the wall with an energy $E_\uparrow$ that is larger than a critical value E_c can continue their motion after the initial few hops (Figure 15). That is, IPTMs that take into account the motion of entrained particles (Claudin & Andreotti, 2006; Kok, 2010a) effectively assume that all entrained particles obey $E_\uparrow \geq E_c$ even though most of them do not (Pähtz & Durán, 2018a).
4. IPTMs neglect particle motion via rolling and sliding, which is significant in bedload transport.

Depending on the boundary conditions, three conceptually different kinds of IPTMs can be distinguished:

1. Models of the rebound threshold Θ_t^{Rb} consider only the dynamics of continuous rebounders. Their rebounds are described, for example, by equations (12b) and (13), which link the streamwise (x) and normal-wall (z) components of the impact velocity $\mathbf{v_i}$ to the streamwise and normal-wall components of the rebound velocity $\mathbf{v_r}$. Such models then look for the smallest Shields number that results in a periodic trajectory under the constraint that the hop height of particles exceeds one particle diameter ($z_h \geq d$). This constraint ensures consistency with the underlying model assumption that continuous rebounders are never captured by the bed surface. The threshold resulting from this constraint is denoted as $\Theta_t^{\mathrm{Rb}**}$. Pähtz, Liu, et al. (2020) modified this constraint to take into account that the near-surface flow can assist particles in escaping the bed surface and is even predominantly responsible for the escape in the viscous bedload transport regime. These authors' escape criterion reads $\Theta/\Theta_t^{\max} \geq \cot\psi / \cot\psi_Y$, where $\Theta_t^{\max} = 0.12$ is the viscous fluid entrainment threshold (see section 2.1), $\psi_Y = 30°$ the pocket angle for particles resting within the deepest pockets of the bed surface, and $\sin\psi = \sin\psi_Y + \mathbf{v_r}^2/(2\tilde{g}d)$. This criterion means that the rebound kinetic energy only needs to uplift a particle rebounding within the deepest pocket to a point at which the near-surface flow is able to push it out of the pocket. The threshold resulting from this modified constraint is denoted as $\Theta_t^{\mathrm{Rb}*}$.
2. Models of the impact entrainment threshold Θ_t^{ImE} (Claudin & Andreotti, 2006; Kok, 2010a) do not neglect captures of continuous rebounders and therefore take into account the entrainment of bed particles. One possible way to do this is by combining rebound boundary conditions with an additional constraint that describes that one particle leaves the surface per impact on average (e.g., $|\mathbf{v_i}| \propto \sqrt{\tilde{g}d}$ (Claudin & Andreotti, 2006)). However, the incorporation of entrained particles as part of the average trajectory leads to consistency problems (see third point in the list above).

Table 1
Modeling Details of the IPTMs by Claudin and Andreotti (2006) (CA06), Kok (2010a) (K10), Berzi et al. (2016, 2017) (B16/17), and Pähtz, Liu, et al. (2020) (P19)

Study	Model	Vertical drag	Viscous sublayer	Viscous damping	Boundary condition
CA06	Θ_t^{ImE}	yes	yes	no	$e^{2D}, \theta_r^{2D} = \mathrm{const}$
K10	Θ_t^{ImE}	yes	no	no	complex
B16/17	$\Theta_t^{\mathrm{Rb\|ImE}}$	no	no	yes	equations (12b) and (13)
P19	$\Theta_t^{\mathrm{Rb}*}$	yes	yes	no	equations (12b) and (14)

3. Hybrids between continuous rebound and impact entrainment models (Berzi et al., 2016, 2017) look for the smallest Shields number (denoted as $\Theta_t^{\mathrm{Rb|ImE}}$) that results in a periodic trajectory under the constraint $z_h \geq d$ (like before) and the additional constraint that particle-bed impacts do not lead to entrainment. Berzi et al. (2016, 2017) modeled the latter constraint via $|\mathbf{v_i}|/\sqrt{\tilde{g}d} \leq \zeta/2 \approx 20$ (cf. equation (17)), which assumes that the fastest particles represented by the average trajectory of continuous rebounders do not exceed the value ζ of the nondimensionalized impact velocity that is associated with the onset of entrainment (which can be roughly justified by assuming an even impact velocity distribution between 0 and ζ). However, Pähtz and Durán (2018a) pointed out that this additional constraint is inconsistent with the experimental and numerical evidence that impact entrainment to be effective requires that the transport rate is significantly larger than zero (see section 4.1.3), which is never the case at the rebound threshold Θ_t^{Rb} in the absence of entrainment by turbulent fluctuation events (see section 4.2.2 and equation (29)). Consistently, Pähtz, Liu, et al. (2020) showed that, in the limit $\Theta \to \Theta_t^{\mathrm{Rb}}$, identical periodic trajectories of continuous rebounders are unstable against trajectory fluctuations. That is, the energy that a particle must acquire upon entrainment to become a continuous rebounder is equal to the rebound energy of the continuous rebounder that has entrained it in this limit. This requirement contradicts the fact that the entrainment energy is much smaller than the rebound energy because of energy conservation, which implies that impact entrainment is impossible in this limit (see also discussion in section 4.2.1).

Apart from these conceptual differences, existing IPTMs differ in several details (partly summarized in Table 1): the form of the fluid drag law, the consideration or neglect of vertical drag forces on the particle motion, the form of the mean flow velocity profile (including the question of whether the viscous sublayer of the turbulent boundary layer is considered; for more details, see Appendix A), and the bed boundary conditions (including the incorporation of viscous damping in the rebound laws). In this regard, it is reiterated that the effects of viscous damping on the dynamics of particle-bed rebounds are probably negligible for bedload transport (for which viscous damping is deemed as potentially significant), even for conditions with strongly damped binary particle collisions (see section 4.1.1.4).

In order to facilitate a comparison between the different model types that does not depend on modeling details but focuses only on conceptual differences, the same mean flow velocity profile (equation (A1), which includes the viscous sublayer), boundary conditions (equations (20) and (21)), and fluid drag law (the drag law by Camenen (2007)) are used for all model types. Following the trajectory calculation by Pähtz, Liu, et al. (2020), the impact velocity $\mathbf{v_i}$ as a function of the rebound velocity $\mathbf{v_r}$ approximates as

$$\hat{v}_{iz} = \hat{v}_{rz} - \hat{t}_h, \quad \text{with} \quad \hat{t}_h = 1 + \hat{v}_{rz} + W\left[-\left(1+\hat{v}_{rz}\right)e^{-(1+\hat{v}_{rz})}\right], \tag{30a}$$

$$\hat{v}_{ix} = \hat{v}_{rx}e^{-\hat{t}_h} + V_s^{-1}\sqrt{\Theta}f(Ga\sqrt{\Theta}, V_s^2 s\hat{z}_* + Z_\Delta)(1 - e^{-\hat{t}_h}), \quad \text{with} \quad \hat{z}_* \equiv -\hat{v}_{iz}(\hat{v}_{rz}+1) - \hat{v}_{rz}, \tag{30b}$$

where t_h is the hop time, W the principal branch of the Lambert-W function, $V_s \equiv v_s/\sqrt{s\tilde{g}d}$ the dimensionless value of the settling velocity v_s (defined in equation (31)), $Z_\Delta d = 0.7d$ the average elevation of the particles' center during particle-bed rebounds (obtained from experiments (Dey et al., 2012; Hong et al., 2015)), and $\sqrt{\Theta}f$ expresses the nonfluctuating wall-bounded flow after Guo and Julien (2007), with f the function given in equation (A1). Furthermore, the hat denotes nondimensionalized quantities using combinations of $\tilde{g}$ and v_s, which is given by

$$v_s = \frac{\sqrt{s\tilde{g}d}}{\mu_b}\left[\sqrt{\frac{1}{4}\sqrt[m]{\left(\frac{24}{C_d^\infty Ga}\right)^2} + \sqrt[m]{\frac{4\mu_b}{3C_d^\infty}}} - \frac{1}{2}\sqrt[m]{\frac{24}{C_d^\infty Ga}}\right]^m, \quad \text{with} \quad \mu_b \equiv \frac{v_{ix} - v_{rx}}{v_{rz} - v_{iz}}, \tag{31}$$

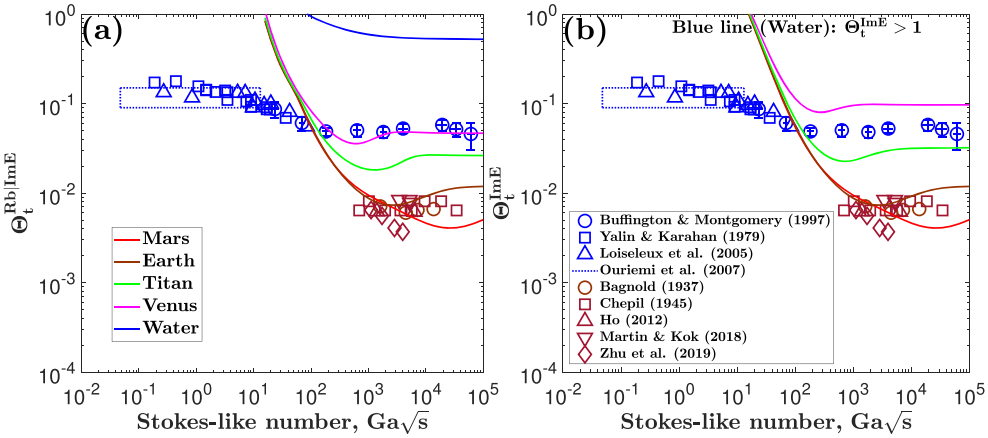

Figure 17. Predictions of (a) the hybrid between rebound and impact entrainment threshold ($\Theta_t^{Rb|ImE}$) and (b) the impact entrainment threshold Θ_t^{ImE} from the IPTM as functions of the Stokes-like number $Ga\sqrt{s}$ (lines) for five different density ratios $s = (2.65, 40, 190, 2200, \text{and } 250000)$ corresponding to five different fluvial or aeolian conditions (Water, Venus, Titan, Earth, and Mars). Symbols correspond to threshold measurements (or measurement compilations) from various studies (Bagnold, 1937; Chepil, 1945; Buffington & Montgomery, 1997; Ho, 2012; Loiseleux et al., 2005; Ouriemi et al., 2007; Martin & Kok, 2018; Zhu et al., 2019) and methods (see text). Ouriemi et al. (2007) did not report single measurement values but a constant threshold 0.12 ± 0.03 for a large range of viscous conditions, indicated by the dotted square. Error bars correspond to 95% confidence intervals of the compilation of reference method-based measurements by Buffington and Montgomery (1997), which make up a large portion of the Shields diagram.

where $C_d^\infty = 1$ and $m = 1.5$ are parameter values associated with the drag law for naturally shaped particles. Equations (20), (21), (30a), and (30b) can be iteratively solved for $\Theta(Ga, s, \hat{v}_{rz})$. Then the thresholds are obtained from

$$\Theta_t^{Rb*}(Ga,s) \equiv \min_{\hat{v}_{rz}} \Theta\left\{Ga,s,\hat{v}_{rz}\left[\cot^2\psi_Y \frac{\Theta^2}{\Theta_t^{\max 2}} \geq \left(\sin\psi_Y + \frac{\mathbf{v_r}^2}{2\tilde{g}d}\right)^{-2} - 1\right]\right\}, \tag{32a}$$

$$\Theta_t^{Rb**}(Ga,s) \equiv \min_{\hat{v}_{rz}} \Theta\left[Ga,s,\hat{v}_{rz}\left(z_h \geq d\right)\right], \tag{32b}$$

$$\Theta_t^{ImE}(Ga,s) \equiv \Theta\left[Ga,s,\hat{v}_{rz}\left(|\mathbf{v_i}| = \frac{1}{2}\zeta\sqrt{\tilde{g}d}\right)\right], \tag{32c}$$

$$\Theta_t^{Rb|ImE}(Ga,s) \equiv \min_{\hat{v}_{rz}} \Theta\left[Ga,s,\hat{v}_{rz}\left(z_h \geq d \wedge |\mathbf{v_i}| \leq \frac{1}{2}\zeta\sqrt{\tilde{g}d}\right)\right], \tag{32d}$$

where the hop height is given by $z_h = [v_{rz}v_s - v_s^2\ln(1+v_{rz}/v_s)]/\tilde{g}$ (for small v_{rz}/v_s, $z_h \simeq v_{rz}^2/(2\tilde{g})$). In equations (32a)–(32d), the rebound threshold Θ_t^{Rb*} is the only modeled cessation threshold that is linked to the viscous yield stress $\Theta_t^{\max}$ and thus to dense granular flow rheology (see section 2.1). In a complete model covering all transport regimes, such a connection must exist because $\Theta_t^{\max}$ represents an upper limit to any kind of cohesionless sediment transport threshold. Also, a complete model of any kind of cohesionless transport threshold must reach this maximum value in the limit of vanishing particle inertia (i.e., when typical particle velocities during a trajectory become much smaller than $\sqrt{\tilde{g}d}$). The characteristic particle velocity scale in IPTMs is given by the settling velocity v_s, which scales as $v_s \propto Ga\sqrt{s\tilde{g}d}$ in the viscous regime (equation (31) for small Ga). That is, a complete model of any kind of cohesionless transport threshold must approach $\Theta_t^{\max}$ in the limit $v_s/\sqrt{\tilde{g}d} \propto Ga\sqrt{s} \to 0$, where $Ga\sqrt{s}$ can be interpreted as a Stokes-like number (Berzi et al., 2016, 2017; Clark et al., 2017; Pähtz and Durán, 2018a).

Figures 17a, 17b, and 18a show the thresholds calculated by equations (32a)–(32d) as a function of $Ga\sqrt{s}$ for five different density ratios $s = (2.65, 40, 190, 2200, \text{and } 250000)$ corresponding to five different fluvial or aeolian conditions (Water, Venus, Titan, Earth, and Mars). These figures also show cessation threshold measurements obtained for nearly cohesionless conditions using different experimental methods. For turbulent

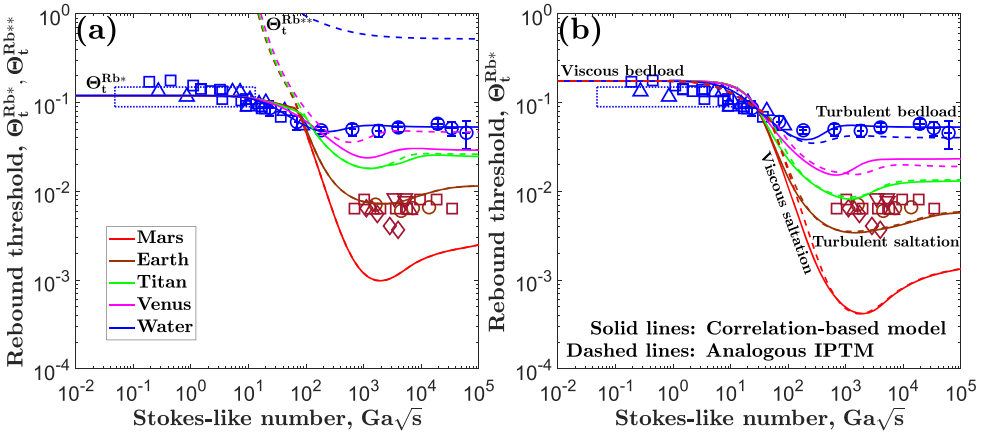

Figure 18. Predictions of the rebound threshold, Θ_t^{Rb**} (dashed lines in (a)) and Θ_t^{Rb*} (solid lines in (a) and (b) and dashed lines in (b)), from (a) the IPTM and (b) the correlation-based model by Pähtz and Durán (2018a) and its IPTM analog as a function of the Stokes-like number $Ga\sqrt{s}$ for five different density ratios s = (2.65, 40, 190, 2200, and 250000) corresponding to five different fluvial or aeolian conditions (Water, Venus, Titan, Earth, and Mars). Symbols correspond to threshold measurements (or measurement compilations) from various studies (Bagnold, 1937; Buffington & Montgomery, 1997; Chepil, 1945; Ho, 2012; Loiseleux et al., 2005; Martin & Kok, 2018; Ouriemi et al., 2007; Zhu et al., 2019) and methods (see text). Ouriemi et al. (2007) did not report single measurement values but a constant threshold 0.12 ± 0.03 for a large range of viscous conditions, indicated by the dotted square. Error bars correspond to 95% confidence intervals of the compilation of reference method-based measurements by Buffington and Montgomery (1997), which make up a large portion of the Shields diagram. For symbol legend, see Figure 17. The IPTM in (b) uses the modified boundary conditions $\mu_b = 0.63$ and $\cot\theta_r^{2D} = \mu_b[1/(\sqrt{3}c_1) - 1] \simeq 1.4$, and the modified viscous yield stress $\Theta_t^{max} = -\mu_b Z_\Delta/(2c_2) + \sqrt{[\mu_b Z_\Delta/(2c_2)]^2 + \mu_b^2/[18(1-c_3)c_2]} \simeq 0.175$ to mimic the predictions from the correlation-based model by Pähtz and Durán (2018a). These modifications are explained in the text.

bedload transport driven by water, the compilation of reference method-based measurements (measurement mean and its 95% confidence interval) by Buffington and Montgomery (1997), which make up a large portion of the Shields diagram, is shown. As explained in section 4.2.3, this method yields approximately the rebound threshold Θ_t^{Rb}. For viscous bedload transport driven by water-oil mixtures, the visual incipient motion measurements by Yalin and Karahan (1979) and Loiseleux et al. (2005) and cessation threshold measurements by Ouriemi et al. (2007) are shown (for viscous bedload transport, the differences between transport initiation, rebound, and impact entrainment threshold are very small (Pähtz and Durán, 2018a)). For aeolian saltation transport, a few studies (e.g., Ho, 2012; Zhu et al., 2019) carried out an indirect extrapolation to vanishing transport to obtain Θ_t^{Rb} using a proxy of Q: the surface roughness z_o (see Appendix A for its definition in the absence of transport), which undergoes a regime shift when saltation transport ceases. Furthermore, visual measurements of Θ_t^{Rb} by Bagnold (1937) and Chepil (1945) are shown, obtained from successively decrementing Θ until intermittent saltation transport stops. Direct measurements of the intermittent saltation transport threshold (and thus Θ_t^{Rb}), based on the so-called Time Frequency Equivalence Method (Wiggs et al., 2004), by Martin and Kok (2018) are also shown. Note that, although the evidence that the thresholds obtained from extrapolation to vanishing transport and from direct measurements of the cessation of intermittent saltation transport correspond to the rebound threshold Θ_t^{Rb} is quite strong (see sections 4.1.3 and 4.2.2), many aeolian researchers believe that they correspond to the impact entrainment threshold Θ_t^{ImE} (e.g., Martin and Kok, 2018). One of the reasons for this belief can be seen in Figure 17b: the prediction of Θ_t^{ImE} from equation (32c) is consistent with aeolian saltation transport data on Earth despite not containing fit parameters. In fact, for the range of conditions corresponding to these data, the predictions of Θ_t^{Rb*} and Θ_t^{Rb**} by equations (32a) and (32b) are equivalent and, coincidentally, very close to the predictions of Θ_t^{ImE} and $\Theta_t^{Rb|ImE}$ by equations (32c) and (32d), which are also equivalent to each other. At this point, it is worth reiterating that differences between the models caused by differences in the modeling details (e.g., those in Table 1) have been excluded here. Such detail differences cause the predictions of existing models to differ more strongly from one another than shown here.

Figures 17a, 17b, and 18a show that the predictions of Θ_t^{Rb**}, Θ_t^{ImE}, and $\Theta_t^{Rb|ImE}$ from equations (32b)–(32d) overestimate threshold measurements for fluvial bedload transport by at least an order of magnitude. For

Θ_t^{Rb**} and $\Theta_t^{Rb|ImE}$, this overestimation is caused by the constraint in the minimization of Θ that the particle hop height z_h must exceed one particle diameter d to escape the bed surface (equations (32b) and (32d)), preventing solutions with small particle velocities that would have a smaller threshold. However, the prediction of Θ_t^{Rb*} from equation (32a), which is based on a modified escape condition that takes into account the near-surface flow, is consistent with fluvial bedload transport conditions (Figure 18a). The simultaneous agreement of the prediction of Θ_t^{Rb*} from equation (32a) with aeolian and fluvial transport regimes strongly supports modeling nonsuspended sediment transport within the continuous rebound framework.

4.3.2. Models Based on Correlations Between Transport Layer-Averaged Physical Quantities

Existing correlation-based cessation threshold models start with the assumption of a constant bed friction coefficient μ_b (Pähtz et al., 2012; Pähtz & Durán, 2018a) (μ_b is the inverse of the parameter α in the model by Pähtz et al. (2012)). As discussed in section 4.2.2, the approximate constancy of μ_b has been analytically linked to continuous rebounds (Pähtz & Durán, 2018b). However, in contrast to the purely kinematic meaning of μ_b in IPTMs (equation (31)), for realistic nonsuspended sediment transport, μ_b conveys information about both the particle kinematics and interparticle contacts. Note that $\mu_b \simeq$ const is also predicted by IPTMs when vertical drag forces are small (i.e., the buoyancy-reduced gravity force dominates the vertical motion) because this fixes $e_z \simeq 1$ and thus e^{2D}, θ_r^{2D}, and μ_b via the rebound laws (Pähtz, Liu, et al., 2020).

A constant μ_b links the average horizontal fluid drag acceleration $\overline{a_{dx}}$ to the buoyancy-reduced gravity $\tilde{g}$ via $\mu_b \simeq \overline{a_{dx}}/\tilde{g}$, where the overbar denotes a particle concentration-weighted height average (Pähtz & Durán, 2018a) (which is equal to the average over the hop time for IPTMs). This link subsequently fixes the value of the nondimensionalized average velocity difference $U_x - V_x \equiv (\overline{u_x} - \overline{v_x})/\sqrt{s\tilde{g}d} = \mu_b v_s/\sqrt{s\tilde{g}d}$ (Pähtz, Liu, et al., 2020) as a function of the Galileo number Ga via equation (31). In fact, equation (31) is not limited to IPTMs but actually more general (Pähtz & Durán, 2018a). A further general correlation between U_x and the nondimensionalized transport layer thickness $Z \equiv \bar{z}/d$ can be obtained from approximating $\overline{u_x(z)} \simeq u_x(\bar{z})$ (Pähtz & Durán, 2018a). An analogous approximation is also involved in some IPTMs, namely, in the right-hand side of equation (30b), since $\bar{\tilde{z}} \simeq \hat{z}_* \simeq \hat{v}_{rz}^2/3$ in leading order in $\hat{v}_{rz}$ (i.e., when vertical drag forces are small). Up to this point, the two existing correlation-based models by Pähtz et al. (2012) and Pähtz and Durán (2018a) are equivalent. From now on, only the latter model is reviewed as it constitutes a substantial improvement of the former model in many regards. Pähtz and Durán (2018a) derived the further correlation $V_z \equiv \sqrt{\overline{v_z^2}/(s\tilde{g}d)} = c_1\mu_b^{-1}V_x$, where c_1 is a proportionality constant. This correlation with $c_1 = [\sqrt{3}(\cot\theta_r^{2D}/\mu_b + 1)]^{-1}$ is also predicted by IPTMs in the limit of small vertical drag forces. That is, up to here, the model by Pähtz and Durán (2018a) is effectively an IPTM that neglects vertical drag forces. The main differences between the model by Pähtz and Durán (2018a) and IPTMs lie in the latter two equations of the full set of model equations:

$$U_x - V_x = \left[\sqrt{\frac{1}{4}\sqrt[m]{\left(\frac{24}{C_d^\infty Ga}\right)^2} + \sqrt[m]{\frac{4\mu_b}{3C_d^\infty}}} - \frac{1}{2}\sqrt[m]{\frac{24}{C_d^\infty Ga}}\right]^m, \tag{33a}$$

$$U_x = \sqrt{\Theta_t^{Rb*}}\, f[Ga\sqrt{\Theta_t}, (Z + Z_\Delta)], \tag{33b}$$

$$V_z = c_1\mu_b^{-1}V_x, \tag{33c}$$

$$Z = c_2\mu_b^{-1}\Theta_t^{Rb*} + sV_z^2, \tag{33d}$$

$$V_x = \frac{2\sqrt{\Theta_t^{Rb*}}}{\kappa}\sqrt{1 - \exp\left[-\frac{1}{4}c_3^2\kappa^{-2}\left(U_x/\sqrt{\Theta_t^{Rb*}}\right)^2\right]}, \tag{33e}$$

where $\mu_b = 0.63$, $c_1 = 0.18$, $c_2 = 0.9$, $c_3 = 0.79$, and $Z_\Delta = 0.7$ are the model parameter values that Pähtz and Durán (2018a) obtained from adjusting equations (33a)–(33e) to DEM-based simulations of nonsuspended sediment transport (the same kind of simulations as those by Pähtz and Durán (2017), see section 4.1.3). Equation (33d) contains two terms: a term (sV_z^2) that is associated with the vertical motion of particles (equivalent to $\bar{\tilde{z}} = \overline{\hat{v}_z^2}$ in IPTMs) and a term ($\mu_b^{-1}\Theta_t^{Rb*}$) that is associated with particle collisions and

particle-bed contacts of particles moving above the bed surface level, which occur because of the surface texture (Pähtz & Durán, 2018a). A term analogous to the latter does not appear in existing IPTMs. Equation (33e) empirically merges two extremes. On the one hand, when the transport layer is completely submerged within the viscous sublayer of the turbulent boundary layer (small $U_x/\sqrt{\Theta_t^{\mathrm{Rb}*}}$), it predicts $V_x = c_3 U_x$. For viscous bedload transport (i.e., when the transport layer is small: $Z \ll Z_\Delta$), this correlation with $c_3 = 1 - \mu_b/[18\Theta_t^{\max}(c_2\Theta_t^{\max}/\mu_b + Z_\Delta)]$ is also predicted by IPTMs that employ the constrained minimization principle in equation (32a) to calculate the rebound threshold $\Theta_t^{\mathrm{Rb}*}$. For viscous saltation transport (i.e., when the transport layer is large: $Z \gg Z_\Delta$), IPTMs of the rebound threshold that consider vertical drag forces also predict $V_x \propto U_x$ (Pähtz and Durán, 2018a). However, the proportionality constant exhibits a different value (but still near unity) that depends on $\mu_b/\cot\theta_r^{2D}$. On the other hand, when most transport occurs within the log-layer of the turbulent boundary layer (large $U_x/\sqrt{\Theta_t^{\mathrm{Rb}*}}$), equation (33e) predicts $V_x \simeq 2\sqrt{\Theta_t^{\mathrm{Rb}*}}/\kappa$, which also follows from the minimization principle for turbulent saltation transport (i.e., $Z \gg Z_\Delta$) (Pähtz & Durán, 2018a). For these reasons, equation (33e) can be interpreted as a rough approximation of the constrained minimization in equation (32a) yielding $\Theta_t^{\mathrm{Rb}*}$. In fact, Figure 18b shows that the predictions of $\Theta_t^{\mathrm{Rb}*}$ from the model by Pähtz and Durán (2018a) are similar to those from an analogous IPTM and that they are also consistent with measurements across aeolian and fluvial environments. The predictions from these two models differ for turbulent bedload transport (large $U_x/\sqrt{\Theta_t^{\mathrm{Rb}*}}$ and small transport layer: $Z \sim Z_\Delta$), mainly because the scaling $V_x \simeq 2\sqrt{\Theta_t^{\mathrm{Rb}*}}/\kappa$ that equation (33e) predicts for large $U_x/\sqrt{\Theta_t^{\mathrm{Rb}*}}$ does not capture the outcome of the constrained minimization in equation (32a) for $Z \sim Z_\Delta$. The predictions from these two models also differ for viscous saltation transport because the model by Pähtz and Durán (2018a) neglects vertical drag forces at various instances. However, note that this model does not completely neglect vertical drag forces because the scaling $V_x \propto U_x$ that equation (33e) predicts for viscous saltation transport is associated with vertical drag (Pähtz & Durán, 2018a), which is why deviations between this model and the analogous IPTM are only moderate in this regime.

4.3.2.1. Open Problem: Reliable Models of the Impact Entrainment Threshold and Planetary Saltation Transport

Existing models of the impact entrainment threshold (Claudin & Andreotti, 2006; Kok, 2010a; Pähtz et al., 2012), which is arguably also the continuous transport threshold, do not take into account that the transport rate Q is significantly larger than zero at Θ_t^{ImE}, even in the absence of entrainment by turbulent fluctuation events (see section 4.1.3). Instead, Q vanishes at the rebound threshold Θ_t^{Rb}, which is smaller than Θ_t^{ImE} (see section 4.2.2). Likewise, as mentioned before, existing models of Θ_t^{ImE} effectively assume that all entrained particles exhibit a kinetic energy that allows them to participate in the continuous rebound motion even though most of them do not (Pähtz & Durán, 2018a). For these reasons, existing impact entrainment threshold models seem to be missing important physics and need to be improved. This is problematic for modeling and predicting extraterrestrial sediment transport and associated bedform evolution (e.g., Almeida et al., 2008; Ayoub et al., 2014; Bourke et al., 2010; Durán Vinent et al., 2019; Jia et al., 2017; Kok, 2010b; Lorenz, 2014; Rasmussen et al., 2015; Telfer et al., 2018) because most predictions of the aeolian saltation transport rate require that transport is continuous (i.e., at capacity).

4.3.3. Main Difference Between Aeolian and Fluvial Rebound Threshold

The most important difference between aeolian saltation and fluvial bedload transport is the largely different density ratio s, which ranges from close to unity for oil and water to the order of 10^5 for air on Mars. Equations (33a)–(33e) elucidate that s affects the modeled rebound threshold $\Theta_t^{\mathrm{Rb}*}$ in a relatively simple manner. In fact, it can be seen that s explicitly appears only in equation (33d), which describes a monotonous increase of the dimensionless transport layer thickness Z with s. Subsequently, Z monotonously increases the dimensionless transport layer-averaged flow velocity U_x via equation (33b). That is, given a certain solution $\Theta_t^{\mathrm{Rb}*}(Ga, s)$ of equations (33a)–(33e), an increase of s leads to an increase of U_x, which must be compensated by a decrease of U_x via a decrease of $\Theta_t^{\mathrm{Rb}*}$ to achieve a new steady solution for the same Galileo number Ga. This mathematical fact expresses the physical fact that particles that stay longer in the flow can feel a given effective flow forcing at a lower fluid shear stress, which is the ultimate reason for why $\Theta_t^{\mathrm{Rb}*}$ decreases with s for a given Ga.

5. Summary and Outlook

Section 1 outlined five old, yet very significant, inconsistencies related to the concept of a threshold shear stress for incipient motion. For the concept of a threshold shear stress to be physically meaningful, these inconsistencies must be addressed and resolved. They can be briefly summarized as follows:

1. By design, existing models of incipient motion capture the conditions to which they have been adjusted (aeolian or fluvial transport on Earth). However, the predictions from standard models adjusted to aeolian transport on Earth (Iversen & White, 1982; Shao & Lu, 2000) are in stark disagreement with recent observations of aeolian transport on Mars (e.g., Baker et al., 2018; Sullivan & Kok, 2017).
2. Because of turbulent fluctuation events, fluid entrainment gives rise to fluvial bedload transport even for Shields numbers much below the Shields curve (Paintal, 1971), which is the curve that is thought to describe incipient motion.
3. Below the respective shear stress threshold associated with incipient motion, turbulent fluctuation events are able to initiate fluvial bedload transport but not aeolian saltation transport. However, there is no reason to believe that the physics of incipient motion are different in aeolian and fluvial environments.
4. Old experiments indicate a nonnegligible role of particle inertia in fluvial bedload transport (Graf & Pazis, 1977; Ward, 1969), which is problematic because critical conditions are defined via nonzero transport rates (i.e., particles are in motion at threshold conditions).
5. In old numerical simulations of turbulent fluvial bedload transport (Nino & Garcia, 1998), it was recognized that the threshold shear stress obtained from extrapolating the simulated capacity transport rate to vanishing transport may not be associated with fluid entrainment. This is problematic because many of the threshold data compiled in the Shields diagram have been obtained from such or similar extrapolation methods (e.g., Shields, 1936).

As a result of the latest research reviewed in sections 2–4, a new conceptual picture has emerged (section 5.1) that resolves these problems. However, it must be emphasized that this conceptual picture represents the authors' synthesis of the current state of the art, and many aeolian and fluvial geomorphologists may disagree. This is because, in some places, it stands in stark contrast to what has been a century old consensus. Likewise, there are still many open problems and controversies, summarized in section 5.2 (and highlighted in sections 2–4), as well as a number of issues that have not been discussed in this review (e.g., the effects of particle size heterogeneity on transport thresholds and sediment entrainment), into which section 5.3 presents a brief outlook.

5.1. A New and Controversial Conceptual Picture of the Physics of the Thresholds of Nonsuspended Sediment Transport and Bed Sediment Entrainment

Figure 19 summarizes the various shear stress thresholds of nonsuspended sediment transport and their relations to and effects on the transport characteristics. Details, with references to the research reviewed in sections 2–4, are described below.

5.1.1. Creeping ($\Theta > 0$)

Creeping (see section 2.3) refers to a superslow granular motion, usually in the form of intermittent local particle rearrangements within the sediment bed (not limited to the bed surface), that occurs below a macroscopic yield criterion (see section 2.1). One form of creeping is triggered by nearby regions above yield, while another form (the origin of which is not fully understood) occurs even in the absence of such regions. The existence of the latter form implies that sediment likely is *always* transported (albeit slowly) for arbitrarily small values of the Shields number Θ, even in the absence of turbulence. Creeping of both kinds is very important in determining the particle motion near transport initiation. It is fundamentally related to the granular material, not a purely fluid-driven effect.

5.1.2. Viscous Yield Stress Θ_t^{max}

Apart from creeping, which affects the entire granular bed, bed surface particles can be entrained directly by flow forces. When a sediment bed is subjected to a laminar flow at a sufficiently low shear Reynolds number Re_*, there is a critical Shields number, the yield stress Θ_t^{max}, above which motion of bed surface particles is initiated and then never stops, whereas potential transient motion below Θ_t^{max} will inevitably come to an end (see section 2.1). The viscous yield stress Θ_t^{max} constitutes the upper limit for any kind of cohesionless sediment transport threshold, including the Shields curve. The values of Θ_t^{max} reported in the literature are somewhat scattered (between 0.1 and 0.4), but these numbers are within the range of the bulk friction coefficients for granular materials (ranging from low friction spheres to more frictional, rough particles),

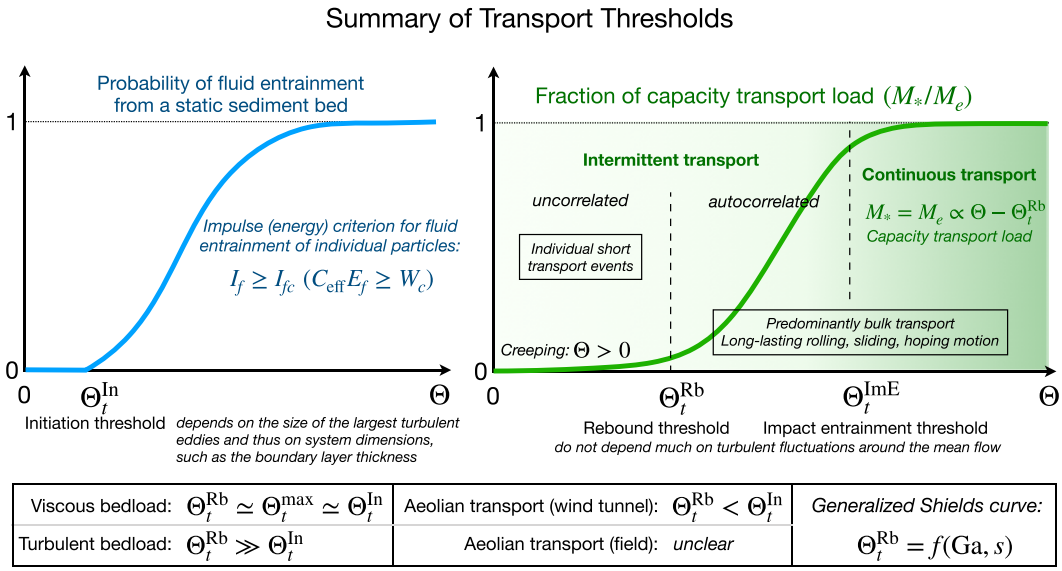

Figure 19. Sketch summarizing Shields number (Θ) thresholds of nonsuspended sediment transport.

suggesting that the granular material's yield condition (see section 2.1) is very important in determining the viscous yield stress.

5.1.3. Initiation Threshold Θ_t^{In}

While for laminar flows, the entrainment of individual bed surface particles is controlled by a critical Shields number, the entrainment of individual bed surface particles by turbulent flows is better described by an impulse (section 3.2.1) or energy (section 3.2.2) criterion. Nonetheless, one can still define an initiation threshold Shields number Θ_t^{In} (see section 3.3) at which the probability of fluid entrainment exceeds zero (i.e., $\Theta_t^{In} \simeq \Theta_t^{max}$ for laminar flows at sufficiently low Re_*). Because fluid entrainment is predominantly caused by turbulent fluctuation events, Θ_t^{In} depends not only on Re_* but also on properties that control the size of the largest turbulent flow eddies, such as the turbulent boundary layer thickness. This may be one of the reasons why aeolian incipient motion models adjusted to wind tunnel measurements fail when applied to atmospheric boundary layers (see first problem outlined at the beginning of section 5). Further possible reasons include atmospheric instability, topography gradients, surface inhomogeneities, such as obstacles and vegetation, and sublimation of subsurface ice in natural atmospheres (see section 3.3.3.4).

5.1.4. Rebound Threshold Θ_t^{Rb} (Generalized Shields Curve)

The rebound threshold Θ_t^{Rb} (see section 4.2) is largely unrelated to the entrainment of bed sediment (except for viscous bedload transport, for which $\Theta_t^{Rb} \simeq \Theta_t^{max}$) but describes the minimal dimensionless fluid shear stress that is needed for the mean turbulent flow to compensate the average energy loss of rebounding particles by fluid drag acceleration during their trajectories. Hence, for $\Theta \geq \Theta_t^{Rb}$, transported particles rebound for comparably longer periods before they deposit, whereas they deposit very quickly for $\Theta < \Theta_t^{Rb}$. The former transport regime gives rise to transport autocorrelations, while the latter gives rise to individual uncorrelated transport events. Hence, bulk sediment transport vanishes at Θ_t^{Rb}, which is described by a general law for the dimensionless bulk transport load M_* at transport capacity (i.e., $M_* = M_e \propto \Theta - \Theta_t^{Rb}$, see equation (29)). In fact, fluvial incipient motion measurements compiled in the Shields diagram are actually measurements of Θ_t^{Rb} (see section 4.2.3), consistent with the fact that turbulent fluvial bedload transport does not vanish even much below the Shields curve because of occasional strong turbulent fluctuation events (Paintal, 1971). The notion that Θ_t^{Rb} is largely unrelated to incipient motion and instead related to particle inertia resolves the second, third, fourth, and fifth problems outlined at the beginning of section 5. There are relatively simple models (which neglect turbulent fluctuations around the mean turbulent flow) predicting Θ_t^{Rb} in agreement with measurements across aeolian and fluvial environment without containing fitting parameters (models of Θ_t^{Rb*} in section 4.3). Such models predict a generalized Shields curve of the form $\Theta_t^{Rb}(Ga, s)$, where $Ga \equiv \sqrt{(s-1)gd^3}/\nu_f$ is the Galileo number and $s \equiv \rho_p/\rho_f$ the particle-fluid-density ratio, via modeling steady continuous particle trajectories. In fact, in aeolian environments, comparably large values of s allow the flow to sustain comparably large steady trajectories at a comparably low Shields number Θ, causing Θ_t^{Rb} to be substantially smaller than in fluvial environments for a given Ga (see section 4.3.3).

5.1.5. Impact Entrainment Threshold Θ_t^{ImE}

Even for $\Theta > \Theta_t^{Rb}$, randomness introduced by inhomogeneities of the bed and turbulent fluctuations of the flow introduce trajectory fluctuations that can lead to random captures of rebounding particles by the bed. To sustain transport capacity, these captures must be compensated by entrainment of bed sediment into the rebound layer by the action of the fluid (see section 3), by particle-bed impacts (see section 4.1.3), or a combination of both (see section 4.1.2). Because entrainment involving the flow requires strong turbulent fluctuation events (see sections 3 and 4.1.2), which occur only at an intermittent basis, transport remains intermittent when impact entrainment alone is insufficient in providing the transport layer with rebounders (i.e., for $\Theta < \Theta_t^{ImE}$). However, once the impact entrainment threshold Θ_t^{ImE} (see section 4.1.3) is exceeded ($\Theta \geq \Theta_t^{ImE}$), impact entrainment is sufficient to sustain continuous capacity transport, even without the assistance of fluid entrainment (i.e., significant fluid entrainment may occur, but is not needed). The impact entrainment threshold is strictly larger than the rebound threshold ($\Theta_t^{ImE} > \Theta_t^{Rb}$), which is associated with a nonzero bulk transport rate ($Q(\Theta_t^{ImE}) > 0$). This behavior can be explained within the continuous rebound framework (see section 4.2.1). Nonetheless, reliable models of Θ_t^{ImE} are currently missing (see section 4.3).

5.1.6. Differences Between Bedload and Saltation Transport

To avoid confusion, we reiterate that the terms *bedload transport* ($h \sim d$) and *saltation transport* ($h \gg d$) have been defined through the transport layer thickness h relative to the particle diameter d (see Notation section and section 1). Depending on the relationship between the initiation threshold Θ_t^{In} and the rebound threshold Θ_t^{Rb}, one observes different dynamics. For turbulent fluvial bedload transport, $\Theta_t^{In} \ll \Theta_t^{Rb}$, which means that transport can be initiated much below the Shields curve by occasional turbulent fluctuation events. However, whenever this happens, transport will very rapidly stop again. This is, indeed, the typical situation for gravel-bed rivers, which adjust their shape so that they remain in a low-mobility state (Parker, 1978; Phillips & Jerolmack, 2016). For aeolian transport in wind tunnels, Θ_t^{In} is significantly larger than Θ_t^{Rb}. This explains why aeolian bedload transport is usually very short-lived. In fact, even though bed particles are usually entrained into a rolling motion at Θ_t^{In} (i.e., $h \sim d$), this rolling motion rapidly evolves into saltation transport (Bagnold, 1941; Burr et al., 2015; Iversen et al., 1987) as the flow is sufficiently strong to net accelerate particles moving near the surface. By doing so, their hop height becomes larger and larger (i.e., h/d substantially increases) until a steady state is approached. For aeolian transport in the field, the magnitude of Θ_t^{In} relative to Θ_t^{Rb} is unclear as Θ_t^{In} is smaller than in wind tunnels because of a much larger boundary layer thickness δ, since δ controls the size of the largest turbulent eddies and thus entrainment by turbulent fluctuation events (see section 3.3).

5.1.7. Implications for Field Phenomenona

The new conceptual picture described above has been derived nearly entirely from theoretical and laboratory investigations. One may therefore wonder to what degree does the notion of various transport thresholds have implications for natural field conditions, such as bedload transport in rivers and saltation transport driven by planetary winds. There are three major aspects in which the field differs from most laboratory experiments: much broader particle size distributions, much larger and more unstable boundary layers (mainly for aeolian transport), and various kinds of surface inhomogeneities, such as bedforms, obstacles, and vegetation. The effects of particle size heterogeneity have been excluded from this review (they are briefly discussed in the outlook, section 5.3.1). The remaining two aspects are both associated with increasing turbulence and thus fluid entrainment (see section 3). In contrast, the rebound threshold Θ_t^{Rb} and arguably the impact entrainment threshold Θ_t^{ImE}, as well as the transport capacity scaling (which requires $\Theta \geq \Theta_t^{ImE}$), are mainly controlled by the mean turbulent flow and relatively insensitive to turbulent fluctuations around it and should therefore be similar in laboratory and field (provided that the bed particle size distributions are similar). That is, for $\Theta \geq \Theta_t^{ImE} \approx (1.5-2)\Theta_t^{Rb}$ (typical for river floods and many aeolian processes), one expects capacity relationships derived from laboratory experiments to reasonably work and laboratory and field to behave similar. This expectation is consistent with observations reported in recent studies (Martin & Kok, 2017; Recking, 2010; Recking et al., 2012). Even if transport is not at capacity, it is, in principle, possible to separate the turbulence-induced random transport contribution from sediment transport rate data sets (Salevan et al., 2017) (see section 4.2.2) and to modify capacity relationships to account for noncapacity transport (Comola, Kok, et al., 2019).

5.2. Summary of Important Open Problems and Controversies

Sections 2–4 have highlighted several important open questions and controversies that need to be addressed in future studies, which are summarized below.

Section 2:

1. Why do fluid-sheared surfaces creep below a macroscopic yield criterion? And why do they do so even for seemingly arbitrarily small values of the Shields number Θ and in the absence of turbulence?
2. What is responsible for the large spread of experimentally measured values of the viscous yield stress $\Theta_t^{\max}$?
3. Is flow-induced bed failure (i.e., yielding) a critical phenomenon?
4. What is the rheology of nonsuspended sediment transport?

Section 3 (although this section concerns both fluvial and aeolian transport conditions, open questions and controversies in this section regard mainly aeolian transport):

1. Why do different experimental designs for measuring the initiation threshold Θ_t^{In} of aeolian rolling and saltation transport cause qualitative differences in the scaling of Θ_t^{In} with the particle diameter d?
2. Is the measured dependency of Θ_t^{In} on the density ratio s for constant Galileo number Ga real or an artifact of differences in the boundary layer thickness of the wind tunnels used to carry out the experiments?
3. Is the measured strong increase of Θ_t^{In} with d for very large s in a wind tunnel with Martian pressure conditions real or an artifact of a limited boundary layer thickness of this wind tunnel?
4. Is aeolian transport in the field on Earth and other planetary bodies, in contrast to wind tunnels with similar atmospheric pressure conditions, always being initiated close to the rebound threshold Θ_t^{Rb} because of thick boundary layers, atmospheric instability, topography inhomogeneities, and subsurface ice sublimation? The answer to this question is probably the most important one, since a positive answer would imply that a reliable model for Θ_t^{In} (i.e., answers to the previous three questions) is not required for predicting aeolian processes on such bodies.
5. Does equilibrium aeolian bedload transport (i.e., $h \sim d$) exist in the field because of thick boundary layers?
6. Direct measurements of aeolian sediment transport initiation in the field, which are currently missing, can help answering the questions above.

Section 4:

1. For a particle collision with a static sediment bed: how does the rebound probability P_r depend on impact velocity and angle?
2. How do particle shape and size distribution affect particle-bed collisions?
3. Does viscous damping truly not much affect particle-bed collisions, as suggested by the insensitivity of DEM-based sediment transport simulations to the normal restitution coefficient ϵ of binary collisions? And if so, what is the physical reason?
4. How do cohesive interparticle forces affect the collision process and thus sediment transport cessation?
5. How do the laws describing a particle collision with a static bed change for a particle collision with a mobile bed?
6. It is straightforward to define intermittent and continuous sediment transport for the absence of fluid entrainment because the sediment transport rate exhibits a discontinuous jump from nearly zero to a finite value at the continuous transport threshold. However, how does one universally define intermittent and continuous transport if fluid entrainment does occur?
7. Is the transition from intermittent to continuous aeolian saltation transport associated with fluid entrainment (the current consensus) or with impact entrainment (the authors' opinion, based on recent developments in the field)?
8. What controls the impact entrainment threshold Θ_t^{ImE} and how does one model it?

5.3. Outlook

To limit the scope of this review, several important topics have been excluded. Two of them are briefly discussed below.

5.3.1. Effects of Particle Size Heterogeneity on Sediment Transport Initiation, Cessation, and Entrainment

Perhaps the most important topic that has been excluded from this review is the effects of the heterogeneity of the size of bed surface particles on sediment transport initiation, cessation, and entrainment. Naturally, sediment transport initiation and entrainment are size-selective. However, it is unclear whether this is also true for sediment transport cessation. While the continuous rebound mechanism (see section 4.2) is clearly a size-selective process (coarser particles are less accelerated during their trajectories), impact entrainment may not be (Martin & Kok, 2019; Zhu et al., 2019). Furthermore, in heterogeneous sediment beds, relatively

fine particles tend to be surrounded by coarser ones and their protrusion (i.e., the particle height above surrounding sediment) is thus smaller than on average, whereas relatively coarse particles tend to have a larger-than-average protrusion. Because driving forces decrease and resisting forces increase with decreasing protrusion (Yager et al., 2018), relatively fine particles are more difficult to be entrained when compared with a bed made only of such fine particles. The ability of fine particles to continuously rebound is also suppressed by the presence of coarse particles (Zhu et al., 2019). All these effects can make heterogeneous sediment beds much less mobile than homogeneous ones of the same median particle size. For example, for both fluvial bedload (MacKenzie & Eaton, 2017; MacKenzie et al., 2018) and aeolian saltation transport (Zhu et al., 2019), it was found for certain heterogeneous beds that the largest particles of the particle size distribution (larger than the 90th percentile) have a very strong control on overall mobility. However, the manner and degree of the heterogeneousness seem to play an important role as not all kinds of heterogeneous beds are so strongly affected by the presence of large particles (e.g., Martin & Kok, 2019; Wilcock, 1993). In particular, in the early stages of bed armoring, the sediment transport rate can increase because collisions between transported fine particles and coarse bed particles are more elastic than collisions between particles of the same size (Bagnold, 1973).

5.3.2. Effects of Steep Bed Slope on Sediment Transport Initiation, Cessation, and Entrainment

Another important topic that has been excluded from this review is the effects of steep bed slope angles on sediment transport initiation, cessation, and entrainment. For example, horizontal downslopes should, if everything else stays the same, increase bed mobility because of the additional horizontal gravity force acting on particles (Maurin et al., 2018). However, in fluvial environments, steep slopes are usually accompanied by a very small water depth of the order of one particle diameter (or even lower), which strongly suppresses the magnitude of hydrodynamic forces acting on particles, thus decreasing rather than increasing bed mobility (Prancevic & Lamb, 2015). Then again, an increasing downslope angle α increases the bulk friction coefficient μ within the sediment bed (for turbulent flows, $\mu \simeq \tan\alpha[1+[(\rho_p/\rho_f-1)\phi_b]^{-1}]$ (Maurin et al., 2018), where ϕ_b is the bed volume fraction). Once μ exceeds the static friction coefficient μ_s associated with the yielding transition (see section 2.1), the entire bed fails and a debris flow forms (Cheng et al., 2018; Prancevic et al., 2014; Takahashi, 1978).

Appendix A: Mean Flow Velocity Profile (Law of the Wall)

The mean flow velocity profile within the inner turbulent boundary layer above a flat wall (the *law of the wall*) exhibits three regions: a log-layer for large nondimensionalized elevations (*wall units*) $Re_* z/d$, a viscous sublayer for small $Re_* z/d$, and a buffer layer for transitional $Re_* z/d$. For more details on turbulent wall-bounded flows, see the review by Smits et al. (2011). In section 4.3, the following form of the law of the wall is used (Guo & Julien, 2007):

$$\begin{aligned}\frac{u_x}{\sqrt{(s-1)gd}} &= \sqrt{\Theta} f\left(Re_*, z/d\right),\\ f\left(Re_*, z/d\right) &= 7\arctan\left(\frac{Re_*}{7}\frac{z}{d}\right) + \frac{7}{3}\arctan^3\left(\frac{Re_*}{7}\frac{z}{d}\right)\\ &\quad - 0.52\arctan^4\left(\frac{Re_*}{7}\frac{z}{d}\right) + \ln\left[1+\left(\frac{Re_*}{B}\frac{z}{d}\right)^{(1/\kappa)}\right]\\ &\quad - \frac{1}{\kappa}\ln\left\{1+0.3Re_*\left[1-\exp\left(-\frac{Re_*}{26}\right)\right]\right\},\end{aligned} \tag{A1}$$

where $\kappa = 0.4$ and $B = \exp(16.873\kappa - \ln 9)$. Within the viscous sublayer of the turbulent boundary layer, $u_x/\sqrt{(s-1)gd} \rightarrow \Theta \mathrm{Ga} z/d$, whereas in the log-layer, $u_x/\sqrt{(s-1)gd} \rightarrow \kappa^{-1}\sqrt{\Theta}\ln(z/z_o)$. The roughness length z_o equals $d/(9 \quad Re_*)$ in the hydraulically smooth and $d/30$ in the hydraulically rough regime (Guo & Julien, 2007).

Notation

τ	Fluid shear stress [Pa]
τ_p	Particle shear stress [Pa]
P	Particle pressure [Pa]

ρ_p	Particle density [kg/m^3]
ρ_f	Fluid density [kg/m^3]
m_p	Particle mass [kg]
u	Instantaneous local flow velocity [m/s]
U_b	Bulk flow velocity [m/s]
$u_* \equiv \sqrt{\tau/\rho_f}$	Fluid shear velocity [m/s]
ν_f	Kinematic fluid viscosity [m^2/s]
δ	Boundary layer thickness [m]
H	Flow thickness [m]
W	Flow width [m]
d	Characteristic particle diameter [m]
h	Transport layer thickness [m]
$\dot{\gamma}$	Particle shear rate (strain rate) [1/s]
T	Granular temperature [m^2/s^2]
g	Gravitational constant [m/s^2]
$\tilde{g} \equiv (1 - \rho_f/\rho_p)g$	Buoyancy-reduced gravitational constant [m/s^2]
M	Sediment transport load [kg/m^2]
Q	Sediment transport rate [kg/(ms)]
$\Theta \equiv \tau/((\rho_p - \rho_f)gd)$	Shields number or Shields parameter
$s \equiv \rho_p/\rho_f$	Particle-fluid-density ratio
$Re \equiv U_b H/\nu_f$	Reynolds number
$Re_* \equiv u_* d/\nu_f$	Shear Reynolds number
$\mathrm{Ga} \equiv \sqrt{(s-1)gd^3}/\nu_f$	Galileo number (also called Yalin parameter)
$\mathrm{St} \equiv s\lvert\mathbf{v_r}\rvert d/(9\nu_f)$	Stokes number, where $\lvert\mathbf{v_r}\rvert$ is the relative velocity between two particles just before they collide
$M_* \equiv M/(\rho_p d)$	Nondimensionalized sediment transport load
$Q_* \equiv Q/(\rho_p d\sqrt{(\rho_p/\rho_f - 1)gd})$	Nondimensionalized sediment transport rate
$I \equiv \dot{\gamma} d/\sqrt{P/\rho_p}$	Inertial number
$J \equiv \rho_f \nu_f \dot{\gamma}/P$	Viscous number
$K \equiv J + c_K I^2$	Viscoinertial number, where c_K is an order-unity fit parameter
$\mathrm{Pe} \equiv \dot{\gamma} d/\sqrt{T}$	Péclet number
$C_m = 1/2$	Added mass coefficient
$\kappa = 0.4$	von Kármán constant
ψ	Pocket angle
ψ_Y	Pocket angle for particles resting within the deepest pockets of the bed surface
L_{arm}	Lever arm length [m]
α	Bed slope angle
ΔZ	Critical dimensionless vertical particle displacement required for entrainment
ΔX	Critical dimensionless horizontal particle displacement required for entrainment
μ_C	Effective Coulomb friction coefficient encoding the combined effects of sliding and rolling friction in entrainment
$\mu \equiv -\tau_p/P$	Ratio between particle shear stress and particle pressure (bulk friction coefficient)
μ_g	Surface friction coefficient of granular particle
μ_s	Static friction coefficient of granular bulk (yield stress ratio)
μ_b	Bulk friction coefficient at the interface between bed and transport layer. In contrast to μ and μ_s, μ_b includes contributions from stresses associated with the particle fluctuation motion in addition to contributions from intergranular contacts.
$\xi \propto \lvert\mu - \mu_s\rvert^{-\nu}$	Correlation length associated with the yielding transition [m], where $\nu = 0.5$ is the critical exponent

$F, F_D, F_L, F_t, F_n, F_e$:	Instantaneous force applied by the fluid on a particle [kgm/s^2]. Subscript (D, L, t, n, e) refers to nature of force (drag, lift, tangential, normal, effective).
$T, T_D, T_L, T_t, T_n, T_e$:	Duration of turbulent fluctuation event [s]. Subscript (D, L, t, n, e) refers to nature of applied fluid force (drag, lift, tangential, normal, effective).
I_f	Impulse of turbulent fluctuation event [kgm/s]
E_f	Energy of turbulent fluctuation event [kgm^2/s^2]
F_c	Force resisting initial particle motion [kgm/s^2]
u_c	Critical instantaneous local flow velocity associated with resisting forces [m/s]
I_{fc}	Critical impulse required for fluid entrainment [kgm/s]
W_c	Critical work done by flow event required for fluid entrainment [kgm^2/s^2]
C_{eff}	Energy transfer coefficient, describing the fraction of energy transferred from flow to target particle during turbulent fluctuation event
$C \equiv \alpha_f^{-1} f(G)\sqrt{s}d/\delta$	Inverse dimensionless boundary layer thickness
$\alpha_f \equiv u_m/\overline{u}$	Ratio between the characteristic flow velocity u_m associated with the largest turbulent fluctuations and the local mean flow velocity $\overline{u}$
$T_{\max}$	Maximal duration of turbulent fluctuation events [s]
$f(G)$	Factor that encodes information about particle shape, orientation, and the pocket geometry
$\mathbf{v_i}$	Impact velocity [m/s]
$\mathbf{v_r}$ ($\mathbf{v_r^{2D}}$)	Rebound velocity (projected into incident plane) [m/s]
$\mathbf{v_e}$ ($\mathbf{v_e^{2D}}$)	Ejection velocity (projected into incident plane) [m/s]
θ_i	Impact angle
θ_r (θ_r^{2D})	Rebound angle (projected into incident plane)
θ_e (θ_e^{2D})	Ejection angle (projected into incident plane)
$\mathbf{E_i}$	Impact energy [kgm^2/s^2]
$\mathbf{E_e}$ ($\mathbf{E_e^{2D}}$)	Ejection energy (projected into incident plane) [kgm^2/s^2]
$\mathbf{N_e}$	Average number of ejected particles
$\mathbf{P_r}$	Rebound probability
$(e^{2D} \equiv \lvert\mathbf{v_r^{2D}}\rvert/\lvert\mathbf{v_i}\rvert)\ e \equiv \lvert\mathbf{v_r}\rvert/\lvert\mathbf{v_i}\rvert$	(Projected) rebound restitution coefficient
$e_z \equiv -v_{rz}/v_{iz}$	Vertical rebound restitution coefficient
$A, B, A^{2D}, B^{2D}, \chi, r, r^{2D}, n_0, \zeta$	Dimensionless parameters appearing in empirical or semiempirical relations describing the collision process between an incident bead and a granular packing
α_r	Normal rebound restitution coefficient in the impact plane
β_r	Tangential rebound restitution coefficient in the impact plane
ϵ	Restitution coefficient for binary particle collision
V_b	Effective value of the local particle velocity averaged over elevations near the bed surface [m/s]
f_{in}	Particle feeding frequency at flume entrance [1/s]
f_{out}	Frequency of particles passing an illuminated window near the flume exit [1/s]
f_Q	Fraction of active aeolian saltation transport
$v_\uparrow$	Initial particle velocity in thought experiment in section 4.2.1 [m/s]
$E_\uparrow$	Initial particle energy in thought experiment in section 4.2.1 [kgm^2/s^2]
E_c	Critical energy that $E_\uparrow$ must exceed for particle to continuously rebound along the surface [kgm^2/s^2]
$n_{\text{tr}}/n_{\text{tot}}$	Number of transported particles relative to the total number of bed surface particles
n_{v_t}	Number of particles that are faster than a certain velocity threshold v_t
z_h	Hop height [m]

t_h	Hop time [s]
$f(Re_*, z/d)$	Function given by equation (A1)
v_s	Settling velocity [m/s]
$U_x \equiv \overline{u_x}/\sqrt{s\tilde{g}d}$	Dimensionless transport layer-averaged fluid velocity
$V_x \equiv \overline{v_x}/\sqrt{s\tilde{g}d}$	Dimensionless transport layer-averaged horizontal particle velocity
$V_z \equiv \sqrt{\overline{v_z^2}}/\sqrt{s\tilde{g}d}$	Dimensionless transport layer-averaged vertical particle velocity
$Z \equiv \overline{z}/d$	Dimensionless transport layer thickness
$Z_\Delta = 0.7$	Dimensionless average elevation of the particles' center during particle-bed rebounds
z_o	Surface roughness [m]
c_1, c_2, c_3	Model constants in equations (33c)–(33e)
Bed sediment entrainment:	Mobilization of bed sediment
Fluid entrainment:	Entrainment caused by the action of flow forces
Incipient motion:	Initiation of sediment transport by fluid entrainment
Impact entrainment:	Entrainment caused by the impacts of transported particles onto the bed
Sediment transport:	Sediment motion caused by the shearing of an erodible sediment bed by flow of a Newtonian fluid
Aeolian sediment transport:	Wind-driven sediment transport
Fluvial sediment transport:	Liquid-driven sediment transport (despite its name, not limited to fluvial environments)
Nonsuspended sediment transport:	Sediment transport in which the fluid turbulence is unable to support the submerged particle weight
Saltation transport:	Nonsuspended sediment transport with comparably large transport layers ($h \gg d$)
Bedload transport:	Nonsuspended sediment transport with comparably small transport layers ($h \sim d$)
Transport capacity (or saturation):	Loosely, the maximum amount of sediment a given flow can carry without causing net sediment deposition at the bed. More precisely, in the context of nonsuspended transport of nearly monodisperse sediment, it is defined as a steady transport state at which any further net entrainment of bed sediment into the transport layer would weaken the mean turbulent flow to a degree at which it is no longer able to compensate the average energy loss of particles rebounding with the bed by their energy gain during their trajectories via fluid drag acceleration. The so defined transport capacity obeys equation (29).
Creeping:	A superslow granular motion, usually in the form of intermittent local particle rearrangements within the sediment bed (not limited to the bed surface), that occurs below a macroscopic yield criterion
Θ_t (τ_t):	Shields number (fluid shear stress) at a nonspecified transport threshold. For specifications, see below.
$t_{\mathrm{conv}} \propto \lvert\Theta - \Theta_t\rvert^{-\beta}$:	Time scale [s] for transport property to converge in the steady state near Θ_t, where β is a positive exponent
Shields diagram (Shields curve):	Diagram compiling measurements of Θ_t as a function of Re_* (the Shields curve $\Theta_t(Re_*)$) for fluvial bedload transport conditions
$\Theta_t^{\max}$ ($\tau_t^{\max}$):	Viscous yield stress. The upper limit of the threshold Shields number (fluid shear stress) in the Shields diagram, which is associated with viscous bedload transport. For $\Theta \lesssim \Theta_t^{\max}$, a sediment bed subjected to a laminar flow at low Shear Reynolds number Re_* may temporarily fail but will eventually rearrange itself into a more stable packing that resists the applied fluid shear stress. For $\Theta \gtrsim \Theta_t^{\max}$, a sediment bed subjected to a laminar flow can no longer find packing geometries that are able to resist the applied fluid shear stress.

Θ_t^{In} (τ_t^{In}): Initiation threshold. Shields number (fluid shear stress) at which the probability of fluid entrainment of bed particles exceeds zero (which, for turbulent fluvial bedload transport, occurs much below the Shields curve). For sediment beds subjected to turbulent flows, a critical fluid shear stress does no longer describe the fluid entrainment of individual particles. However, one can still define a Shields number (Θ_t^{In}) below which fluid entrainment does never occur. Like for $\Theta_t^{\max}$, transient behavior associated with the flow temporarily pushing particles from less stable to more stable pockets is excluded in the definition of Θ_t^{In}.

$\Theta_t^{\mathrm{In}\prime}$ ($\tau_t^{\mathrm{In}\prime}$): Rocking initiation threshold. Shields number (fluid shear stress) above (below) which there is a nonzero (zero) probability that peaks of flow forces associated with turbulent fluctuation events acting on bed particles exceed resisting forces. That is, there is a nonzero probability that particles rock (or wobble or oscillate) within their bed pockets. Rocking may ($\Theta_t^{\mathrm{In}\prime} = \Theta_t^{\mathrm{In}}$) or may not ($\Theta_t^{\mathrm{In}\prime} < \Theta_t^{\mathrm{In}}$) lead to complete entrainment depending on the maximal duration of the strongest possible turbulent fluctuation events.

Θ_t^{Rb} (τ_t^{Rb}): Rebound threshold. Shields number (fluid shear stress) above which the mean turbulent flow is able to compensate the average energy loss of transported particles rebounding with the bed by their energy gain during their trajectories via fluid drag acceleration, giving rise to a long-lasting rebound motion. In general, this threshold is unrelated to the entrainment of bed sediment. It is also the threshold that appears in most threshold shear stress-based sediment transport expressions.

$\Theta_t^{\mathrm{Rb}*}$ ($\Theta_t^{\mathrm{Rb}**}$): Modeled rebound threshold. Values of Θ_t^{Rb} from models that consider (neglect) that the near-surface flow can assist rebounding particles in escaping the bed surface.

Θ_t^{ImE} (τ_t^{ImE}): Impact entrainment threshold. Shields number (fluid shear stress) above which entrainment of bed sediment by impacts of transported particles onto the bed is able to compensate captures of long-lasting rebounders (see Θ_t^{Rb} above) by the bed. This threshold is arguably also the threshold of continuous nonsuspended sediment transport.

$\Theta_t^{\mathrm{Rb|ImE}}$ ($\tau_t^{\mathrm{Rb|ImE}}$): Modeled hybrid between rebound and impact entrainment threshold

Acknowledgments
All data shown in the figures of this review can be found in the following references: Peyneau and Roux (2008a), da Cruz et al. (2005), Kamrin and Koval (2014), Houssais et al. (2015), Allen and Kudrolli (2017),Allen and Kudrolli (2018), Diplas et al. (2008), Valyrakis (2013), Williams et al. (1994), Iversen and White (1982), Burr et al. (2015), Swann et al. (2020), Beladjine et al. (2007), Vowinckel et al. (2016), Salevan et al. (2017), Buffington and Montgomery (1997), Yalin and Karahan (1979), Loiseleux et al. (2005), Ouriemi et al. (2007), Bagnold (1937), Chepil (1945), Ho (2012), Martin and Kok (2018), and Zhu et al. (2019). We thank Michael Church and three anonymous reviewers for their critical reviews and numerous insightful comments and suggestions. T.P. acknowledges support from grant National Natural Science Foundation of China (No. 11750410687).

References

Agudo, J. R., Illigmann, C., Luzi, G., Laukart, A., Delgado, A., & Wierschem, A. (2017). Shear-induced incipient motion of a single sphere on uniform substrates at low particle Reynolds numbers. *Journal of Fluid Mechanics*, *825*, 284–314. https://doi.org/10.1017/jfm.2017.370

Alhamdi, S. F. H., & Bailey, S. C. C. (2017). Universality of local dissipation scales in turbulent boundary layer flows with and without free-stream turbulence. *Physics of Fluids*, *29*, 115103. https://doi.org/10.1063/1.4996200

Ali, S. Z., & Dey, S. (2016). Hydrodynamics of sediment threshold. *Physics of Fluids*, *28*, 75103. https://doi.org/10.1063/1.4955103

Allen, B., & Kudrolli, A. (2017). Depth resolved granular transport driven by shearing fluid flow. *Physical Review Fluids*, *2*, 24304. https://doi.org/10.1103/PhysRevFluids.2.024304

Allen, B., & Kudrolli, A. (2018). Granular bed consolidation, creep, and armoring under subcritical fluid flow. *Physical Review Fluids*, *3*, 74305. https://doi.org/10.1103/PhysRevFluids.3.074305

Almeida, M. P., Parteli, E. J. R., Andrade, J. S., & Herrmann, H. J. (2008). Giant saltation on Mars. *Proceedings of the National Academy of Science*, *105*(17), 6222–6226. https://doi.org/10.1073/pnas.0800202105

Amarsid, L., Delenne, J.-Y., Mutabaruka, P., Monerie, Y., Perales, F., & Radjaï, F. (2017). Viscoinertial regime of immersed granular flows. *Physical Review E*, *96*, 12901. https://doi.org/10.1103/PhysRevE.96.012901

Ammi, M., Oger, L., Beladjine, D., & Valance, A. (2009). Three-dimensional analysis of the collision process of a bead on a granular packing. *Physical Review E*, *79*, 21305. https://doi.org/10.1103/PhysRevE.79.021305

Amon, A., Bertoni, R., & Crassous, J. (2013). Experimental investigation of plastic deformations before a granular avalanche. *Physical Review E*, *87*, 12204. https://doi.org/10.1103/PhysRevE.87.012204

Ancey, C., Bigillon, F., Frey, P., Lanier, J., & Ducret, R. (2002). Saltating motion of a bead in a rapid water stream. *Physical Review E*, *66*, 36306. https://doi.org/10.1103/PhysRevE.66.036306

Ancey, C., Böhm, T., Jodeau, M., & Frey, P. (2006). Statistical description of sediment transport experiments. *Physical Review E*, *74*, 11302. https://doi.org/10.1103/PhysRevE.74.011302

Ancey, C., Bohorquez, P., & Heyman, J. (2015). Stochastic interpretation of the advection-diffusion equation and its relevance to bed load transport. *Journal of Geophysical Research: Earth Surface*, *120*, 529–2551. https://doi.org/10.1002/2014JF003421

Ancey, C., Coussot, P., & Evesque, P. (1999). A theoretical framework for granular suspensions in a steady simple shear flow. *Journal of Rheology*, *43*(6), 1673–1699. https://doi.org/10.1122/1.551067
Ancey, C., Davison, A. C., Böhm, T., Jodeau, M., & Frey, P. (2008). Entrainment and motion of coarse particles in a shallow water stream down a steep slope. *Journal of Fluid Mechanics*, *595*, 83–114. https://doi.org/10.1017/S0022112007008774
Anderson, R. S., & Haff, P. K. (1988). Simulation of eolian saltation. *Science*, *241*, 820–823. https://doi.org/10.1126/science.241.4867.820
Anderson, R. S., & Haff, P. K. (1991). Wind modification and bed response during saltation of sand in air. *Acta Mechanica Supplementum*, *1*, 21–51. https://doi.org/10.1007/978-3-7091-6706-9_2
Anderson, R. S., & Hallet, B. (1986). Sediment transport by wind: Toward a general model. *Geological Society of America Bulletin*, *97*, 523–535. https://doi.org/10.1130/0016-7606(1986)97<523:STBWTA>2.0.CO;2
Andreotti, B. (2004). A two-species model of aeolian sand transport. *Journal of Fluid Mechanics*, *510*, 47–70. https://doi.org/10.1017/S0022112004009073
Apperley, L. W., & Raudkivi, A. J. (1989). The entrainment of sediments by the turbulent flow of water. *Hydrobiologia*, *176*(1), 39–49. https://doi.org/10.1007/978-94-009-2376-8_5
Aussillous, P., Zou, Z., Guazzelli, E., Yan, L., & Wyart, M. (2016). Scale-free channeling patterns near the onset of erosion of sheared granular beds. *Proceedings of the National Academy of Science*, *113*(42), 11,788–11,793. https://doi.org/10.1073/pnas.1609023113
Ayoub, F., Avouac, J.-P., Newman, C. E., Richardson, M. I., Lucas, A., Leprince, S., & Bridges, N. (2014). Threshold for sand mobility on Mars calibrated from seasonal variations of sand flux. *Nature Communications*, *5*, 5096. https://doi.org/10.1038/ncomms6096
Azéma, E., & Radjaï, F. (2010). Stress-strain behavior and geometrical properties of packings of elongated particles. *Physical Review E*, *81*, 051,304. https://doi.org/10.1103/PhysRevE.81.051304
Azéma, E., & Radjaï, F. (2014). Internal structure of inertial granular flows. *Physical Review Letters*, *112*, 78001. https://doi.org/10.1103/PhysRevLett.112.078001
Bachelet, V., Mangeney, A., de Rosny, J., Toussaint, R., & Farin, M. (2018). Elastic wave generated by granular impact on rough and erodible surfaces. *Journal of Applied Physics*, *123*, 44901. https://doi.org/10.1063/1.5012979
Bagnold, R. A. (1936). The meovement of desert sand. *Proceedings of the Royal Society of London Series A*, *157*, 594–620. https://doi.org/10.1098/rspa.1936.0218
Bagnold, R. A. (1937). The transport of sand by wind. *The Geographical Journal*, *89*(5), 409–438. https://doi.org/10.2307/1786411
Bagnold, R. A. (1938). The measurement of sand storms. *Proceedings of the Royal Society of London Series A*, *167*, 282–291. https://doi.org/10.1098/rspa.1938.0132
Bagnold, R. A. (1941). *The physics of blown sand and desert dunes*. New York: Methuen.
Bagnold, R. A. (1956). The flow of cohesionless grains in fluid. *Philosophical Transactions of the Royal Society of London A*, *249*, 235–297. https://doi.org/10.1098/rsta.1956.0020
Bagnold, R. A. (1966). *An approach to the sediment transport problem from general physics, in US Geological Survey Professional Paper 422-I*. Washington, DC: U.S. Government Printing Office. https://doi.org/10.3133/pp422I
Bagnold, R. A. (1973). The nature of saltation and 'bed-load' transport in water. *Proceedings of the Royal Society of London Series A*, *332*, 473–504. https://doi.org/10.1098/rspa.1973.0038
Baker, M. M., Newman, C. E., Lapotre, M. G. A., Sullivan, R., Bridges, N. T., & Lewis, K. W. (2018). Coarse sediment transport in the modern Martian environment. *Journal of Geophysical Research: Planets*, *123*(6), 1380–1394. https://doi.org/10.1002/2017JE005513
Baran, O., Ertas, D., & Halsey, T. C. (2006). Velocity correlations in dense gravity-driven granular chute flow. *Physical Review E*, *74*, 51302. https://doi.org/10.1103/PhysRevE.74.051302
Barchyn, T. E., & Hugenholtz, C. H. (2011). Comparison of four methods to calculate aeolian sediment transport threshold from field data: Implications for transport prediction and discussion of method evolution. *Geomorphology*, *129*, 190–203. https://doi.org/10.1016/j.geomorph.2011.01.022
Beladjine, D., Ammi, M., Oger, L., & Valance, A. (2007). Collision process between an incident bead and a three-dimensional granular packing. *Physical Review E*, *75*, 61305. https://doi.org/10.1103/PhysRevE.75.061305
Berzi, D., Jenkins, J. T., & Valance, A. (2016). Periodic saltation over hydrodynamically rough beds: Aeolian to aquatic. *Journal of Fluid Mechanics*, *786*(1), 190–209. https://doi.org/10.1017/jfm.2015.601
Berzi, D., Valance, A., & Jenkins, J. T. (2017). The threshold for continuing saltation on Earth and other solar system bodies. *Journal of Geophysical Research: Earth Surface*, *122*, 1374–1388. https://doi.org/10.1002/2016JF003982
Bo, T. L., Fu, L. T., Liu, L., & Zheng, X. J. (2017). An improved numerical model suggests potential differences of wind-blown sand between on Earth and Mars. *Journal of Geophysical Research: Atmospheres*, *122*, 5823–5836. https://doi.org/10.1002/2016JD026132
Böhm, T., Ancey, C., Frey, P., Reboud, J. L., & Ducottet, C. (2004). Fluctuations of the solid discharge of gravity-driven particle flows in a turbulent stream. *Physical Review E*, *69*, 61307. https://doi.org/10.1103/PhysRevE.69.061307
Boulton, G. S., & Hindmarsh, R. C. A. (1987). Sediment deformation beneath glaciers: Rheology and geological consequences. *Journal of Geophysical Research: Solid Earth*, *92*(B9), 9059–9082. https://doi.org/10.1029/JB092iB09p09059
Bourke, M. C., Lancaster, N., Fenton, L. K., Parteli, E. J. R., Zimbelman, J. R., & Radebaugh, J. (2010). Extraterrestrial dunes: An introduction to the special issue on planetary dune systems. *Geomorphology*, *121*, 1–14. https://doi.org/10.1016/j.geomorph.2010.04.007
Bourrier, F., Nicot, F., & Darve, F. (2008). Physical processes within a 2D granular layer during an impact. *Granular Matter*, *10*, 415–437. https://doi.org/10.1007/s10035-008-0108-0
Bouzid, M., Izzet, A., Trulsson, M., Clément, E., Claudin, P., & Andreotti, B. (2015). Non-local rheology in dense granular flows—Revisiting the concept of fluidity. *The European Physics Journal E*, *38*, 125. https://doi.org/10.1140/epje/i2015-15125-1
Bouzid, M., Trulsson, M., Claudin, P., Clément, E., & Andreotti, B. (2013). Nonlocal rheology of granular flows across yield conditions. *Physical Review Letters*, *111*, 238301. https://doi.org/10.1103/PhysRevLett.111.238301
Bouzid, M., Trulsson, M., Izzet, A., Favier de Coulomb, A., Claudin, P., Clément, E., & Andreotti, B. (2017). Non-local rheology of dense granular flows. *The European Physical Journal E*, *140*, 11013. https://doi.org/10.1051/epjconf/201714011013
Boyer, F., Guazzelli, E., & Pouliquen, O. (2011). Unifying suspension and granular rheology. *Physical Review Letters*, *107*, 188301. https://doi.org/10.1103/PhysRevLett.107.188301
Brahms, A. (1757). *Anfangsgründe der Deich- und Wasserbaukunst*. Aurich: Tapper.
Bridges, N. T., Ayoub, F., Avouac, J.-P., Leprince, S., Lucas, A., & Mattson, S. (2012). Earth-like sand fluxes on Mars. *Nature*, *485*, 339–342. https://doi.org/10.1038/nature11022
Bridges, N. T., Bourke, M. C., Geissler, P. E., Banks, M. E., Colon, C., Diniega, S., et al. (2012). Planet-wide sand motion on Mars. *Geology*, *40*(1), 31–34. https://doi.org/10.1130/G32373.1
Buffington, J. M. (1999). The legend of A. F. Shields. *Journal of Hydraulic Engineering*, *125*(4), 376–387. https://doi.org/10.1061/(ASCE)0733-9429(1999)125:4(376)

Buffington, J. M., Dietrich, W. E., & Kirchner, J. W. (1992). Friction angle measurements on a naturally formed gravel streambed: Implications for critical boundary shear stress. *Water Resources Research*, *28*(2), 411–425. https://doi.org/10.1029/91WR02529

Buffington, J. M., & Montgomery, D. R. (1997). A systematic analysis of eight decades of incipient motion studies, with special reference to gravel-bedded rivers. *Water Resources Research*, *33*(8), 1993–2029. https://doi.org/10.1029/96WR03190

Bunte, K., & Abt, S. R. (2005). Effect of sampling time on measured gravel bed load transport rates in a coarse-bedded stream. *Water Resources Research*, *41*, W11405. https://doi.org/10.1029/2004WR003880

Burr, D. M., Bridges, N. T., Marshall, J. R., Smith, J. K., White, B. R., & Emery, J. P. (2015). Higher-than-predicted saltation threshold wind speeds on Titan. *Nature*, *517*(7532), 60–63. https://doi.org/10.1038/nature14088

Camenen, B. (2007). Simple and general formula for the settling velocity of particles. *Journal of Hydraulic Engineering*, *133*(2), 229–233. https://doi.org/10.1061/(ASCE)0733-9429(2007)133:2(229)

Cameron, S. M., Nikora, V. I., & Marusic, I. (2019). Drag forces on a bed particle in open-channel flow: Effects of pressure spatial fluctuations and very-large-scale motions. *Journal of Fluid Mechanics*, *863*, 494–512. https://doi.org/10.1017/jfm.2018.1003

Cameron, S., Nikora, V., & Witz, M. (2020). Entrainment of sediment particles by very large-scale motions. *Journal of Fluid Mechanics*, *888*, A7. https://doi.org/10.1017/jfm.2020.24

Candelier, R., & Dauchot, O. (2009). Creep motion of an intruder within a granular glass close to jamming. *Physical Review Letters*, *103*, 128001. https://doi.org/10.1103/PhysRevLett.103.128001

Cao, Z., Pender, G., & Meng, J. (2006). Explicit formulation of the shields diagram for incipient motion of sediment. *Journal of Hydraulic Engineering*, *132*(10), 1097–1099. https://doi.org/10.1061/(ASCE)0733-9429(2006)132:10(1097)

Carneiro, M. V., Araújo, N. A. M., Pähtz, T., & Herrmann, H. J. (2013). Midair collisions enhance saltation. *Physical Review Letters*, *111*(5), 58001. https://doi.org/10.1103/PhysRevLett.111.058001

Carneiro, M. V., Pähtz, T., & Herrmann, H. J. (2011). Jump at the onset of saltation. *Physical Review Letters*, *107*(9), 98001. https://doi.org/10.1103/PhysRevLett.107.098001

Carneiro, M. V., Rasmussen, K. R., & Herrmann, H. J. (2015). Bursts in discontinuous aeolian saltation. *Scientific Reports*, *5*, 11109. https://doi.org/10.1038/srep11109

Castellanos, A. (2005). The relationship between attractive interparticle forces and bulk behaviour in dry and uncharged fine powders. *Advances in Physics*, *54*(4), 263–376. https://doi.org/10.1080/17461390500402657

Celik, A. O., Diplas, P., & Dancey, C. L. (2013). Instantaneous turbulent forces and impulse on a rough bed: Implications for initiation of bed material movement. *Water Resources Research*, *49*, 2213–2227. https://doi.org/10.1002/wrcr.20210

Celik, A. O., Diplas, P., & Dancey, C. L. (2014). Instantaneous pressure measurements on a spherical grain under threshold flow conditions. *Journal of Fluid Mechanics*, *741*, 60–97. https://doi.org/10.1017/jfm.2013.632

Celik, A. O., Diplas, P., Dancey, C. L., & Valyrakis, M. (2010). Impulse and particle dislodgement under turbulent flow conditions. *Physics of Fluids*, *22*, 46601. https://doi.org/10.1063/1.3385433

Charru, F., Mouilleron, H., & Eiff, O. (2004). Erosion and deposition of particles on a bed sheared by a viscous flow. *Journal of Fluid Mechanics*, *519*, 55–80. https://doi.org/10.1017/S0022112004001028

Chen, Y., Zhang, J., Huang, N., & Xu, B. (2019). An experimental study on splash functions of natural sand-bed collision. *Journal of Geophysical Research: Atmospheres*, *124*, 7226–7235. https://doi.org/10.1029/2018JD029967

Cheng, N. S., Tang, H., & Yan, J. (2018). Low-submergence effect on incipient sediment motion. *Journal of Engineering Mechanics*, *144*(12), 4018111. https://doi.org/10.1061/(ASCE)EM.1943-7889.0001540

Chepil, W. S. (1945). Dynamics of wind erosion: II. *Initiation of soil movement, Soil Science*, *60*(5), 397–411. https://doi.org/10.1097/00010694-194511000-00005

Chojnacki, M., Johnson, J. R., Moersch, J. E., Fenton, L. K., Michaels, T. I., & Bell, J. F. III (2015). Persistent aeolian activity at Endeavour crater, Meridiani Planum, Mars; new observations from orbit and the surface. *Icarus*, *251*, 275–290. https://doi.org/10.1016/j.icarus.2014.04.044

Clark, A. H., Kondic, L., & Behringer, R. P. (2012). Particle scale dynamics in granular impact. *Physical Review Letters*, *109*, 238,302. https://doi.org/10.1103/PhysRevLett.109.238302

Clark, A. H., Kondic, L., & Behringer, R. P. (2016). Steady flow dynamics during granular impact. *Physical Review E*, *93*, 50901(R). https://doi.org/10.1103/PhysRevE.93.050901

Clark, A. H., Petersen, A. J., Kondic, L., & Behringer, R. P. (2015). Nonlinear force propagation during granular impact. *Physical Review Letters*, *114*, 144502. https://doi.org/10.1103/PhysRevLett.114.144502

Clark, A. H., Shattuck, M. D., Ouellette, N. T., & O'Hern, C. S. (2015). Onset and cessation of motion in hydrodynamically sheared granular beds. *Physical Review E*, *92*(4), 42202. https://doi.org/10.1103/PhysRevE.92.042202

Clark, A. H., Shattuck, M. D., Ouellette, N. T., & O'Hern, C. S. (2017). Role of grain dynamics in determining the onset of sediment transport. *Physical Review Fluids*, *2*, 34305. https://doi.org/10.1103/PhysRevFluids.2.034305

Clark, A. H., Thompson, J. D., Shattuck, M. D., Ouellette, N. T., & O'Hern, C. S. (2018). Critical scaling near the yielding transition in granular media. *Physical Review E*, *97*(6), 62901. https://doi.org/10.1103/PhysRevE.97.062901

Claudin, P., & Andreotti, B. (2006). A scaling law for aeolian dunes on Mars, Venus, Earth, and for subaqueous ripples. *Earth and Planetary Science Letters*, *252*, 30–44. https://doi.org/10.1016/j.epsl.2006.09.004

Comola, F., Gaume, J., Kok, J. F., & Lehning, M. (2019). Cohesion-induced enhancement of aeolian saltation. *Geophysical Research Letters*, *46*(10), 5566–5574. https://doi.org/10.1029/2019GL082195

Comola, F., Kok, J. F., Chamecki, M., & Martin, R. L. (2019). The intermittency of wind-driven sand transport. *Geophysical Research Letters*, *46*, 13,430–13,440. https://doi.org/10.1029/2019GL085739

Comola, F., & Lehning, M. (2017). Energy- and momentum-conserving model of splash entrainment in sand and snow saltation. *Geophysical Research Letters*, *44*, 1601–1609. https://doi.org/10.1002/2016GL071822

Cornelis, W. M., & Gabriels, D. (2004). A simple model for the prediction of the deflation threshold shear velocity of dry loose particles. *Sedimentology*, *51*, 39–51. https://doi.org/10.1111/j.1365-3091.2004.00609.x

Crassous, J., Beladjine, D., & Valance, A. (2007). Impact of a projectile on a granular medium described by a collision model. *Physical Review Letters*, *99*, 248001. https://doi.org/10.1103/PhysRevLett.99.248001

Crassous, J., Metayer, J. F., Richard, P., & Laroche, C. (2008). Experimental study of a creeping granular flow at very low velocity. *Journal of Statistical Mechanics: Theory and Experiment*, *2008*(03), P03009. https://doi.org/10.1088/1742-5468/2008/03/P03009

Creyssels, M., Dupont, P., Ould El Moctar, A., Valance, A., Cantat, I., Jenkins, J. T., et al. (2009). Saltating particles in a turbulent boundary layer: Experiment and theory. *Journal of Fluid Mechanics*, *625*, 47–74. https://doi.org/10.1017/S0022112008005491

Cundall, P. A., & Strack, O. D. L. (1979). A discrete numerical model for granular assemblies. *Geotechnique*, *291*, 47–65. https://doi.org/10.1680/geot.1979.29.1.47

da Cruz, F., Emam, S., Prochnow, M., Roux, J.-N., & Chevoir, F. (2005). Rheophysics of dense granular materials: Discrete simulation of plane shear flows. *Physical Review E*, *72*, 21309. https://doi.org/10.1103/PhysRevE.72.021309

Deskos, G., & Diplas, P. (2018). Incipient motion of a non-cohesive particle under stokes flow conditions. *International Journal of Multiphase Flow*, *99*, 151–161. https://doi.org/10.1016/j.ijmultiphaseflow.2017.09.015

de Vet, S. J., Merrison, J. P., Mittelmeijer-Hazeleger, M. C., van Loon, E. E., & Cammeraat, L. H. (2014). Effects of rolling on wind-induced detachment thresholds of volcanic glass on Mars. *Planetary and Space Science*, *103*, 205–218. https://doi.org/10.1016/j.pss.2014.07.012

Dey, S. (1999). Sediment threshold. *Applied Mathematical Modelling*, *23*, 399–417. https://doi.org/10.1016/S0307-904X(98)10081-1

Dey, S., & Ali, S. Z. (2018). Review article: Advances in modeling of bed particle entrainment sheared by turbulent flow. *Physics of Fluids*, *30*, 61301. https://doi.org/10.1063/1.5030458

Dey, S., & Ali, S. Z. (2019). Bed sediment entrainment by streamflow: State of the science. *Sedimentology*, *66*(5), 1449–1485. https://doi.org/10.1111/sed.12566

Dey, S., Das, R., Gaudio, R., & Bose, S. K. (2012). Turbulence in mobile-bed streams. *Acta Geophysica*, *60*(6), 1547–1588. https://doi.org/10.2478/s11600-012-0055-3

Dey, S., & Papanicolaou, A. (2008). Sediment threshold under stream flow: A state-of-the-art review. *KSCE Journal of Civil Engineering*, *12*(1), 45–60. https://doi.org/10.1007/s12205-008-8045-3

Dinehart, R. L. (1999). Correlative velocity fluctuations over a gravel river bed. *Water Resources Research*, *35*(2), 569–582. https://doi.org/10.1029/1998WR900038

Diplas, P., Dancey, C. L., Celik, A. O., Valyrakis, M., Greer, K., & Akar, T. (2008). The role of impulse on the initiation of particle movement under turbulent flow conditions. *Science*, *322*(5902), 717–720. https://doi.org/10.1126/science.1158954

Divoux, T., Gayvallet, H., & Géminard, J. C. (2008). Creep motion of a granular pile induced by thermal cycling. *Physical Review Letters*, *101*, 148303. https://doi.org/10.1103/PhysRevLett.101.148303

Dong, Z., Liu, X., Li, F., Wang, H., & Zhao, A. (2002). Impact-entrainment relationship in a saltating cloud. *Earth Surface Processes and Landforms*, *27*(6), 641–658. https://doi.org/10.1002/esp.341

Dong, Z., Liu, X., Wang, H., & Wang, X. (2003). Aeolian sand transport: A wind tunnel model. *Sedimentary Geology*, *161*, 71–83. https://doi.org/10.1016/S0037-0738(02)00396-2

Drake, T. G., & Calantoni, J. (2001). Discrete particle model for sheet flow sediment transport in the nearshore. *Journal of Geophysical Research*, *106*(C9), 19,859–19,868. https://doi.org/10.1029/2000JC000611

Drake, T. G., Shreve, R. L., Dietrich, W. E., Whitings, P. J., & Leopold, L. B. (1988). Bedload transport of fine gravel observed by motion-picture photography. *Journal of Fluid Mechanics*, *192*, 193–217. https://doi.org/10.1017/S0022112088001831

Drucker, D. C., & Prager, W. (1952). Soil mechanics and plastic analysis or limit design. *Quarterly of Applied Mathematics*, *10*(2), 157–165. https://www.jstor.org/stable/43633942

Duan, S., Cheng, N., & Xie, L. (2013). A new statistical model for threshold friction velocity of sand particle motion. *Catena*, *104*, 32–38. https://doi.org/10.1016/j.catena.2012.04.009

Duan, S. Z., Zhu, W., & Zheng, X. J. (2013). Numerical investigation on two-grain-bed collisions in windblown sand transport. *Powder Technology*, *235*, 431–436. https://doi.org/10.1016/j.powtec.2012.10.059

Durán, O., Andreotti, B., & Claudin, P. (2012). Numerical simulation of turbulent sediment transport, from bed load to saltation. *Physics of Fluids*, *24*, 103306. https://doi.org/10.1063/1.4757662

Durán, O., Claudin, P., & Andreotti, B. (2011). On aeolian transport: Grain-scale interactions, dynamical mechanisms and scaling laws. *Aeolian Research*, *3*, 243–270. https://doi.org/10.1016/j.aeolia.2011.07.006

Durán Vinent, O., Andreotti, B., Claudin, P., & Winter, C. (2019). A unified model of ripples and dunes in water and planetary environments. *Nature Geoscience*, *12*, 345–350. https://doi.org/10.1038/s41561-019-0336-4

Dwivedi, A., Melville, B. W., Shamseldin, A. Y., & Guha, T. K. (2010a). Drag force on a sediment particle from point velocity measurements: A spectral approach. *Water Resources Research*, *46*, W10,529. https://doi.org/10.1029/2009WR008643

Dwivedi, A., Melville, B. W., Shamseldin, A. Y., & Guha, T. K. (2010b). Flow structures and hydrodynamic force during sediment entrainment. *Water Resources Research*, *47*, W01,509. https://doi.org/10.1029/2010WR009089

Edwards, B. L., & Namikas, S. L. (2015). Characterizing the sediment bed in terms of resistance to motion: Toward an improved model of saltation thresholds for aeolian transport. *Aeolian Research*, *19*, 123–128. https://doi.org/10.1016/j.aeolia.2015.10.004

Einstein, H. A. (1950). *The bed-load function for sediment transportation in open channel flows*. Washington, DC: United States Department of Agriculture. https://doi.org/10.22004/ag.econ.156389

Einstein, H. A., & El-Samni, E. S. A. (1949). Hydrodynamic forces on a rough wall. *Reviews of Modern Physics*, *21*(3), 520–524. https://doi.org/10.1103/RevModPhys.21.520

Elghannay, H. A., & Tafti, D. K. (2017). Sensitivity of numerical parameters on DEM predictions of sediment transport. *Particulate Science and Technology*, *36*(4), 438–446. https://doi.org/10.1080/02726351.2017.1352638

Fenistein, D., & van Hecke, M. (2003). Kinematics: Wide shear zones in granular bulk flow. *Nature*, *425*(6955), 256. https://doi.org/10.1038/425256a

Ferdowsi, B., Ortiz, C. P., Houssais, M., & Jerolmack, D. J. (2017). River-bed armouring as a granular segregation phenomenon. *Nature Communications*, *8*(1), 1363. https://doi.org/10.1038/s41467-017-01681-3

Ferdowsi, B., Ortiz, C. P., & Jerolmack, D. J. (2018). Glassy dynamics of landscape evolution. *Proceedings of the National Academy of Sciences*, *115*(19), 4827–4832. https://doi.org/10.1073/pnas.1715250115

Forterre, Y., & Pouliquen, O. (2008). Flows of dense granular media. *Annual Review of Fluid Mechanics*, *40*, 1–24. https://doi.org/10.1146/annurev.fluid.40.111406.102142

Francis, J. R. D. (1973). Experiments on the motion of solitary grains along the bed of a water-stream. *Philosophical Transactions of the Royal Society of London A*, *332*, 443–471. https://doi.org/10.1098/rspa.1973.0037

Frey, P., & Church, M. (2009). How river beds move. *Science*, *325*(5947), 1509–1510. https://doi.org/10.1126/science.1178516

Frey, P., & Church, M. (2011). Bedload: A granular phenomenon. *Earth Surface Processes and Landforms*, *36*, 58–69. https://doi.org/10.1002/esp.2103

Gaudel, N., & De Richter, S. K. (2019). Effect of vibrations on granular material flows down an inclined plane using DEM simulations. *Powder Technology*, *346*, 256–264. https://doi.org/10.1016/j.powtec.2019.01.080

Gilbert, G. K. (1914). *The transportation of debris by running water*, in US Geological Survey Professional Paper 86. Washington, DC: U.S. Geological Survey. https://doi.org/10.3133/pp86

Gillette, D. A., Adams, J., Endo, A., Smith, D., & Kihl, R. (1980). Threshold velocities for input of soil particles into the air by desert soils. *Journal of Geophysical Research*, *85*(C10), 5621–5630. https://doi.org/10.1029/JC085iC10p05621

Giménez-Curto, L. A., & Corniero, M. A. (2009). Entrainment threshold of cohesionless sediment grains under steady flow of air and water. *Sedimentology*, *56*(2), 493–509. https://doi.org/10.1111/j.1365-3091.2008.00981.x
Gondret, P., Lance, M., & Petit, L. (2002). Bouncing motion of spherical particles in fluids. *Physics of Fluids*, *14*, 643. https://doi.org/10.1063/1.1427920
González, C., Richter, D. H., Bolster, D., Bateman, S., Calantoni, J., & Escauriaza, C. (2017). Characterization of bedload intermittency near the threshold of motion using a Lagrangian sediment transport model. *Environmental Fluid Mechanics*, *17*(1), 111–137. https://doi.org/10.1007/s10652-016-9476-x
Gordon, M., & McKenna Neuman, C. (2009). A comparison of collisions of saltating grains with loose and consolidated silt surfaces. *Journal of Geophysical Research*, *114*, F04015. https://doi.org/10.1029/2009JF001330
Gordon, M., & McKenna Neuman, C. (2011). A study of particle splash on developing ripple forms for two bed materials. *Geomorphology*, *129*, 79–91. https://doi.org/10.1016/j.geomorph.2011.01.015
Govers, G. (1987). Initiation of motion in overland flow. *Sedimentology*, *34*, 1157–1164. https://doi.org/10.1111/j.1365-3091.1987.tb00598.x
Graf, W. H., & Pazis, G. C. (1977). Desposition and erosion in an alluvial channel. *Journal of Hydraulic Research*, *15*(2), 151–166. https://doi.org/10.1080/00221687709499653
Greeley, R., Iversen, J., Leach, R., Marshall, J., White, B., & Williams, S. (1984). Windblown sand on Venus: Preliminary results of laboratory simulations. *Icarus*, *57*, 112–124. https://doi.org/10.1016/0019-1035(84)90013-7
Greeley, R., Leach, R., White, B., Iversen, J., & Pollack, J. (1980). Threshold windspeeds for sand on mars: Wind tunnel simulations. *Geophysical Research Letters*, *7*(2), 121–124. https://doi.org/10.1029/GL007i002p00121
Greeley, R., & Marshall, J. R. (1985). Transport of Venusian rolling 'stones' by wind? *Nature*, *313*, 771–773. https://doi.org/10.1038/313771a0
Greeley, R., White, B., Leach, R., Iversen, J., & Pollack, J. (1976). Mars: Wind friction speeds for particle movement. *Geophysical Research Letters*, *3*(8), 417–420. https://doi.org/10.1029/GL003i008p00417
Guazzelli, E., & Pouliquen, O. (2018). Rheology of dense granular suspensions. *Journal of Fluid Mechanics*, *852*, P1. https://doi.org/10.1017/jfm.2018.548
Guo, J., & Julien, P. Y. (2007). Buffer law and transitional roughness effect in turbulent open-channel flows. In *The Fifth International Symposium on Environmental Hydraulics (ISEH V)* (Vol. 5, pp. 1–6). Tempe, Arizona: University of Nebraska - Lincoln.
Haff, P. K., & Anderson, R. S. (1993). Grain scale simulations of loose sedimentary beds: The example of grain-bed impacts in aeolian saltation. *Sedimentology*, *40*, 175–198. https://doi.org/10.1111/j.1365-3091.1993.tb01760.x
Hansen, C. J., McEwen, A. S., Ingersoll, A. P., & Terrile, R. J. (1990). Surface and airborne evidence for plumes and winds on triton. *Science*, *250*(4979), 421–424. https://doi.org/10.1126/science.250.4979.421
He, S., & Ohara, N. (2017). A new formula for estimating the threshold wind speed for snow movement. *Journal of Advances in Modeling Earth Systems*, *9*, 2514–2525. https://doi.org/10.1002/2017MS000982
Heathershaw, A. D., & Thorne, P. D. (1985). Sea-bed noises reveal role of turbulent bursting phenomenon in sediment transport by tidal currents. *Nature*, *316*, 339–342. https://doi.org/10.1038/316339a0
Helland-Hansen, E., Klingeman, P. C., & Milhous, R. T. (1974). Sediment transport at low shields-parameter values. *Journal of the Hydraulics Division*, *100*(1), 261–265.
Henann, D. L., & Kamrin, K. (2013). A predictive, size-dependent continuum model for dense granular flows. *Proceedings of the National Academy of Sciences*, *110*(17), 6730–6735. https://doi.org/10.1073/pnas.1219153110
Herminghaus, S. (2005). Dynamics of wet granular matter. *Advances in Physics*, *54*(3), 221–261. https://doi.org/10.1080/00018730500167855
Heyman, J., Bohorquez, P., & Ancey, C. (2016). Entrainment, motion, and deposition of coarse particles transported by water over a sloping mobile bed. *Journal of Geophysical Research: Earth Surface*, *121*, 1931–1952. https://doi.org/10.1002/2015JF003672
Heyman, J., Mettra, F., Ma, H. B., & Ancey, C. (2013). Statistics of bedload transport over steep slopes: Separation of time scales and collective motion. *Geophysical Research Letters*, *40*, 128–133. https://doi.org/10.1029/2012GL054280
Ho, T. D. (2012), Etude expérimentale du transport de particules dans une couche limite turbulente, Ph.D. thesis, University of Rennes, Rennes, France.
Ho, T. D., Dupont, P., Ould El Moctar, A., & Valance, A. (2012). Particle velocity distribution in saltation transport. *Physical Review E*, *85*, 052,301. https://doi.org/10.1103/PhysRevE.85.052301
Hofland, B. (2005). Rock & roll: Turbulence-induced damage to granular bed protections, Ph.D. thesis, Delft University of Technology, Delft, The Netherlands.
Hofland, B., Booij, R., & Battjes, J. (2005). Measurement of fluctuating pressures on coarse bed material. *Journal of Hydraulic Engineering*, *131*(9), 770–781. https://doi.org/10.1061/(ASCE)0733-9429(2005)131:9(770)
Hong, A., Tao, M., & Kudrolli, A. (2015). Onset of erosion of a granular bed in a channel driven by fluid flow. *Physics of Fluids*, *27*(1), 013,301. https://doi.org/10.1063/1.4905146
Houssais, M., & Jerolmack, D. J. (2017). Toward a unifying constitutive relation for sediment transport across environments. *Geomorphology*, *277*, 251–264. https://doi.org/10.1016/j.geomorph.2016.03.026
Houssais, M., Ortiz, C. P., Durian, D. J., & Jerolmack, D. J. (2015). Onset of sediment transport is a continuous transition driven by fluid shear and granular creep. *Nature Communications*, *6*, 6527. https://doi.org/10.1038/ncomms7527
Houssais, M., Ortiz, C. P., Durian, D. J., & Jerolmack, D. J. (2016). Rheology of sediment transported by a laminar flow. *Physical Review E*, *94*, 062,609. https://doi.org/10.1103/PhysRevE.94.062609
Huang, H. J., Bo, T. L., & Zhang, R. (2017). Exploration of splash function and lateral velocity based on three-dimensional mixed-size grain/bed collision. *Granular Matter*, *19*, 73. https://doi.org/10.1007/s10035-017-0759-9
Huang, H. J., Bo, T. L., & Zheng, X. J. (2014). Numerical modeling of wind-blown sand on Mars. *The European Physical Journal E*, *37*(9), 80. https://doi.org/10.1140/epje/i2014-14080-7
Iversen, J., Greeley, R., Marshall, J. R., & Pollack, J. B. (1987). Aeolian saltation threshold: The effect of density ratio. *Sedimentology*, *34*, 699–706. https://doi.org/10.1111/j.1365-3091.1987.tb00795.x
Iversen, J. D., Pollack, J. B., Greeley, R., & White, B. R. (1976). Saltation threshold on Mars: The effect of interparticle force, surface-roughness, and low atmospheric density. *Icarus*, *29*, 381–393. https://doi.org/10.1016/0019-1035(76)90140-8
Iversen, J. D., & Rasmussen, K. R. (1994). The effect of surface slope on saltation threshold. *Sedimentology*, *41*, 721–728. https://doi.org/10.1111/j.1365-3091.1994.tb01419.x
Iversen, J. D., & White, B. R. (1982). Saltation threshold on Earth, Mars and Venus. *Sedimentology*, *29*, 111. https://doi.org/10.1111/j.1365-3091.1982.tb01713.x
Jenkins, J. T., Cantat, I., & Valance, A. (2010). Continuum model for steady, fully developed saltation above a horizontal particle bed. *Physical Review E*, *82*, 020,301(R). https://doi.org/10.1103/PhysRevE.82.020301

Jenkins, J. T., & Valance, A. (2014). Periodic trajectories in aeolian sand transport. *Physics of Fluids*, *26*(7), 073,301. https://doi.org/10.1063/1.4885576

Jenkins, J. T., & Valance, A. (2018). Two-phase continuum theory for windblown sand. *Physical Review Fluids*, *3*, 34305. https://doi.org/10.1103/PhysRevFluids.3.034305

Jia, P., Andreotti, B., & Claudin, P. (2017). Giant ripples on comet 67p/churyumov-gerasimenko sculpted by sunset thermal wind. *Proceedings of the National Academy of Science*, *114*(10), 2509–2514. https://doi.org/10.1073/pnas.1612176114

Jia, X., Brunet, T., & Laurent, J. (2011). Elastic weakening of a dense granular pack by acoustic fluidization: Slipping, compaction, and aging. *Physical Review E*, *84*, 020,301. https://doi.org/10.1103/PhysRevE.84.020301

Jop, P. (2015). Rheological properties of dense granular flows. *Comptes Rendus Physique*, *16*(1), 62–72. https://doi.org/10.1016/j.crhy.2014.12.001

Jop, P., Forterre, Y., & Pouliquen, O. (2005). Crucial role of sidewalls in granular surface flows: Consequences for the rheology. *Journal of Fluid Mechanics*, *541*, 167–192. https://doi.org/10.1017/S0022112005005987

Jop, P., Forterre, Y., & Pouliquen, O. (2006). A constitutive law for dense granular flows. *Nature*, *441*(7094), 727–730. https://doi.org/10.1038/nature04801

Kalinske, A. A. (1947). Movement of sediment as bed load in rivers. *Transactions of the American Geophysical Union*, *28*(4), 615–620. https://doi.org/10.1029/TR028i004p00615

Kamrin, K. (2018). Quantitative rheological model for granular materials: The importance of particle size. In *Handbook of Materials Modeling: Applications: Current and Emerging Materials* (pp. 1–24). New York City: Springer, Cham.

Kamrin, K., & Henann, D. L. (2015). Nonlocal modeling of granular flows down inclines. *Soft Matter*, *11*(1), 179–185. https://doi.org/10.1039/C4SM01838A

Kamrin, K., & Koval, G. (2012). Nonlocal constitutive relation for steady granular flow. *Physical Review Letters*, *108*, 178301. https://doi.org/10.1103/PhysRevLett.108.178301

Kamrin, K., & Koval, G. (2014). Effect of particle surface friction on nonlocal constitutive behavior of flowing granular media. *Computational Particle Mechanics*, *1*, 169–176. https://doi.org/10.1007/s40571-014-0018-3

Kaufmann, E., Kömle, N. I., & Kargl, G. (2006). Laboratory simulation experiments on the solid-state greenhouse effect in planetary ices. *Icarus*, *185*(1), 274–286. https://doi.org/10.1016/j.icarus.2006.07.009

Kirchner, J. W., Dietrich, W. E., Iseya, F., & Ikeda, H. (1990). The variability of critical shear stress, friction angle, and grain protrusion in water-worked sediments. *Sedimentology*, *37*(4), 647–672. https://doi.org/10.1111/j.1365-3091.1990.tb00627.x

Knight, J. B., Fandrich, C. G., Lau, C. N., Jaeger, H. M., & Nagel, S. R. (1995). Density relaxation in a vibrated granular material. *Physical Review E*, *51*, 3957–3963. https://doi.org/10.1103/PhysRevE.51.3957

Kok, J. F. (2010a). An improved parametrization of wind blown sand flux on Mars that includes the effect of hysteresis. *Geophysical Research Letters*, *37*, L12202. https://doi.org/10.1029/2010GL043646

Kok, J. F. (2010b). Difference in the wind speeds required for initiation versus continuation of sand transport on Mars: Implications for dunes and dust storms. *Physical Review Letters*, *104*, 74502. https://doi.org/10.1103/PhysRevLett.104.074502

Kok, J. F., Parteli, E. J. R., Michaels, T. I., & Karam, D. B. (2012). The physics of wind-blown sand and dust. *Reports on Progress in Physics*, *75*, 106901. https://doi.org/10.1088/0034-4885/75/10/106901

Kok, J. F., & Renno, N. O. (2006). Enhancement of the emission of mineral dust aerosols by electric forces. *Physical Review Letters*, *33*, L19S10. https://doi.org/10.1029/2006GL026284

Kok, J. F., & Renno, N. O. (2009). A comprehensive numerical model of steady state saltation (comsalt). *Journal of Geophysical Research*, *114*, D17204. https://doi.org/10.1029/2009JD011702

Komatsu, T. S., Inagaki, S., Nakagawa, N., & Nasuno, S. (2001). Creep motion in a granular pile exhibiting steady surface flow. *Physical Review Letters*, *86*, 1757–1760. https://doi.org/10.1103/PhysRevLett.86.1757

Koval, G., Roux, J. N., Corfdir, A., & Chevoir, F. (2009). Annular shear of cohesionless granular materials: From the inertial to quasistatic regime. *Physical Review E*, *79*, 21306. https://doi.org/10.1103/PhysRevE.79.021306

Kramer, H. (1935). Sand mixtures and sand movement in fluvial models. *Transactions of the American Society of Civil Engineers*, *100*, 798–838.

Lacks, D. J., & Sankaran, R. M. (2011). Contact electrification of insulating materials. *Journal of Physics D: Applied Physics*, *44*(45), 453001. https://doi.org/10.1088/0022-3727/44/45/453001

Lajeunesse, E., Malverti, L., & Charru, F. (2010). Bed load transport in turbulent flow at the grain scale: Experiments and modeling. *Journal of Geophysical Research*, *115*, F04001. https://doi.org/10.1029/2009JF001628

Lämmel, M., Dzikowski, K., Kroy, K., Oger, L., & Valance, A. (2017). Grain-scale modeling and splash parametrization for aeolian sand transport. *Physical Review E*, *95*, 22902. https://doi.org/10.1103/PhysRevE.95.022902

Lämmel, M., & Kroy, K. (2017). Analytical mesoscale modeling of aeolian sand transport. *Physical Review E*, *96*, 52906. https://doi.org/10.1103/PhysRevE.96.052906

Lämmel, M., Rings, D., & Kroy, K. (2012). A two-species continuum model for aeolian sand transport. *New Journal of Physics*, *14*, 93037. https://doi.org/10.1088/1367-2630/14/9/093037

Lätzel, M., Luding, S., Herrmann, H. J., Howell, D. W., & Behringer, R. P. (2003). Comparing simulation and experiment of a 2D granular couette shear device. *The European Physical Journal E*, *11*, 325–333. https://doi.org/10.1140/epje/i2002-10160-7

Lavelle, J. W., & Mofjeld, H. O. (1987). Do critical stresses for incipient motion and erosion really exist? *Journal of Hydraulic Engineering*, *113*(3), 370–385. https://doi.org/10.1061/(ASCE)0733-9429(1987)113:3(370)

Lebonnois, S., Schubert, G., Forgeta, F., & Spiga, A. (2018). Planetary boundary layer and slope winds on Venus. *Icarus*, *314* 149–158. https://doi.org/10.1016/j.icarus.2018.06.006

Lee, D. B., & Jerolmack, D. (2018). Determining the scales of collective entrainment in collision-driven bed load. *Earth Surface Dynamics*, *6*, 1089–1099. https://doi.org/10.5194/esurf-6-1089-2018

Lee, H., Ha, M. Y., & Balachandar, S. (2012). Work-based criterion for particle motion and implication for turbulent bed-load transport. *Physics of Fluids*, *24*, 116604. https://doi.org/10.1063/1.4767541

Lehning, M., Doorschot, J., & Bartelt, P. (2000). A snowdrift index based on snowpack model calculations. *Annals of Glaciology*, *31*, 382–386. https://doi.org/10.3189/172756400781819770

Li, B., & McKenna Neuman, C. (2012). Boundary-layer turbulence characteristics during aeolian saltation. *Geophysical Research Letters*, *39*(11), L11402. https://doi.org/10.1029/2012GL052234

Li, S., & Henann, D. L. (2019). Material stability and instability in non-local continuum models for dense granular materials. *Journal of Fluid Mechanics*, *871*, 799–830. https://doi.org/10.1017/jfm.2019.311

Ling, C. H. (1995). Criteria for incipient motion of spherical sediment particles. *Journal of Hydraulic Engineering*, *121*(6), 472–478. https://doi.org/10.1061/(ASCE)0733-9429(1995)121:6(472)
Liu, Y., & Szlufarska, I. (2012). Chemical origins of frictional aging. *Physical Review Letters*, *109*, 186102. https://doi.org/10.1103/PhysRevLett.109.186102
Lobkovsky, A. E., Orpe, A., Molloy, R., Kudrolli, A., & Rothman, D. (2008). Erosion of a granular bed driven by laminar fluid flow. *Journal of Fluid Mechanics*, *605*, 47–58. https://doi.org/10.1017/S0022112008001389
Loiseleux, T., Gondret, P., Rabaud, M., & Doppler, D. (2005). Onset of erosion and avalanche for an inclined granular bed sheared by a continuous laminar flow. *Physics of Fluids*, *17*, 103304. https://doi.org/10.1063/1.2109747
Lorenz, R. D. (2014). Physics of saltation and sand transport on Titan: A brief review. *Icarus*, *230*, 162–167. https://doi.org/10.1016/j.icarus.2013.06.023
Lorenz, R. D., Claudin, P., Andreotti, B., Radebaugh, J., & Tokanod, T. (2010). A 3 km atmospheric boundary layer on Titan indicated by dune spacing and Huygens data. *Icarus*, *205*(2), 719–721. https://doi.org/10.1016/j.icarus.2009.08.002
Lu, H., Raupach, M. R., & Richards, K. S. (2005). Modeling entrainment of sedimentary particles by wind and water: A generalized approach. *Journal of Geophysical Research*, *110*, D24114. https://doi.org/10.1029/2005JD006418
Lyles, L., & Krauss, R. K. (1971). Threshold velocities and initial particle motion as influenced by air turbulence. In *Transactions of the American Society of Agricultural Engineers* (Vol. 14, pp. 563–566). Saint Joseph, Michigan: ASAE. https://doi.org/10.13031/2013.38339
MacKenzie, L. G., & Eaton, B. C. (2017). Large grains matter: Contrasting bed stability and morphodynamics during two nearly identical experiments. *Earth Surface Processes and Landforms*, *42*, 1287–1295. https://doi.org/10.1002/esp.4122
MacKenzie, L. G., Eaton, B. C., & Church, M. (2018). Breaking from the average: Why large grains matter in gravel-bed streams. *Earth Surface Processes and Landforms*, *43*, 3190–3196. https://doi.org/10.1002/esp.4465
Mantz, P. A. (1977). Incipient transport of fine grains and flakes by fluids-extended shield diagram. *Journal of the Hydraulics Division*, *103*. ASCE 12992).
Martin, R. L., Jerolmack, D. J., & Schumer, R. (2012). The physical basis for anomalous diffusion in bed load transport. *Journal of Geophysical Research: Earth Surface*, *117*, F01018. https://doi.org/10.1029/2011JF002075
Martin, R. L., & Kok, J. F. (2017). Wind-invariant saltation heights imply linear scaling of aeolian saltation flux with shear stress. *Science Advances*, *3*, e1602569. https://doi.org/10.1126/sciadv.1602569
Martin, R. L., & Kok, J. F. (2018). Distinct thresholds for the initiation and cessation of aeolian saltation from field measurements. *Journal of Geophysical Research: Earth Surface*, *123*, 1546–1565. https://doi.org/10.1029/2017JF004416
Martin, R. L., & Kok, J. F. (2019). Size-independent susceptibility to transport in aeolian saltation. *Journal of Geophysical Research: Earth Surface*, *124*, 1658–1674. https://doi.org/10.1029/2019JF005104
Masteller, C. C., & Finnegan, N. J. (2017). Interplay between grain protrusion and sediment entrainment in an experimental flume. *Journal of Geophysical Research: Earth Surface*, *122*, 274–289. https://doi.org/10.1002/2016JF003943
Maurin, R., Chauchat, J., Chareyre, B., & Frey, P. (2015). A minimal coupled fluid-discrete element model for bedload transport. *Physics of Fluids*, *27*(11), 113302. https://doi.org/10.1063/1.4935703
Maurin, R., Chauchat, J., & Frey, P. (2016). Dense granular flow rheology in turbulent bedload transport. *Journal of Fluid Mechanics*, *804*, 490–512. https://doi.org/10.1017/jfm.2016.520
Maurin, R., Chauchat, J., & Frey, P. (2018). Revisiting slope influence in turbulent bedload transport: Consequences for vertical flow structure and transport rate scaling. *Journal of Fluid Mechanics*, *839*, 135–156. https://doi.org/10.1017/jfm.2017.903
McElwaine, J. N., Maeno, N., & Sugiura, K. (2004). The splash function for snow from wind-tunnel measurements. *Annals of Glaciology*, *38*, 71–78. https://doi.org/10.3189/172756404781815356
McEwan, I. K., Willetts, B. B., & Rice, M. A. (1992). The grain/bed collision in sand transport by wind. *Sedimentology*, *39*(6), 971–981. https://doi.org/10.1111/j.1365-3091.1992.tb01991.x
Merrison, J. P. (2012). Sand transport, erosion and granular electrification. *Aeolian Research*, *4*, 1–16. https://doi.org/10.1016/j.aeolia.2011.12.003
Merrison, J. P., Gunnlaugsson, H. P., Nørnberg, P., Jensen, A. E., & Rasmussen, K. (2007). Determination of the wind induced detachment threshold for granular material on Mars using wind tunnel simulations. *Icarus*, *191*, 568–580. https://doi.org/10.1016/j.icarus.2007.04.035
Meyer-Peter, E., & Müller, R. (1948). Formulas for bedload transport. In *Proceedings of the 2nd Meeting of the International Association for Hydraulic Structures Research* (pp. 39–64). Stockholm: IAHR.
MiDi, G. (2004). On dense granular flows. *The European Physical Journal E*, *14*(4), 341–365. https://doi.org/10.1140/epje/i2003-10153-0
Miller, M. C., McCave, I. N., & Komar, P. D. (1977). Threshold of sediment motion under unidirectional currents. *Sedimentology*, *24*, 507–527. https://doi.org/10.1111/j.1365-3091.1977.tb00136.x
Mitha, S., Tran, M. Q., Werner, B. T., & Haff, P. K. (1986). The grain-bed impact process in aeolian saltation. *Acta Mechanica*, *63*, 267–278. https://doi.org/10.1007/BF01182553
Mollinger, A. M., & Nieuwstadt, F. T. M. (1996). Measurement of the lift force on a particle fixed to the wall in the viscous sublayer of a fully developed turbulent boundary layer. *Journal of Fluid Mechanics*, *316*, 285–306. https://doi.org/10.1017/S0022112096000547
Moore, P. L., & Iverson, N. R. (2002). Slow episodic shear of granular materials regulated by dilatant strengthening. *Geology*, *30*(9), 843–846. https://doi.org/10.1130/0091-7613(2002)030<0843:SESOGM>2.0.CO;2
Moosavi, R., Reza Shaebani, M., Maleki, M., Török, J., Wolf, D. E., & Losert, W. (2013). Coexistence and transition between shear zones in slow granular flows. *Physical Review Letters*, *111*, 148301. https://doi.org/10.1103/PhysRevLett.111.148301
Nalpanis, P., Hunt, J. C. R., & Barrett, C. F. (1993). Saltating particles over flat beds. *Journal of Fluid Mechanics*, *251*, 661–685. https://doi.org/10.1017/S0022112093003568
Namikas, S. L. (2006). A conceptual model of energy partitioning in the collision of saltating grains with an unconsolidated sediment bed. *Journal of Coastal Research*, *22*(5), 1250–1259. https://doi.org/10.2112/06A-0007.1
Nelson, J. M., Shreve, R. L., McLean, S. R., & Drake, T. G. (1995). Role of near-bed turbulence structure in bed load transport and bed form mechanics. *Water Resources Research*, *31*(8), 2071–2086. https://doi.org/10.1029/95WR00976
Ness, C., & Sun, J. (2015). Flow regime transitions in dense non-Brownian suspensions: Rheology, microstructural characterization, and constitutive modeling. *Physical Review E*, *91*, 012,201. https://doi.org/10.1103/PhysRevE.91.012201
Ness, C., & Sun, J. (2016). Shear thickening regimes of dense non-Brownian suspensions. *Soft Matter*, *12*, 914–924. https://doi.org/10.1039/c5sm02326b
Nichol, K., Zanin, A., Bastien, R., Wandersman, E., & van Hecke, M. (2010). Flow-induced agitations create a granular fluid. *Physical Review Letters*, *104*, 078,302. https://doi.org/10.1103/PhysRevLett.104.078302

Nickling, W. G. (1988). The initiation of particle movement by wind. *Sedimentology*, *35*(3), 499–511. https://doi.org/10.1111/j.1365-3091.1988.tb01000.x

Nino, Y., & Garcia, M. (1998). Using Lagrangian particle saltation observations for bedload sediment transport modelling. *Hydrological Processes*, *12*, 1197–1218. https://doi.org/10.1002/(SICI)1099-1085(19980630)12:8<1197::AID-HYP612>3.0.CO;2-U

Nishida, M., Tanaka, K., & Matsumoto, Y. (2004). Discrete element method simulation of the restitutive characteristics of a steel spherical projectile from a particulate aggregation. *JSME International Journal Series A Solid Mechanics and Material Engineering*, *47*(3), 438–447. https://doi.org/10.1299/jsmea.47.438

Oger, L., Ammi, M., Valance, A., & Beladjine, D. (2005). Discrete element method studies of the collision of one rapid sphere on 2D and 3D packings. *The European Physical Journal E*, *17*, 467–476. https://doi.org/10.1140/epje/i2005-10022-x

Oger, L., Ammi, M., Valance, A., & Beladjine, D. (2008). Study of the collision of one rapid sphere on 3D packings: Experimental and numerical results. *Computers and Mathematics with Applications*, *55*, 132–148. https://doi.org/10.1016/j.camwa.2007.04.001

Ouriemi, M., Aussillous, P., Medale, M., Peysson, Y., & Guazzelli, E. (2007). Determination of the critical shields number for particle erosion in laminar flow. *Physics of Fluids*, *19*(6), 61706. https://doi.org/10.1063/1.2747677

Pähtz, T. (2018). Comment on "Distinct thresholds for the initiation and cessation of aeolian saltation from field measurements" by Raleigh L. Martin and Jasper F. Kok: Alternative interpretation of measured thresholds as two distinct cessation thresholds. *Journal of Geophysical Research: Earth Surface*, *123*, 3388–3391. https://doi.org/10.1029/2018JF004824

Pähtz, T., & Durán, O. (2017). Fluid forces or impacts: What governs the entrainment of soil particles in sediment transport mediated by a Newtonian fluid? *Physical Review Fluids*, *2*(7), 74303. https://doi.org/10.1103/PhysRevFluids.2.074303

Pähtz, T., & Durán, O. (2018a). The cessation threshold of nonsuspended sediment transport across aeolian and fluvial environments. *Journal of Geophysical Research: Earth Surface*, *123*, 1638–1666. https://doi.org/10.1029/2017JF004580

Pähtz, T., & Durán, O. (2018b). Universal friction law at granular solid-gas transition explains scaling of sediment transport load with excess fluid shear stress. *Physical Review Fluids*, *3*(10), 104302. https://doi.org/10.1103/PhysRevFluids.3.104302

Pähtz, T., Durán, O., de Klerk, D. N., Govender, I., & Trulsson, M. (2019). Local rheology relation with variable yield stress ratio across dry, wet, dense, and dilute granular flows. *Physical Review Letters*, *123*(4), 48001. https://doi.org/10.1103/PhysRevLett.123.048001

Pähtz, T., Kok, J. F., & Herrmann, H. J. (2012). The apparent roughness of a sand surface blown by wind from an analytical model of saltation. *New Journal of Physics*, *14*(4), 43035. https://doi.org/10.1088/1367-2630/14/4/043035

Pähtz, T., Liu, Y., Hu, P., & He, Z. (2020). Bridging aeolian and fluvial sediment transport thresholds: A generalised shields curve from a periodic saltation model, https://arxiv.org/abs/1912.07208.

Pähtz, T., Valyrakis, M., Zhao, X. H., & Li, Z. S. (2018). The critical role of the boundary layer thickness for the initiation of aeolian sediment transport. *Geosciences*, *8*(9), 314. https://doi.org/10.3390/geosciences8090314

Paintal, A. S. (1971). Concept of critical shear stress in loose boundary open channels. *Journal of Hydraulic Research*, *9*, 91–113. https://doi.org/10.1080/00221687109500339

Papanicolaou, A., Diplas, P., Dancey, C. L., & Balakrishnan, M. (2001). Surface roughness effects in near-bed turbulence: Implications to sediment entrainment. *Journal of Engineering Mechanics*, *127*(3), 211–218. https://doi.org/10.1061/(ASCE)0733-9399(2001)127:3(211)

Paphitis, D. (2001). Sediment movement under unidirectional flows: An assessment of empirical threshold curves. *Coastal Engineering*, *43*(3-4), 227–245. https://doi.org/10.1016/S0378-3839(01)00015-1

Parker, G. (1978). Self-formed straight rivers with equilibrium banks and mobile bed. Part 2. The gravel river. *Journal of Fluid Mechanics*, *89*, 127–146. https://doi.org/10.1017/S0022112078002505

Parker, G., & Klingeman, P. C. (1982). On why gravel bed streams are paved. *Water Resources Research*, *18*(5), 1409–1423. https://doi.org/10.1029/WR018i005p01409

Petrosyan, A., Galperin, B., Larsen, S. E., Lewis, S. R., Määttänen, A., Read, P. L., et al. (2011). The Martian atmospheric boundary layer. *Reviews of Geophysics*, *49*, RG3005. https://doi.org/10.1029/2010RG000351

Peyneau, P. E., & Roux, J. N. (2008a). Frictionless bead packs have macroscopic friction, but no dilatancy. *Physical Review E*, *78*, 11307. https://doi.org/10.1103/PhysRevE.78.011307

Peyneau, P. E., & Roux, J. N. (2008b). Solidlike behavior and anisotropy in rigid frictionless bead assemblies. *Physical Review E*, *78*, 41307. https://doi.org/10.1103/PhysRevE.78.041307

Phillips, C. B., & Jerolmack, D. J. (2016). Self-organization of river channels as a critical filter on climate signals. *Science*, *352*(6286), 694–697. https://doi.org/10.1126/science.aad3348

Pierson, T. C., Costa, J. E., & Vancouver, W. (1987). A rheologic classification of subaerial sediment-water flows, Debris flows/avalanches: Process, recognition, and mitigation. *Reviews in Engineering Geology*, *7*, 1–12. https://doi.org/10.1130/REG7-p1

Pilotti, M., & Menduni, G. (2001). Beginning of sediment transport of incoherent grains in shallow shear flows. *Journal of Hydraulic Research*, *39*(2), 115–124. https://doi.org/10.1080/00221680109499812

Pons, A., Darnige, T., Crassous, J., Clément, E., & Amon, A. (2016). Spatial repartition of local plastic processes in different creep regimes in a granular material. *Europhysics Letters*, *113*(2), 843–846. https://doi.org/10.1209/0295-5075/113/28001

Pouliquen, O., & Forterre, Y. (2009). A non-local rheology for dense granular flows, Philosophical Transactions of the Royal Society A: Mathematical. *Physical and Engineering Sciences*, *367*(1909), 5091–5107. https://doi.org/10.1098/rsta.2009.0171

Prancevic, J. P., & Lamb, M. P. (2015). Unraveling bed slope from relative roughness in initial sediment motion. *Journal of Geophysical Research: Earth Surface*, *120*, 474–489. https://doi.org/10.1002/2014JF003323

Prancevic, J. P., Lamb, M. P., & Fuller, B. M. (2014). Incipient sediment motion across the river to debris-fl ow transition. *Geology*, *42*(3), 191–194. https://doi.org/10.1130/G34927.1

Radjaï, F., Wolf, D. E., Jean, M., & Moreau, J. J. (1998). Bimodal character of stress transmission in granular packings. *Physical Review Letters*, *80*, 61–64. https://doi.org/10.1103/PhysRevLett.80.61

Raffaele, L., Bruno, L., Pellerey, F., & Preziosi, L. (2016). Windblown sand saltation: A statistical approach to fluid threshold shear velocity. *Aeolian Research*, *23*, 79–91. https://doi.org/10.1016/j.aeolia.2016.10.002

Rasmussen, K. R., Valance, A., & Merrison, J. (2015). Laboratory studies of aeolian sediment transport processes on planetary surfaces. *Geomorphology*, *244*, 74–94. https://doi.org/10.1016/j.geomorph.2015.03.041

Recking, A. (2010). A comparison between flume and field bed load transport data and consequences for surface-based bed load transport prediction. *Water Resources Research*, *46*, W03,518. https://doi.org/10.1029/2009WR008007

Recking, A., Liébault, F., Peteuil, C., & Jolimet, T. (2012). Testing bedload transport equations with consideration of time scales. *Earth Surface Processes and Landforms*, *37*, 774–789. https://doi.org/10.1002/esp.3213

Reid, I., Frostick, L. E., & Layman, J. T. (1985). The incidence and nature of bedload transport during flood flows in coarse-grained alluvial channels. *Earth Surface Processes and Landforms*, *10*(1), 33–44. https://doi.org/10.1002/esp.3290100107

Ribière, P., Philippe, P., Richard, P., Delannay, R., & Bideau, D. (2005). Slow compaction of granular systems. *Journal of Physics: Condensed Matter*, *17*(24), S2743–S2754. https://doi.org/10.1088/0953-8984/17/24/024

Rice, M. A., Willetts, B. B., & McEwan, I. K. (1995). An experimental study of multiple grain-size ejecta produced by collisions of saltating grains with a flat bed. *Sedimentology*, *42*(4), 695–706. https://doi.org/10.1111/j.1365-3091.1995.tb00401.x

Rice, M. A., Willetts, B. B., & McEwan, I. K. (1996). Observations of collisions of saltating grains with a granular bed from high-speed cine-film. *Sedimentology*, *43*(1), 21–31. https://doi.org/10.1111/j.1365-3091.1996.tb01456.x

van Rijn, L. C. (1984). Sediment transport, part I: Bed load transport. *Journal of Hydraulic Engineering*, *110*, 1431–1456. https://doi.org/10.1061/(ASCE)0733-9429(1984)110:10(1431)

Rioual, F., Valance, A., & Bideau, D. (2000). Experimental study of the collision process of a grain on a two-dimensional granular bed. *Physical Review E*, *62*, 2450. https://doi.org/10.1103/PhysRevE.62.2450

Rioual, F., Valance, A., & Bideau, D. (2003). Collision process of a bead on a two-dimensional bead packing: Importance of the inter-granular contacts. *Europhysics Letters*, *61*(2), 194. https://doi.org/10.1209/epl/i2003-00212-8

Roering, J. J., Kirchner, J. W., Sklar, L. S., & Dietrich, W. E. (2001). Hillslope evolution by nonlinear creep and landsliding: An experimental study. *Geology*, *29*(2), 143–146. https://doi.org/10.1130/0091-7613(2002)030<0481:HEBNCA>2.0.CO;2

Salevan, J. C., Clark, A. H., Shattuck, M. D., O'Hern, C. S., & Ouellette, N. T. (2017). Determining the onset of hydrodynamic erosion in turbulent flow. *Physical Review Fluids*, *2*, 114302. https://doi.org/10.1103/PhysRevFluids.2.114302

Salim, S., Pattiaratchi, C., Tinoco, R., Coco, G., Hetzel, Y., Wijeratne, S., & Jayaratne, R. (2017). The influence of turbulent bursting on sediment resuspension under unidirectional currents. *Earth Surface Dynamics*, *5*, 399–415. https://doi.org/10.5194/esurf-5-399-2017

Salim, S., Pattiaratchi, C., Tinoco, R. O., & Jayaratne, R. (2018). Sediment resuspension due to near-bed turbulent effects: A deep sea case study on the northwest continental slope of western australia. *Journal of Geophysical Research: Oceans*, *123*, 7102–7119. https://doi.org/10.1029/2018JC013819

Savage, S. B. (1984). *The mechanics of rapid granular flows*. In Advances in Applied Mechanics (Vol. 24, pp. 289–366). San Diego, USA: Elsevier. https://doi.org/10.1016/S0065-2156(08)70047-4

Schmeeckle, M. W. (2014). Numerical simulation of turbulence and sediment transport of medium sand. *Journal of Geophysical Research: Earth Surface*, *119*, 1240–1262. https://doi.org/10.1002/2013JF002911

Schmeeckle, M. W., Nelson, J. M., & Shreve, R. L. (2007). Forces on stationary particles in near-bed turbulent flows. *Journal of Geophysical Research*, *112*, F02003. https://doi.org/10.1029/2006JF000536

Schmidt, R. A. (1980). Threshold wind-speeds and elastic impact in snow transport. *Journal of Glaciology*, *26*(94), 453–467. https://doi.org/10.3189/S0022143000010972

Seizilles, G., Lajeunesse, E., Devauchelle, O., & Bak, M. (2014). Cross-stream diffusion in bedload transport. *Physics of Fluids*, *26*, 13302. https://doi.org/10.1063/1.4861001

Shao, Y., & Lu, H. (2000). A simple expression for wind erosion threshold friction velocity. *Journal of Geophysical Research*, *105*(D17), 22,437–22,443. https://doi.org/10.1029/2000JD900304

Shields, A. F. (1936). *Application of similarity principles and turbulence research to bedload movement (English translation of the original German manuscript), 167*. California Institute of Technology, Pasadena: Hydrodynamics Laboratory. https://resolver.caltech.edu/CaltechKHR:HydroLabpub167

Shih, W., & Diplas, P. (2018). A unified approach to bed load transport description over a wide range of flow conditions via the use of conditional data treatment. *Water Resources Research*, *54*, 3490–3509. https://doi.org/10.1029/2017WR022373

Shih, W., & Diplas, P. (2019). Threshold of motion conditions under stokes flow regime and comparison with turbulent flow data. *Water Resources Research*, *55*, 10,872–10,892. https://doi.org/10.1029/2019WR024836

Silvestro, S., Vaz, D. A., Ewing, R. C., Rossi, A. P., Fenton, L. K., Michaels, T. I., et al. (2013). Pervasive aeolian activity along rover Curiosity's traverse in Gale Crater, Mars. *Geology*, *41*(4), 483–486. https://doi.org/10.1130/G34162.1

Singh, A., Fienberg, K., Jerolmack, D. J., Marr, J., & Foufoula-Georgiou, E. (2009). Experimental evidence for statistical scaling and intermittency in sediment transport rates. *Journal of Geophysical Research*, *114*, F01025. https://doi.org/10.1029/2007JF000963

Smits, A. J., McKeon, B. J., & Marusic, I. (2011). High-Reynolds number wall turbulence. *Annual Review of Fluid Mechanics*, *43*, 353–375. https://doi.org/10.1146/annurev-fluid-122109-160753

Srivastava, I., Silbert, L. E., Grest, G. S., & Lechman, J. B. (2019). Flow-arrest transitions in frictional granular matter. *Physical Review Letters*, *122*, 48003. https://doi.org/10.1103/PhysRevLett.122.048003

Stewart, R. L., Bridgwater, J., Zhou, Y. C., & Yu, A. B. (2001). Simulated and measured flow of granules in a bladed mixer–a detailed comparison. *Chemical Engineering Science*, *56*(19), 5457–5471. https://doi.org/10.1016/S0009-2509(01)00190-7

Sullivan, R., & Kok, J. F. (2017). Aeolian saltation on Mars at low wind speeds. *Journal of Geophysical Research: Planets*, *122*, 2111–2143. https://doi.org/10.1002/2017JE005275

Sumer, B. M., Chua, L. H. C., Cheng, N. S., & Fredsøe, J. (2003). Influence of turbulence on bed load sediment transport. *Journal of Hydraulic Engineering*, *129*(8), 585–596. https://doi.org/10.1061/(ASCE)0733-9429(2003)129:8(585)

Sutherland, A. J. (1967). Proposed mechanism for sediment entrainment by turbulent flows. *Journal of Geophysical Research*, *72*(24), 6183–6194. https://doi.org/10.1029/JZ072i024p06183

Swann, C., Sherman, D. J., & Ewing, R. C. (2020). Experimentally-derived thresholds for windblown sand on mars. *Geophysical Research Letters*, *47*, e2019GL084484. https://doi.org/10.1029/2019GL084484

Takahashi, T. (1978). Mechanical characteristics of debris flow. *Journal of Hydraulics Division, ASCE*, *104*, 1153–1169.

Tanabe, T., Shimada, T., Ito, N., & Nishimori, H. (2017). Splash detail due to a single grain incident on a granular bed. *Physical Review E*, *95*, 022,906. https://doi.org/10.1103/PhysRevE.95.022906

Tanaka, K., Nishida, M., Kunimochi, T., & Takagi, T. (2002). Discrete element simulation and experiment for dynamic response of two-dimensional granular matter to the impact of a spherical projectile. *Powder Technology*, *124*, 160–173. https://doi.org/10.1016/S0032-5910(01)00489-2

Telfer, M. W., Parteli, E. J. R., Radebaugh, J., Beyer, R. A., Bertrand, T., Forget, F., et al. The New Horizons Geology, Geophysics and Imaging Science Theme Team (2018). Dunes on Pluto. *Science*, *360*, 992–997. https://doi.org/10.1126/science.aao2975

Terzaghi, K. (1951). *Theoretical soil mechanics*. London: Chapman And Hall, Limited.

Thomas, N., Davidsson, B., El-Maarry, M. R., Fornasier, S., Giacomini, L., Gracia-Berná, A. G., et al. (2015). Redistribution of particles across the nucleus of comet 67p/churyumov-gerasimenko. *Astronomy & Astrophysics*, *583*, A17. https://doi.org/10.1051/0004-6361/201526049

Thompson, J. D., & Clark, A. H. (2019). Critical scaling for yield is independent of distance to isostaticity. *Physical Review Research*, *1*, 012002(R). https://doi.org/10.1103/PhysRevResearch.1.012002

Topic, N., Retzepoglu, S., Wensing, M., Illigmann, C., Luzi, G., Agudo, J. R., & Wierschem, A. (2019). Effect of particle size ratio on shear-induced onset of particle motion at low particle Reynolds numbers: From high shielding to roughness. *Physics of Fluids*, *31*, 63305. https://doi.org/10.1063/1.5108800

Trulsson, M. (2018). Rheology and shear jamming of frictional ellipses. *Journal of Fluid Mechanics*, *849*, 718–740. https://doi.org/10.1017/jfm.2018.420

Trulsson, M., Andreotti, B., & Claudin, P. (2012). Transition from the viscous to inertial regime in dense suspensions. *Physical Review Letters*, *109*, 118305. https://doi.org/10.1103/PhysRevLett.109.118305

Valance, A., & Crassous, J. (2009). Granular medium impacted by a projectile: Experiment and model. *The European Physical Journal E*, *30*, 43–54. https://doi.org/10.1140/epje/i2009-10504-9

Valance, A., Rasmussen, K. R., Ould El Moctar, A., & Dupont, P. (2015). The physics of aeolian sand transport. *Comptes Rendus Physique*, *16*, 105–117. https://doi.org/10.1016/j.crhy.2015.01.006

Valyrakis, M. (2013). *Entrainment of coarse solid particles by energetic turbulent flow events*. New York: Nova Science Publishers.

Valyrakis, M., Diplas, P., & Dancey, C. L. (2011). Entrainment of coarse grains in turbulent flows: An extreme value theory approach. *Water Resources Research*, *47*, W09512. https://doi.org/10.1029/2010WR010236

Valyrakis, M., Diplas, P., & Dancey, C. L. (2013). Entrainment of coarse particles in turbulent flows: An energy approach. *Journal of Geophysical Research: Earth Surface*, *118*, 42–53. https://doi.org/10.1029/2012JF002354

Valyrakis, M., Diplas, P., Dancey, C. L., Greer, K., & Celik, A. O. (2010). Role of instantaneous force magnitude and duration on particle entrainment. *Journal of Geophysical Research*, *115*, F02006. https://doi.org/10.1029/2008JF001247

Voivret, C., Radjaï, F., Delenne, J. Y., & El Youssoufi, M. S. (2009). Multiscale force networks in highly polydisperse granular media. *Physical Review Letters*, *102*, 178001. https://doi.org/10.1103/PhysRevLett.102.178001

Vollmer, S., & Kleinhans, M. G. (2007). Predicting incipient motion, including the effect of turbulent pressure fluctuations in the bed. *Water Resources Research*, *43*, W05410. https://doi.org/10.1029/2006WR004919

Vowinckel, B., Jain, R., Kempe, T., & Fröhlich, J. (2016). Entrainment of single particles in a turbulent open-channel flow: A numerical study. *Journal of Hydraulic Research*, *54*(2), 158–171. https://doi.org/10.1080/00221686.2016.1140683

Vowinckel, B., Kempe, T., & Fröhlich, J. (2014). Fluid-particle interaction in turbulent open channel flow with fully-resolved mobile beds. *Advances in Water Resources*, *72*, 32–44. https://doi.org/10.1016/j.advwatres.2014.04.019

Wainwright, J., Parsons, A. J., Cooper, J. R., Gao, P., Gillies, J. A., Mao, L., et al. (2015). The concept of transport capacity in geomorphology. *Reviews of Geophysics*, *53*, 1155–1202. https://doi.org/10.1002/2014RG000474

Wang, P., & Zheng, X. (2014). Saltation transport rate in unsteady wind variations. *The European Physical Journal E*, *37*, 40. https://doi.org/10.1140/epje/i2014-14040-3

Wang, P., & Zheng, X. (2015). Unsteady saltation on Mars. *Icarus*, *260*, 161–166. https://doi.org/10.1016/j.icarus.2015.07.012

Ward, B. D. (1969). Relative density effects on incipient bed movement. *Water Resources Research*, *5*(5), 1090–1096. https://doi.org/10.1029/WR005i005p01090

Werner, B. T. (1990). A steady-state model of wind-blown sand transport. *The Journal of Geology*, *98*(1), 1–17. https://www.jstor.org/stable/30068220

Werner, B. T., & Haff, P. K. (1988). The impact process in aeolian saltation: Two-dimensional simulations. *Sedimentology*, *35*(2), 189–196. https://doi.org/10.1111/j.1365-3091.1988.tb00944.x

White, B. R., & Schulz, J. C. (1977). Magnus effect in saltation. *Journal of Fluid Mechanics*, *81*(3), 497–512. https://doi.org/10.1017/S0022112077002183

Wiberg, P. L., & Smith, J. D. (1987). Calculations of the critical shear stress for motion of uniform and heterogeneous sediments. *Water Resources Research*, *23*(8), 1471–1480. https://doi.org/10.1029/WR023i008p01471

Wiggs, G. F. S., Atherton, R. J., & Baird, A. J. (2004). Thresholds of aeolian sand transport: Establishing suitable values. *Sedimentology*, *51*, 95–108. https://doi.org/10.1046/j.1365-3091.2003.00613.x

Wilcock, P. R. (1993). Critical shear stress of natural sediments. *Journal of Hydraulic Engineering*, *119*(4), 491–505. https://doi.org/10.1061/(ASCE)0733-9429(1993)119:4(491)

Willetts, B. B., & Rice, M. A. (1986). Collisions in aeolian saltation. *Acta Mechanica*, *63*, 255–265. https://doi.org/10.1007/BF01182552

Willetts, B. B., & Rice, M. A. (1989). Collisions of quartz grains with a sand bed: The influence of incident angle. *Earth Surface Processes and Landforms*, *14*(8), 719–730. https://doi.org/10.1002/esp.3290140806

Williams, J. J., Butterfield, G. R., & Clark, D. G. (1994). Aerodynamic entrainment threshold: Effects of boundary layer flow conditions. *Sedimentology*, *41*, 309–328. https://doi.org/10.1111/j.1365-3091.1994.tb01408.x

Wong, M., & Parker, G. (2006). Reanalysis and correction of bed-load relation of Meyer-Peter and Müller using their own database. *Journal of Hydraulic Engineering*, *132*(11), 1159–1168. https://doi.org/10.1061/(ASCE)0733-9429(2006)132:11(1159)

Xing, M., & He, C. (2013). 3D ejection behavior of different sized particles in the grain-bed collision process. *Geomorphology*, *187*, 94–100. https://doi.org/10.1016/j.geomorph.2013.01.002

Yager, E. M., & Schmeeckle, M. W. (2013). The influence of vegetation on turbulence and bed load transport. *Journal of Geophysical Research: Earth Surface*, *118*, 1585–1601. https://doi.org/10.1002/jgrf.20085

Yager, E. M., Schmeeckle, M. W., & Badoux, A. (2018). Resistance is not futile: Grain resistance controls on observed critical shields stress variations. *Journal of Geophysical Research: Earth Surface*, *123*, 3308–3322. https://doi.org/10.1029/2018JF004817

Yalin, M. (1977). *Mechanics of sediment transport*. Oxford: Pergamon Press.

Yalin, M. S., & Karahan, E. (1979). Inception of sediment transport. *Journal of the Hydraulics Division*, *105*, 1433–1443.

Yan, L., Barizien, A., & Wyart, M. (2016). Model for the erosion onset of a granular bed sheared by a viscous fluid. *Physical Review E*, *93*, 12903. https://doi.org/10.1103/PhysRevE.93.012903

Yang, F. L., & Hunt, M. L. (2006). Dynamics of particle-particle collisions in a viscous liquid. *Physics of Fluids*, *18*, 121506. https://doi.org/10.1063/1.2396925

Yang, J. Q., & Nepf, H. M. (2018). A turbulence-based bed-load transport model for bare and vegetated channels. *Geophysical Research Letters*, *45*, 10,428–10,436. https://doi.org/10.1029/2018GL079319

Yang, J. Q., & Nepf, H. M. (2019). Impact of vegetation on bed load transport rate and bedform characteristics. *Water Resources Research*, *55*, 6109–6124. https://doi.org/10.1029/2018WR024404

Yang, Y., Gao, S., Wang, Y. P., Jia, J., Xiong, J., & Zhou, L. (2019). Revisiting the problem of sediment motion threshold. *Continental Shelf Research*, *187*, 103960. https://doi.org/10.1016/j.csr.2019.103960

Zanke, U. C. E. (2003). On the influence of turbulence on the initiation of sediment motion. *International Journal of Sediment Research*, *18*(1), 17–31.

Zhang, Q., & Kamrin, K. (2017). Microscopic description of the granular fluidity field in nonlocal flow modeling. *Physical Review Letters*, *118*, 58001. https://doi.org/10.1103/PhysRevLett.118.058001

Zheng, X., Zhu, W., & Xie, L. (2008). A probability density function of liftoff velocities in mixed-size wind sand flux, Science in China Series G: Physics. *Mechanics & Astronomy*, *51*(8), 976–985. https://doi.org/10.1007/s11433-008-0105-7

Zheng, X. J., Xie, L., & Zhou, Y. H. (2005). Exploration of probability distribution of velocities of saltating sand particles based on the stochastic particle-bed collisions. *Physics Letters A*, *341*, 107–118. https://doi.org/10.1016/j.physleta.2005.04.084

Zhu, W., Huo, X., Zhang, J., Wang, P., Pähtz, T., Huang, N., & He, Z. (2019). Large effects of particle size heterogeneity on dynamic saltation threshold. *Journal of Geophysical Research: Earth Surface*, *124*(8), 2311–2321. https://doi.org/10.1029/2019JF005094